THE ROLE OF SULFUR ALLOYING IN DEFECTS AND TRANSITIONS IN COPPER INDIUM GALLIUM DISELENIDE DISULFIDE THIN FILMS

by

ADAM FRASER HALVERSON

A DISSERTATION

Presented to the Department of Physics
and the Graduate School of the University of Oregon
in partial fulfillment of the requirements
for the degree of
Doctor of Philosophy

December 2007

"The Role of Sulfur Alloying in Defects and Transitions in Copper Indium Gallium Diselenide Disulfide Thin Films," a dissertation prepared by Adam Fraser Halverson in partial fulfillment of the requirements for the Doctor of Philosophy degree in the Department of Physics. This dissertation has been approved and accepted by:

Dr. Roger Haydock, Chair of the Examining Committee

3 October 2007
Date

Committee in Charge:

Committee in Charge:	Dr. Roger Haydock, Chair Dr. J. David Cohen, Advisor Dr. Stephen Gregory Dr. Hailin Wang Dr. Jim Hutchison

Accepted by:

Dean of the Graduate School

An Abstract of the Dissertation of

Adam Fraser Halverson for the degree of Doctor of Philosophy

in the Department of Physics to be taken December 2007

Title: THE ROLE OF SULFUR ALLOYING IN DEFECTS AND TRANSITIONS IN COPPER INDIUM GALLIUM DISELENIDE DISULFIDE THIN FILMS

Approved: ____

Dr. J. David Cohen

The effects of sulfur alloying on the electronic properties of $CuIn(SeS)_2$ and $CuInGa(SeS)_2$ materials has been investigated using sophisticated junction capacitance techniques including drive-level capacitance profiling and transient photocapacitance and photocurrent spectroscopies. CISSe and CIGSSe materials are used as absorber layers in thin-film photovoltaic devices. By characterizing the electronic properties of these materials we hope to understand how these materials can be improved to make thin-film devices with better conversion efficiencies. Sulfur widens the bandgap of these materials by moving the valence band to lower energies and the conduction band to higher energies. This significantly affects the electronic structure of these devices by increasing the activation energies of dominant acceptor levels and lowering room temperature free hole carrier densities. Using optical spectroscopies we observe a large, broad defect that also changes its apparent energetic depth with sulfur alloying. The occupation of this defect was controlled both optically and thermally, and showed a striking temperature dependence. This temperature dependence was measured by recording the relative defect signal, the ratio of the TPC signal in the defect regime to the above bandgap regime, as a function of temperature. As the temperature of the measurement was decreased, steps in the relative defect signal were observed, indicating the turning off of the thermal pathway that emptied trapped charge from the defect. Remarkably, such steps were seen at the same temperature in CISSe and CIGSSe devices with similar sulfur content. In addition, no steps were seen in CIGS devices. This points to a defect state specific to the incorporation of sulfur in the absorber material. We hope that a better understanding of the electronic structure of these materials will assist in the creation of improved wide-bandgap thin-film photovoltaic devices.

CURRICULUM VITAE

NAME OF AUTHOR: Adam Fraser Halverson

PLACE OF BIRTH: Seattle, WA

DATE OF BIRTH: April 22, 1978

GRADUATE AND UNDERGRADUATE SCHOOLS ATTENDED:

University of Oregon
Reed College

DEGREES AWARDED:

Doctor of Philosophy in Physics, 2007, University of Oregon
Master of Science in Physics, 2003, University of Oregon
Bachelor of Arts in Science, 2000, Reed College

AREAS OF SPECIAL INTEREST:

Solid State Physics
Photovoltaics

PROFESSIONAL EXPERIENCE:

Research and Teaching Assistant, Department of Physics, University of Oregon, Eugene, OR, 2001-2005]

Laser and Optics Physicist, Electro-Scientific Industries, Inc., Portland, Oregon, 2000-2001]

GRANTS, AWARDS AND HONORS:

National Science Foundation IGERT Fellow, University of Oregon, 2005-2007

President University of Oregon Physics Graduate Students, 2004 – 2005

PUBLICATIONS:

A. F. Halverson, J. J. Gutierrez, J. D. Cohen, B. Yan, J. Yang, and S. Guha, "Electronic characterization and effects of light-induced degradation on hydrogenated nanocrystalline silicon," Appl. Phys. Lett. 88, 017920, 2006.

J. J. Gutierrez, A. F. Halverson, E. D. Tweeten, J. D. Cohen, B. Yan, J. Yang, S. Guha, "Electronic properties of RF glow discharge intrinsic microcrystalline silicon near the amorphous silicon phase boundary", Mat. Res. Soc. Symp. Proc. Vol. 808 (A8.9.1), 2004.

A. F. Halverson, P. T. Erslev, J. Lee, J. D. Cohen, W. N. Shafarman, "Characterization of the electronic properties of wide bandgap $CuIn(SeS)_2$ alloys", Mat. Res. Soc. Symp. Proc. Vol. 865 (F.16.3), 2005.

A. F. Halverson, J. J. Gutierrez, J. D. Cohen, B. Yan, J. Yang, S. Guha, "The effects of hydrogen profiling and of light-induced degradation on the electronic properties of hydrogenated nanocrystalline silicon", Mat. Res. Soc. Symp. Proc. Vol. 862 (A.13.7), 2005.

A. F. Halverson, S. Nishiwaki, W. N. Shafarman, J. D. Cohen, "Electronic properties of wide bandgap pentenary chalcopyrite alloys and their photovoltaic devices," Photovoltaic Energy Conversion, Conference Record of the 2006 IEEE 4th World Conference on Photovoltaic Energy Conversion, Vol. 1, 364-367, 2006.

A. F. Halverson, J. Mattheis, U. Rau, J. D. Cohen, "Reverse bias induced metastable effects in $Cu(In,Ga)Se_2$ photovoltaic devices," Photovoltaic Energy Conversion, Conference Record of the 2006 IEEE 4th World Conference on Photovoltaic Energy Conversion, Vol. 1, 519-522, 2006.

A. F. Halverson, S. Nishiwaki, W. N. Shafarman, J. David Cohen, "Energetics of minority and majority carrier transitions through defects in wide bandgap pentenary $Cu(In,Ga)(Se,S)_2$ thin film solar cells." Mat. Res. Soc. Symp. Proc. Vol. 1012 (Y.04.04), 2007.

P. Erslev, A. Halverson, W. N. Shafarman, J. David Cohen, “Study of the electronic properties of matched Na-containing and Na-free $CuInGaSe_2$ samples using junction capacitance methods.” Mat. Res. Soc. Symp. Proc. Vol. 1012 (Y.12.30), 2007.

ACKNOWLEDGMENTS

I would like to thank all of the people that helped make this dissertation and degree possible for me to attain.

First and foremost I would like to thank my wife Teresa and new daughter Zooey without whom I would not have had the motivation or support to finish this work. Teresa has been unfailingly supportive of me in my efforts. She has helped me through the difficult times one goes through when undertaking a project of this magnitude. She has brightened all of my days. I would also like to acknowledge the support of my family throughout the odyssey of my education. They have provided me with valuable support, perspective, and relief during this long process.

I would like to thank the professors in the physics department at the University of Oregon and at Reed College who helped mold me into the scientist that I am. In particular I would like to thank Dr. J. David Cohen for taking me into his lab and giving me the opportunity to prosper. His knowledge and direction have been indispensable to my research and degree. I would like to acknowledge the support of Dr. David Sokoloff for funding me in my early years of graduate school. Without his support I would not have made it this far. I would also like to acknowledge Dr. Bill Shafarman at the University of Delaware for the valuable and unique samples that he grew for us.

Finally I would like to acknowledge my lab mates and friends who made the graduate school experience interesting, fun, and tolerable. We have had many adventures on the road through graduate school. Let's hope for many more.

TABLE OF CONTENTS

LIST OF FIGURES

LIST OF TABLES

CHAPTER I

INTRODUCTION TO WIDE BANDGAP THIN-FILM PHOTOVOLTAICS

1.1 Solar Photovoltaics as a Viable Power Source

The sun is the primary source of external energy input to the Earth. The scale of energy available from the sun on the surface of the Earth dwarfs by orders of magnitude any other available power source. Energy from the sun arrives at Earth's surface at a rate of 120 PW, which amounts to nearly 3700 ZJ (3.7×10^{24} J) of energy per year. Compare this with the world annualized energy consumption in 2004 of 4.7×10^{20} J [1, 2]. Thought of in another way, more energy from the sun hits the surface of the Earth in one hour than the entire human consumption of energy in an entire year.

Other renewable energy technologies exist, and while they certainly make for attractive and viable power generation options, their total energy availability pales in comparison to the long-term needs of humanity. For example, the total power available in tidal currents and other tidally induced motion of water is near 2 TW. The total geothermal power available integrated over all the continental land mass is 12 TW, although the amount that could be efficiently collected is much smaller. Wind power only has 2-4 TW of power available for use. In these terms, solar energy is incident on the planet at a rate of 120,000 TW, and humanity's consumption rate is 10 TW in an annualized average.

Solar power is not a perfect resource. It is diffuse and intermittent, issues which lead to land usage and storage problems. In addition, solar photovoltaics have as yet failed to provide a cost-effective method of power conversion. However, its abundance and long-term stability and availability make solar energy an invaluable resource for investigation and implementation.

The materials under study in this work are used as the absorber layers in thin-film photovoltaic devices. Thin-film devices represent the "second generation" of photovoltaic devices, with crystalline silicon based devices considered the "first generation" [3]. Thin-film devices trade conversion efficiency for cheap materials and production costs. Current thin-film technologies include amorphous silicon, cadmium telluride, and the materials under study in this work: Cu-III-VI_2 alloys commonly referred to as copper indium diselenide (CIS) or copper indium gallium diselenide (CIGS). The specific alloy system under study in this work is $Cu(InGa)(SeS)_2$.

1.2 Disordered Materials Research and CIGSSe

In addition to applications in photovoltaics, these thin films also allow us to study the properties of disordered materials. Such materials lack the long range order that simplify analyses of crystalline materials. In fact, many of the properties of disordered materials have only been understood empirically. However, recent advances in computing technology and power have allowed more theoretical investigations into the properties of disordered materials.

CIGS is a polycrystalline material with a chalcopyrite crystal structure. Crystallite sizes vary from hundreds of nanometers to a few microns in a film of only a few microns in thickness. The properties of grain boundaries and other morphological properties of the film can have a large effect on device efficiencies. In addition to considerations of structural disorder from the polycrystalline nature of these materials, there is also a significant degree of compositional disorder. The best CIGS devices are grown with non-ideal cation stoichiometry, and are doped by their native intrinsic defects, no impurity doping is used. In a ternary compound there are 12 possible intrinsic defects, neglecting the possibility of defect complexes, and in CIS and related alloys, many of these defects have formation energies below 1 eV. Additionally, significant metastable behavior has been observed in these materials. Thus the nature of these materials provides a rich foundation for the study of the electronic and optical properties of defects in non-crystalline materials.

In light of these complicating aspects of material and electronic structure, CIGS devices hold the current world record for conversion efficiency for thin-film single-junction devices [4]. This has motivated an intense program of study to determine the properties of CIGS materials that contribute both advantageously and disadvantageously to the performance of these devices.

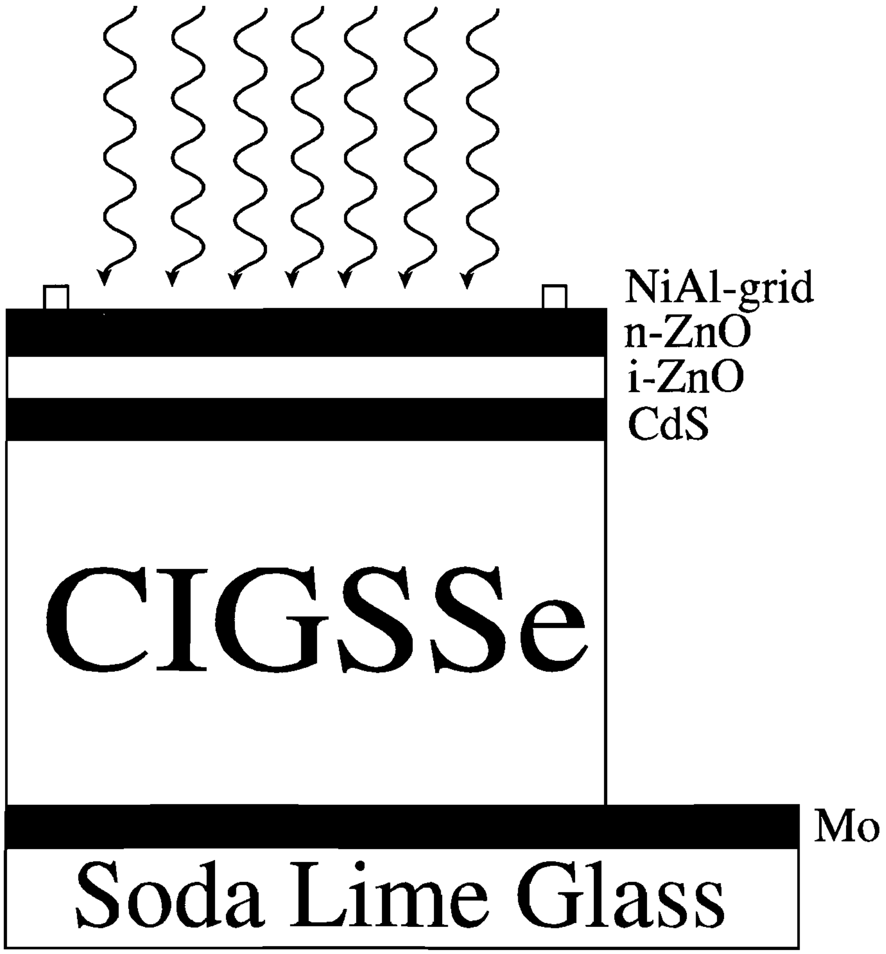

Figure 1.1. Typical CIGS sandwich structure. Devices are deposited on soda lime glass coated with 1 μm thick molybdenum as the back ohmic contact. ~2 μm thick CIGSSe absorbers are then deposited using a variety of techniques. A CdS buffer layer with a ~30nm thickness is deposited using a chemical bath deposition process. The device is finished with a 50 μm undoped ZnO layer and a 500 μm thick Al doped ZnO layer deposited by rf sputtering. Finally NiAl contact grid is added as the top contact using electron beam evaporation.

The relatively simple device structure of CIGS devices is shown in figure 1.1 with the deposition procedures shown in the caption. All films studied in this work have been deposited using elemental evaporation with no intentional grading of the composition of the films [5]. Highly optimized devices use a three-stage deposition process that results in less uniform compositions, and typically include graded bandgap profiles to improve carrier collection.

1.3 Context of this Work:

Wide-Bandgap Sulfur-Containing Thin-Film Devices

Of particular importance in a material for photovoltaic application is a bandgap with a good match to the solar spectrum. Photons with energies below the bandgap will typically not contribute to the output of the device due to poor absorption. However, photons with energies larger than the bandgap of the material will only contribute one electron-hole pair to the output of the device. Thus, any energy difference between a higher energy photon and the bandgap is lost to thermalisation. The optimum bandgap energy for terrestrial applications is 1.4 eV, wider than the record CIGS device referred to earlier.

Wide bandgap devices based on CIGS absorbers have, so far, failed to meet performance expectations. This is primarily due to rolloff of the open circuit voltage in devices with bandgaps larger than roughly 1.3eV [6]. The open circuit voltage should scale linearly with the bandgap. However, as shown in figure 1.2, this has not been the case.

Significant effort has been put into to understanding and overcoming these performance losses with increased gallium alloying. Early results by Heath et. al. showed the existence of a defect 0.8 eV above the valence band of the absorber, regardless of the gallium content [7, 8]. Because gallium alloying primarily moves the conduction band to higher energies, this defect effectively moves towards the middle of the gap as the bandgap is widened with gallium addition. Recombination efficiency increases

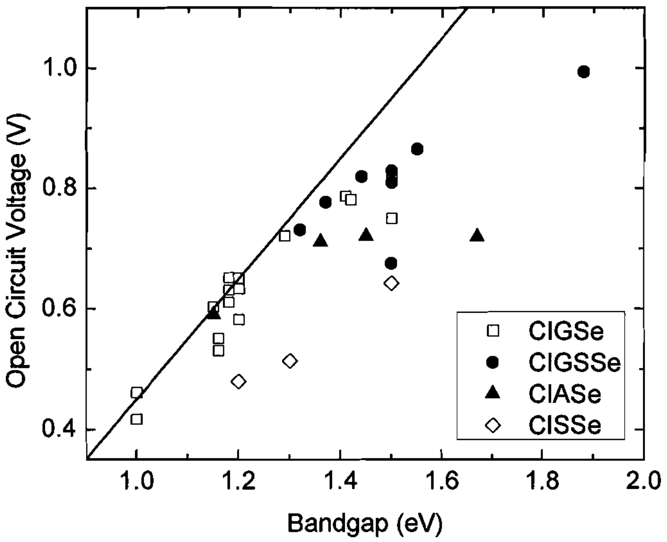

Figure 1.2. Open-circuit voltages versus bandgap for Institute of Energy Conversion grown devices with various absorber compositions. A straight line of E_{gap}-0.55eV has been added to guide the eye. A similar graph with data for a variety of deposition methods and cell structures can be found in the paper by Herberholz et. al. [6].

exponentially with proximity to the middle of the gap [9, 10]; thus this defect may become a detrimental recombination center for absorbers with high gallium contents.

It is for this reason that we have chosen to study the pentenary alloy system $Cu(In,Ga)(Se,S)_2$. The addition of sulfur to CIGSe increases the bandgap by moving the valence band to lower energies *and* moving the conduction band to higher energies. Our hope is that through more sophisticated alloying we will be able to overcome the losses encountered in wide-bandgap CIGS devices, and to elucidate the processes that lead to the loss of performance.

Notes

[1] U.S. Department of Energy, *International Energy Outlook 2007* (Energy Information Administration Office of Integrated Analysis and Forecasting, 2007).

[2] U.S. Department of Energy, *Basic Research Needs for Solar Energy Utilization*, (Energy Information Administration Office of Integrated Analysis and Forecasting 2005).

[3] M. A. Green, Prog. Photovolt.: Res. Appl. **9**, 123 (2001).

[4] K. Ramanathan, M. A. Contreras, C. L. Perkins, S. Asher, F. S. Hasoon, J. Keane, D. Young, M. Romero, W. Metzger, R. Noufi, J. Ward, and A. Duda, Prog. Photovolt.: Res. Appl. **11**, 225 (2003).

[5] M. Gossla and W. N. Shafarman, Thin Solid Films **480-481**, 33 (2005).

[6] R. Herberholz, V. Nadenau, U. Ruhle, C. Koble, H. W. Schock, and B. Dimmler, Sol. En. Mater. and Solar Cells **49**, 227 (1997).

[7] J. T. Heath, PhD dissertation, (University of Oregon, Eugene, 2002), p. 148.

[8] J. T. Heath, J. D. Cohen, W. N. Shafarman, D. X. Liao, and A. A. Rockett, Appl. Phys. Lett. **80**, 4540 (2002).

[9] R. N. Hall, Phys. Rev. **87**, 387 LP (1952).

[10] W. Shockley and W. T. Read, Phys. Rev. **87**, 835 LP (1952).

CHAPTER II

SOLAR CELL PERFORMANCE AND MATERIAL CHARACTERIZATION

2.1 Performance Characterization

The performance of a solar cell is characterized by the conversion efficiency of incident optical power into electrical power. In its most idealized form, a pn-junction solar cell functions as a diode with an additional current offset term due to the optically generated charge. In that case, the current response to voltage (JV curve) under illumination is governed by the equation [1-4]:

$$I = I_s(e^{qV/AkT} - 1) - I_L \tag{2.1}$$

where I_s is the diode saturation current, q the electron charge, A the diode ideality factor, k Boltzmann's constant, T the temperature, and I_L the current due to illumination. The ideality factor is a parameter that is used to account for the the main recombination pathways in the device and typically has a value between 1 and 2 [5, 6]. The diode saturation current can be represented as $I_s = I_{00} e^{\frac{-E_g}{AkT}}$, which implies a linear dependence of the open-circuit voltage on the bandgap. A schematic IV curve is shown in figure 2.1.

There are several parameters used to describe an IV-curve. The voltage at which there is no current flow through the device is the open-circuit voltage V_{OC}, and the current at zero applied voltage is the short-circuit current I_{SC}. By multiplying the current response of the device by the applied voltage one can determine the power generated by the device at each voltage. This power curve has a maximum which determines the maximum power point, i.e. the voltage V_m and the current I_m that optimize power output from the device. The ratio of the product of V_m and I_m to the product of V_{OC} and I_{SC} is called the *fill factor*. The fill factor is a useful parameter for describing the quality of the diode in the device. The fill factor can be significantly reduced when parasitic effects such as series and shunt resistances exist within the device [5, 6]. All of these individual performance parameters are combined to determine the most important performance parameter, the conversion efficiency of the device. Namely:

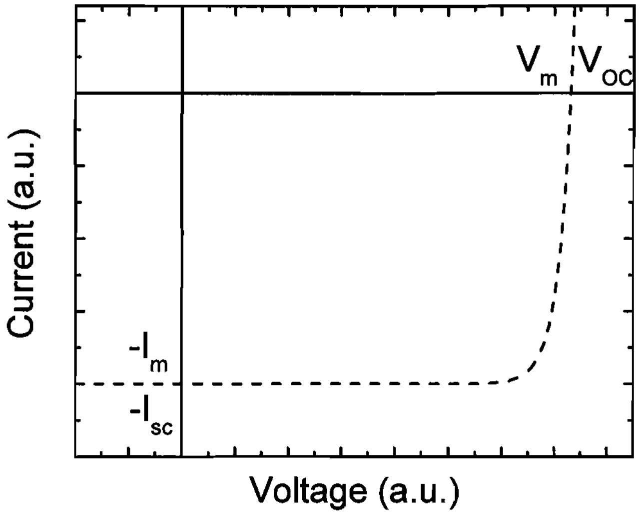

Figure 2.1. Schematic plot of the current response (dashed line) of an illuminated pn-junction solar cell device. Shown on the graph are the maximum power voltage V_m, the open circuit voltage V_{OC}, the maximum power current I_m, and the short-circuit current I_{sc}. The area of the grey rectangle represents the maximum power output from the device.

The efficiency η is

$$\eta = \frac{P_{out}}{P_{in}} = \frac{I_m V_m}{P_{in}} = FF \frac{I_{SC} V_{OC}}{P_{in}}, \tag{2.2}$$

where P_{in} is the incident optical power and P_{out} is the output power of the device.

The current record conversion efficiency for a CIGS thin-film solar cell device is 19.2% [7]. This small area (A=0.408cm^2) device has a short-circuit current density of J_{SC}=35.71mA/cm^2, an open-circuit voltage of V_{OC}=0.689V, and a fill factor of FF=78.12%. The device has roughly Ga/(In+Ga)=0.25, although this is an estimate because the depth profiles of the Ga and In were (intentionally) non-uniform throughout the device. It is interesting to note that this device has a bandgap of E_g=1.12eV, which is well below 1.42eV, the theoretical ideal bandgap for the AM1.5 solar spectrum [2].

2.2 Admittance Spectroscopy

Another extremely useful method of characterizing devices is admittance spectroscopy. The admittance (the inverse of the impedance *Z*) is a complex number whose real part is the *conductance G* of the device, and whose imaginary part is the *susceptance*. The susceptance term characterizes the ability of the material to store energy in either magnetic or electric fields. In the former case the susceptance is negative and the material is predominantly inductive, and in the latter case the susceptance is positive and the material is predominantly capacitive. The real and imaginary components of the current response are related to each other via the Kramers-Kronig relation, which links the real and imaginary parts of the current response, such that we can derive one from the other. This is a result of enforcing causality in dispersive systems [8, 9].

In a p-n junction device the admittance has both capacitance and conductance terms. Conductance terms arise due to series and parallel resistances due to the bulk resistivity of the material, contact resistance, shunting, and other sources. The capacitance arises from the depletion layer in the device, a region in the device that is depleted of free carriers and hence acts as a dielectric insulator. The charge configuration in a p-n junction in thermal equilibrium mimics that of a parallel place capacitor, thus the capacitance can be determined using the formula:

$$C = \frac{\varepsilon_r \varepsilon_0 A}{W}$$

(2.3) where ε_r is the relative dielectric constant of the material, ε_0 is the dielectric constant of free space, A is the area of the device, and W is the depletion layer width.

The capacitance of a junction is very sensitive to the amount of charge within the depletion region in the form of bulk and interface defect states, or even photo-excited charge. In addition junction capacitance measurements are applied to devices in their device configuration, as opposed to bare materials. This is a particularly important characteristic for CIGS-related materials, as the material properties of CIGS absorbers have been seen to have a detailed dependence on deposition parameters and their device configuration [10, 11].

2.2.1 Junction Capacitance

When two differently doped semiconductors are physically joined, the large difference in carrier concentrations between the two materials causes a diffusion current. Holes from the p-doped material diffuse into the n-type material, and electrons from the n-type material diffuse into the p-type material. As these carriers diffuse, they leave behind immobile acceptor and donor dopant ions, which create an electric field. The carrier diffusion current continues until it is exactly balanced by the drift current set up by the resultant electric field, and the device is said to be in thermal equilibrium.

As mobile carriers have diffused from each material into the other, there is a region around the junction in which there are now no free charge carriers. Thus, this region of material acts as a dielectric insulator, bounded on both sides by free charge carriers where there is no electric field to sweep them away. This is the configuration of a parallel plate capacitor, with the capacitance defined by equation

(2.3). However, unlike a typical fixed capacitor, the width of the depletion region, and hence the capacitance, is a detailed function of the charge density contained within the depletion region. For a one-sided abrupt junction (and also for Schottky junctions) the width of the depletion region varies as:

$$W = \sqrt{\frac{2\varepsilon_s (V_{bi} - V)}{qN_D}} \tag{2.4}$$

where V_{bi} is the built-in potential, V is any applied voltage bias (positive for forward bias, negative for reverse bias), q is the fundamental electron charge, and N_D is the concentration of charge within the depletion region. Thus, the capacitance of a junction is related to the concentration of charge due to defects or dopants within the depletion region. Note that this formulation assumes that all charge change occurs at the edge of the depletion region, namely at W.

This simplified formulation of junction capacitance works well for intentionally doped crystalline semiconductor materials. However, the thin-films studied for this thesis are poly-crystalline materials, i.e. materials that are made up of many small closely packed crystallites, and which display no long range order. These disordered materials are known to have significant native densities of states within the bandgap of the material, the understanding of which plays a vital role in understanding the properties of the material and the devices made from it. Thus we must reexamine the capacitance response for a material with a continuous density of states within the bandgap.

At its most fundamental, capacitance is ratio of a change of charge in response to a change in voltage:

$$C = \frac{\partial Q}{\partial V} \tag{2.5}$$

In order to understand the capacitance response of an arbitrary distribution of charge states within the bandgap, it is necessary to use the Poisson equation:

$$-\frac{d^2\psi}{dx^2} = \frac{\rho}{\varepsilon} \tag{2.6}$$

where ψ is the electrostatic potential, ρ is the charge distribution, and ε is the dielectric constant of the material. Poisson's equation determines the electrostatic potential due to a particular charge distribution $\rho(x)$. It is essentially a differential form of Gauss's law from electrostatics [9]. The advantage of this formulation of the capacitance is that it does not require one to specify a charge distribution, and hence can be applied to non-uniform charge distributions. Other methods of deriving the full admittance from the Poisson equation exist [12, 13], but these derivations require the assumption of slowly varying material properties, which does not suit our purposes.

Using the boundary conditions in the region far from the interface that $\psi(\infty)=0$, and that $d\psi/dx=0$ (also at ∞), we find that the potential at the interface layer can be written:

$$\psi(0) = -\int_0^\infty x\frac{\rho(x)}{\varepsilon}dx \tag{2.7}$$

When a small voltage δV is applied across the device, this simply modifies the relative potential at the interface (the bulk remains effectively at $\psi(\infty)=0$), thus the differential change in voltage can be written:

$$\delta V = \int_0^\infty x \frac{\delta\rho(x)}{\varepsilon} dx \tag{2.8}$$

The differential charge response to such a change in voltage is simply the integrated change in the charge distribution due to the voltage change, or:

$$\delta Q = A \int_0^\infty \delta\rho(x) dx \tag{2.9}$$

where A is the area of the device and $\delta\rho(x)$ is the differential change in charge density due to δV. Thus, for an arbitrary charge distribution in the depletion region, we can calculate the capacitance via equation (2.5):

$$C = \frac{\partial Q}{\partial V} = \frac{A \int_0^\infty \delta\rho(x) dx}{\int_0^\infty x \frac{\delta\rho(x)}{\varepsilon} dx} = \frac{\varepsilon A}{\langle x \rangle}. \tag{2.10}$$

Here, ⟨x⟩ is the first moment of the charge response, or the weighted average position of all the charges able to respond at the measurement frequency and temperature.

2.2.2 Emission Energy Dependence

To account for the frequency and temperature dependence of the charge response, it is sufficient to introduce a thermally activated emission time limit for the response of the states within the bandgap, thus establishing an energy threshold above which defects within the bandgap are too deep to respond to the ac-pertubation voltage. This "emission energy" is defined as:

$$E_e = k_B T \ln(\nu / \omega) \tag{2.11}$$

where k_B is Boltzmann's constant, T is the measurement temperature, ω is the angular frequency of the measurement, and υ is the thermal emission prefactor. This equation has its origins in detailed balance considerations of carrier emission from and capture into a deep defect. Namely, in a semiconductor, four processes control the occupation of a deep defect: capture of holes from the valence band, emission of holes to the valence band, capture of electrons from the conduction band, and emission of electrons to the conduction band. These processes are shown schematically in figure 2.2. The rates for each of these processes are:

$$\begin{aligned} r_1 &= \nu\sigma_p p\ f \\ r_2 &= e_p\ (1-f) \\ r_3 &= \nu\sigma_n n(1-f) \\ r_4 &= e_n f \end{aligned} \tag{2.12}$$

where ν is the average thermal hole velocity, σ_x is the capture cross section for each type of carrier, e_x is the emission probability from the defect for each carrier type, N_d is the defect density per unit volume, p and n are the free hole and electron densities respectively, and *f* is the occupation probability given by a Fermi-Dirac-like distribution. In thermal equilibrium, the capture and emission processes to each respective band balance in detail, i.e. $r_1=r_2$, and $r_3=r_4$ [14]. If we then consider a Fermi energy coincident with the defect energy, we can solve these equations for the emission rates as a function of the properties of the defect:

$$\frac{1}{\tau_n} = e_n = v\sigma_n N_c e^{(E_d-E_c)/kT} \qquad \frac{1}{\tau_p} = e_p = v\sigma_p N_v e^{(E_v-E_d)/kT} \tag{2.13}$$

where τ_x is the characteristic time for capture and emission processes to occur.

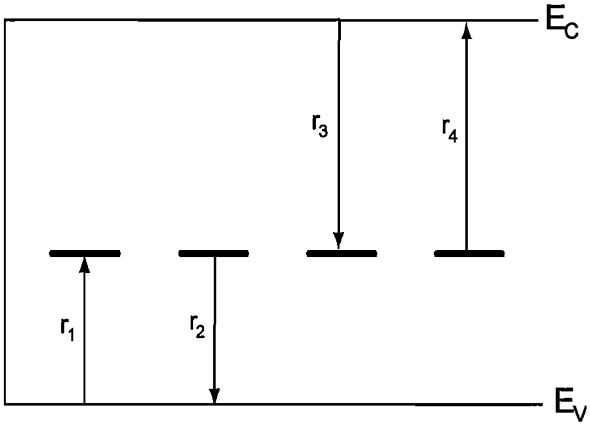

Figure 2.2. Schematic diagram of charge emission and capture processes from a single defect level.

For a one-sided device, the capture and emission processes of the majority carriers in the more intrinsic side of the device will dominate over the minority carrier signal in most circumstances. Thus I will restrict discussion to the hole emission rate of the defect, as that is the majority carrier in the materials of interest in this work.

The emission rate of the defect defines a characteristic time for a defect to emit charge to and capture charge from the valence band. This imposes limits on the ability of the defect to "follow" an ac-voltage perturbation at a particular temperature. We can rewrite (2.11) in the form of (2.13) to get:

$$\frac{1}{\tau_{meas}} = \omega_{meas} = \nu e^{-\frac{E_e}{k_B T}} \tag{2.14}$$

Thus we see that there is a characteristic time both for carrier capture and emission from a defect for an ac-measurement. If the timescale of the measurement is smaller than the timescale for capture and emission processes, the defect will not contribute to the overall capacitance of the device, and so this modifies the measurable charge distribution that is able to respond on the timescale of the measurement. Specifically:

$$\rho_{meas}(x) = q \int_{E_F}^{E_V + E_e} g(E,x)dE\,. \tag{2.15}$$

Thus, as the emission energy of the measurement is changed, the amount of charge that is able to respond changes via the integration limits of (2.15). This introduces a spatial cutoff position x_e below which charge cannot respond due to the band bending in the depletion region. As the bands bend away from the Fermi level the emission energy crosses the Fermi level, defining the position x_e. Between the junction and the cutoff position the charge distribution cannot respond to the applied ac-voltage on the time scale of the measurement, thus there is essentially no charge change in this spatial region. Using these capacitance techniques as a function of emission energy, we can then create an energetic "map" of a device, which aids in understanding the material and guides us in further measurements.

2.2.3 Measuring Capacitance

The actual measurement of differential capacitance is very straightforward using a lock-in amplifier. Lock-in amplifiers are phase sensitive detectors that are able to very accurately measure a signal that is varying with a known frequency. An ac-voltage signal generated by the lock-in is used to probe the device, and the lock-in detects the phase shifted current signal responding at the frequency of the voltage probe signal. By analyzing the in-phase and out-of-phase components of the response, we can determine the conductance and capacitance of the device under the measurement conditions.

We assume a simple circuit diagram for the bulk material of the device under study, as shown in figure 2.3 [15]. The sample is considered to have a bulk capacitance C_P, as well as a series resistance component R_S which may arise, for example, from the bulk resistivity plus any contact resistance. R_S is generally very small under these conditions compared to the other impedances in the device and will generally be neglected.

The current response to an ac-voltage $V=A\exp(i\omega t)$ will be:

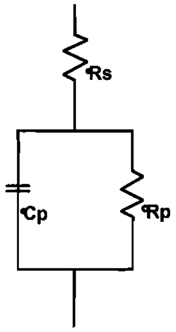

Figure 2.3. Equivalent circuit model for the device. R_s is the series resistance, R_p the bulk resistance, and C_p the bulk capacitance.

$$I = \frac{V}{R_P} + C\frac{dV}{dt} = \frac{A}{R_P}\cos(\omega t) - A\omega C\sin(\omega t). \tag{2.16}$$

Thus there are both in-phase and out-of-phase components to the signal, the coefficients of which are related to the components of the idealized circuit model of the material.

By calibrating the lock-in using a pure capacitor of known value, we can determine quantitatively the capacitance component of the current response of our sample to an applied ac-voltage as a function of the frequency of the applied ac-voltage as well as the sample's temperature. For these measurements we use a Stanford Research Systems SR850 digital lock-in amplifier, which has an ac-voltage source that can range from the millihertz range to 100 kHz. The ac-voltage is input to an adder that combines the ac-voltage with an independently controlled DC offset voltage, as well as voltage pulses for use in transient measurements. This combined voltage is applied to the sample device, which is in a temperature controlled dry-nitrogen cryostat, and the output is fed to a Stanford Research Systems SR570 current preamplifier. The preamplifier converts the current response from the device to a voltage, which is then fed back to the lock-in amplifier for lock-in detection. This measurement apparatus is diagramed in figure 2.4.

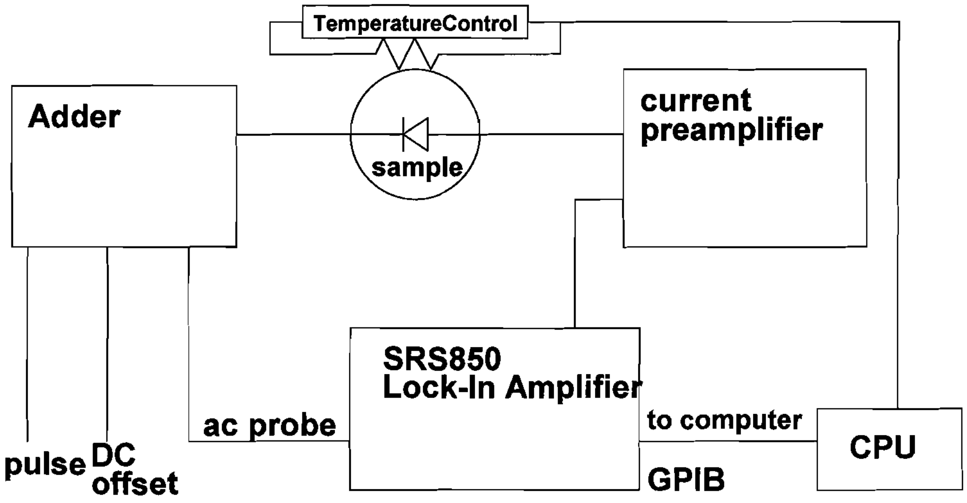

Figure 2.4. Measurement apparatus used for capacitance measurements. The temperature and lock-in are computer controlled.

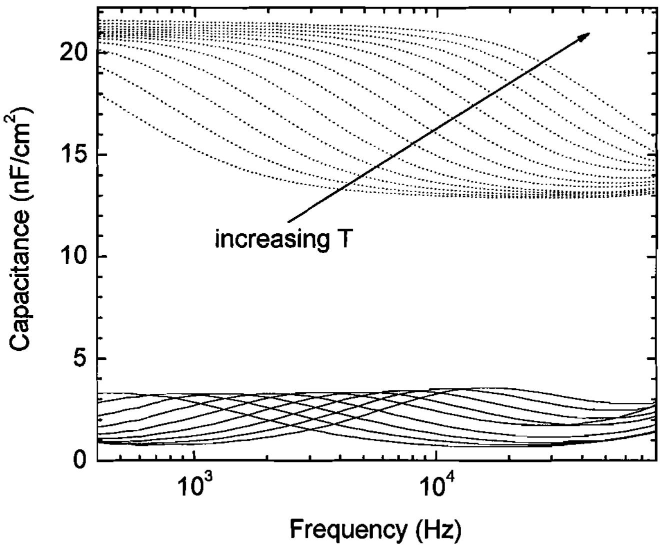

Figure 2.5. Example capacitance (dotted lines) and conductance/ω (solid lines) curves collected over a range of temperatures and frequencies for a CIGSS thin-film solar cell device. The capacitance and conductance/ω curves are related through the Kramers-Kronig relations. In this case, the location of the step in capacitance is the same as the peak in conductance/ω.

Typical results of capacitance measured over a range of frequencies at various temperatures are shown in figure 2.5. The steps in capacitance as the frequency is increased are common features of admittance spectra. These steps occur as a particular source of charge response becomes unable to respond on the timescale of the measurement. By increasing the temperature of the measurement, the frequency at which the charge is unable to respond increases, and the step moves to a higher frequency. Thus, by recording the frequency and temperature of the steps in capacitance, one can determine the "activation energy" of the step, which gives information about the energy depth of the feature that causes the step. This analysis is performed using an Arrhenius plot, as shown in figure 2.6. If we examine equation (2.14), we see that the measurement frequency and temperature are intimately related to the thermal emission prefactor and energy depth of the defect that is responding. The slope m of the linear fit to the Arrhenius data versus 1000/T is related to the activation energy E_a of the defect by $E_a=1000\cdot m\cdot k_B\cdot ln(10)$. The thermal emission prefactor is related to the y-intercept of the linear fit by $\upsilon=exp(y_0)$.

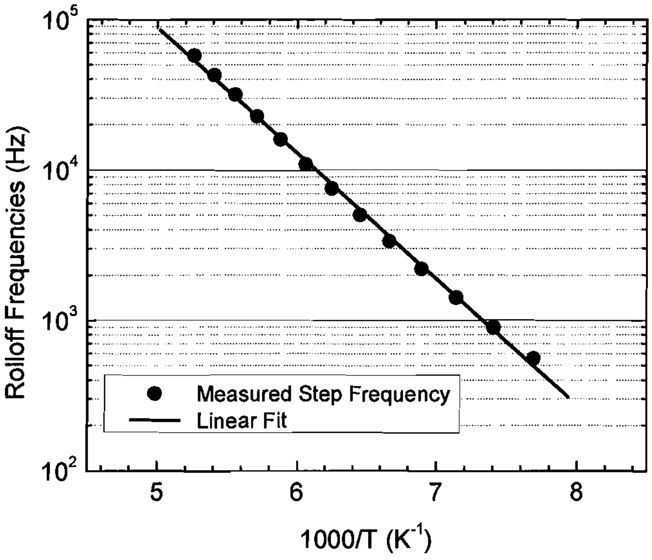

Figure 2.6. Example Arrhenius plot for the data shown in figure 2.5. The rolloff frequency of each step is plotted versus 1000/T. The slope of this line gives information about the activation energy of the step in capacitance, and the y-intercept gives the thermal emission prefactor. Values for this plot are E_A=172meV and $\nu=10^9$ sec^{-1}.

It is important to remember that the capacitance arises due to changes in the charge response centroid, as per equation (2.10). Thus, we are able to gain information about the source of particular steps in the capacitance spectra by calculating the widths associated with them. For example, at low temperatures and high frequencies, it is possible to freeze-out the ac-response from all the defects as well as the free carriers in the device [16]. The capacitance measured under these conditions comes entirely from the geometry of the device and is related to the thickness of the device by

$$C_g = \frac{\varepsilon A}{d} \qquad (2.17)$$

where d is the thickness of the device and C_g is the geometric capacitance. This effect is not always observed, since it may require very high frequencies for the temperature range available to us.

Above the geometric capacitance limit, the first step is then the activation not of a defect, but of the conductivity within the material. The free carrier response turns on when the measurement frequency becomes smaller than the inverse of the dielectric response time, $\rho\varepsilon$. Just below the frequency where the free carriers are able to respond, the capacitance at the top of the capacitance step gives a reliable estimate of the depletion width of the device, since only the free carriers at the edge of the depletion region are able to respond to the applied ac-voltage.

Upon further reduction of the measurement frequency, we are often able to observe defect activation steps at larger emission energies. These "deep" defects typically have activation energies between 100meV and 300meV in CIGS devices, and do not generally show any correlations with the growth parameters of the devices, including gallium content [17]. This latter observation may be due to the way gallium alloying affects the band structure of CIGS. Ga addition increases the bandgap of the material mainly by moving the conduction band edge to higher energy while leaving the energy of the valence band edge nearly the same. Because the defects are exchanging charge with the valence band as they respond, the lack of correlation between the Ga fraction and the activation energies indicates that the deep defects are not changing their energetic position relative to the valence band due to Ga alloying. However, sulfur alloying increases the bandgap by moving both the valence band and conduction band away from each other. Thus, we can expect that if the deep defects are fixed to an isoenergetic feature in the bandgap that is not related to the band edges, we may see a significant dependence of the activation energy with sulfur alloying. I will address these results in chapter 4.

There are several sources of measurement error that can cause anomalous results with admittance spectroscopy. Perhaps the most difficult to avoid is shunting of the device. Shunting can occur due to physical damage to the film during deposition, handling, or mounting for measurement. A shunt effectively reduces the effective bulk resistance of the idealized circuit to nearly zero, even though it may just be a single pathway. Thus the dissipation, or the ratio of the conductance signal to the capacitance signal, becomes extremely large. For large dissipations it becomes difficult for the lock-in to accurately separate the two phases of the current response, which can lead to crossover between the conductance and capacitance channels of the output. All of the methods measuring capacitance also rely on sophisticated knowledge of both the area of the device and the dielectric constant. For this thesis I will use ε=11.7, which is within the standard range exhibited in the literature [18].

Recording the capacitance (or conductance) of the device as a function of frequency and temperature is able to provide valuable information about the energetic characteristics of defect states in the material that can affect the performance of the device. In addition, the capacitance values give information about the geometric thickness of the device, as well as the depletion width. Finally, C-T-ω spectra provide a guide for further measurements that use junction capacitance to determine other device and material properties.

2.3 Spatial Defect Profiling

We saw in equation (2.3) that the capacitance is a function of the width of the depletion region, and in equation (2.4) that the width of the depletion region is a function of both the applied voltage and the trap density contained in the depletion region. We can take advantage of these relationships to *spatially* profile the defect concentrations within the active layer of our devices.

2.3.1 Capacitance-Voltage Profiling

Certainly one of the most well-known methods for creating a spatial profile of the defect distribution is capacitance-voltage (CV) profiling [1]. CV profiling is based on the measurement of the capacitance of the device over a range of applied DC biases. To calculate the CV defect density determined by measuring C at dc voltages V_1 and V_2, we rewrite equation (2.8) as

$$\delta V = \int_{W_1}^{W_2} x \frac{\delta\rho(x)}{\varepsilon} dx \approx \frac{W\rho(W)dW}{\varepsilon} \tag{2.18}$$

where *W* is the average width between $W(V_1)$ and $W(V_2)$. This calculation assumes (through the limits on the integral) that all the charge change is happening at the edge of the depletion region. Thus we calculate:

$$\frac{dC}{dV} = -\frac{\varepsilon A}{W^2}\frac{dW}{dV} = -\frac{C^3}{\varepsilon A^2 \rho(W)} \tag{2.19}$$

which is readily rearranged to produce:

$$\rho(W) = -\frac{C^3}{\varepsilon A^2 \left(\frac{dC}{dV} \right)} \tag{2.20}$$

An example curve of capacitance versus voltage data and the resulting CV profile is shown in figure 2.7.

CV profiling is a useful tool for determining dopant profiles in crystalline semiconductor materials. However, when there is a significant density of deep states or interface states, the interpretation of CV data can be difficult. We have already seen that for materials with a significant density of deep states within the bandgap

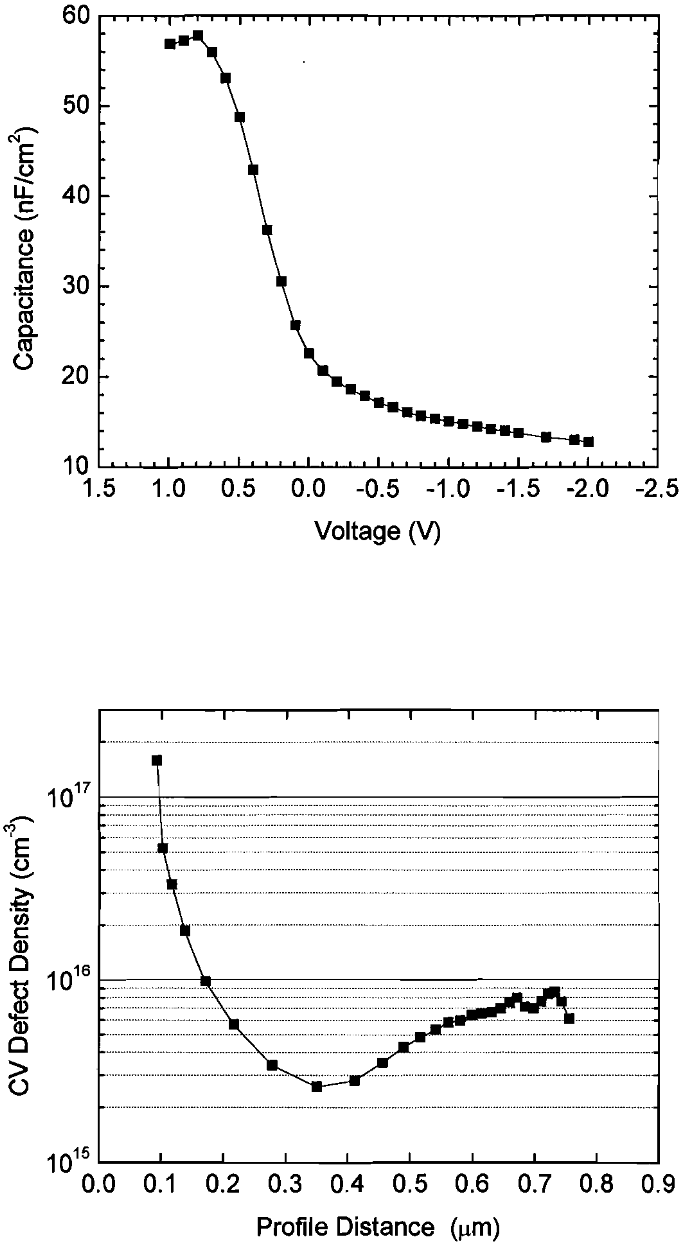

Figure 2.7. a. Raw capacitance versus voltage data. Negative voltage values represent a reverse bias. **b.** Resultant CV defect profile obtained using equation (2.20).

there may be a charge response that comes from a deep state crossing the Fermi level deep inside the depletion region. Thus the assumption that all of the charge change with applied voltage is occurring at the edge of the depletion region breaks down, and we can no longer simply apply equation (2.3) to determine the depth. The deep state contribution to the capacitance will also artificially inflate the measured value of the free carrier density. Since this is an important parameter for device operation, it is vital to be able to obtain an accurate value for it. Additional concerns arise when significant spatial non-uniformities exist within the device.

In addition, CV profiling is a quasi-static measurement, in that the DC voltage is changed relatively slowly as the measurement is run. Thus, there is an ill-defined time constant for the measurement coming from both the measurement frequency and the time between the changes in the applied bias voltage. If deep states and interface states change charge on a similar time-scale as the measurement, results will be ambiguous, and will depend on the rate at which the measurement was made.

2.3.2 Drive Level Capacitance Profiling

Drive level capacitance profiling (DLCP) is a method that was designed to overcome many of the drawbacks inherent in a CV profiling measurement [10, 19, 20]. DLCP uses the same principles as admittance spectroscopy, but extends them to the non-linear capacitance response to large ac-voltages. Standard techniques for measuring capacitance use very small ac-voltages and assume a linear charge response. DLCP uses a series of larger ac-voltages such that a nonlinear charge response is expected. Thus:

$$\frac{dQ}{dV} = C_0 + C_1 dV + C_2 (dV)^2 + \ldots \tag{2.21}$$

As we will see, the higher order coefficients give us valuable information about the true defect density.

First we must revisit the capacitance response of a continuous density of trap states within the bandgap of a material. Again our approach will be to integrate the Poisson equation making minimal assumptions about the density of responding states. This development follows that given by Heath et al. [20]. When dealing with continuous densities of states in the bandgap, it is important to recall the emission energy cutoff given by equation (2.11) and the position cutoff x_e defined by the crossing of the emission energy and the Fermi level. Between the interface and the position cutoff, deep states do not have time to respond to the ac-voltage perturbation.

As before, the dc potential at the interface due to the junction is written:

$$\psi_0(0) = \int_0^\infty x \frac{\rho_0(x)}{\varepsilon} dx = \frac{1}{\varepsilon}\left(\int_0^{x_e} x\rho_0(x)dx + \int_{x_e}^\infty x\rho_0(x)dx \right) \tag{2.22}$$

which is then separated into two terms, one covering the area between the junction and the position cutoff, and one covering the area beyond the position cutoff that is able to respond. For an abrupt junction, a small voltage δV increases the potential at the interface to a new value

$$\psi(0) = \psi_0(x) + \delta V \,. \tag{2.23}$$

This shifts the position cutoff location further from the junction to a new location $x_e+\delta x$, where x_e is the still the position cutoff before adding the voltage δV. This

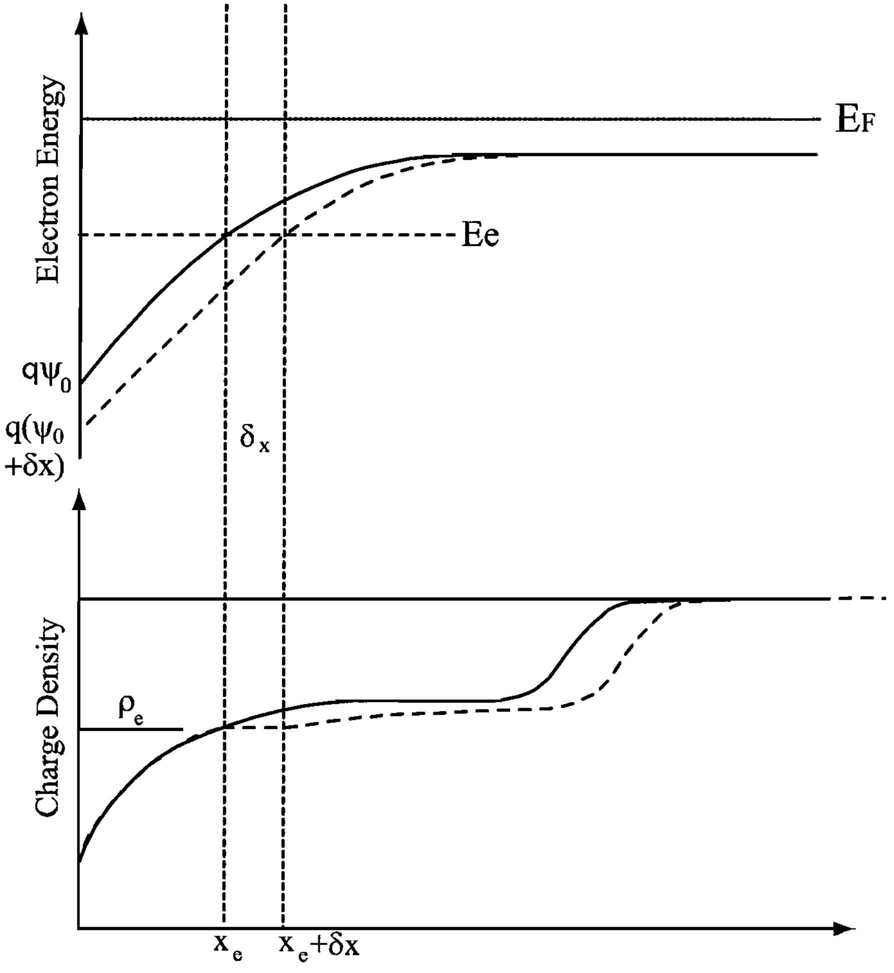

Figure 2.8. Schematic spatial profiles of electron energy and charge density during a drive-level measurement.

formulation is illustrated in Figure 2.8.

Because the δV we are applying is an ac-perturbation, it is only applied for a time $1/\omega$. Due to the emission times of charge from the deep defects, defects deeper than the emission energy of the measurement (and hence closer to the junction than

x_e) will not be able to change their occupation on the time scale of the measurement. In addition, defects between x_e and $x_e+\delta x$ will be emission limited, and will have a constant charge density across that region equal to the charge density at x_e before the perturbation, denoted ρ_e. Thus, at a time t=1/ω after the perturbation is applied the dc potential at the interface is now:

$$\psi(0)=\frac{1}{\varepsilon}\left(\int_0^{x_e} x\rho_0(x)+\int_{x_e}^{x_+ +\delta x} x\rho_e dx+\int_{x_e+\delta x}^{\infty} x\rho(x)dx\right) \tag{2.24}$$

If the material properties do not change rapidly on a scale of δx, the final integral in (2.23) will be the same as the final integral in (2.22). This makes sense because while the integration limits on the two integrals are different, the charge densities at those limits are nearly the same, or $\rho(x)\approx\rho_0(x-\delta x)$. Then the total change in depletion charge in response to the voltage perturbation δV is the charge in the region between x_e and $x_e+\delta x$, which is equal to

$$\delta Q=\rho_e A\delta x. \tag{2.25}$$

This is the charge response to an ac-voltage perturbation for an arbitrary density of states. The capacitance response do an ac-voltage perturbation is still $\delta Q/\delta V$, and we have just to relate δV and δx.

Calculating out the middle integral in (2.24) keeping in mind $\rho(x)\approx\rho_0(x-\delta x)$ and that ρ_e is a constant, we have

$$\psi(0)=\frac{1}{\varepsilon}\left(\int_0^{x_e} x\rho_0(x)+\frac{\rho_e}{2}\left((x_e+\delta x)^2-x_e^2\right)+\int_{x_e+\delta x}^{\infty} x\rho_0(x-\delta x)dx\right). \tag{2.26}$$

We can then calculate $\delta V = \psi(0) - \psi_0(0)$ and we have

$$\delta V = \frac{\rho_e}{2\varepsilon}\left((x_e + \delta x)^2 - x_e^2\right) + \delta x \int_{x_e}^{\infty} \frac{d^2\psi}{dx^2} dx = \frac{\rho_e}{2\varepsilon}\left((x_e + \delta x)^2 - x_e^2\right) - \delta x F_e \qquad (2.27)$$

where F_e is the magnitude of the electric field at the point x_e. This equation is quadratic in δx and can be solved for δx in terms of δV. We then have

$$\delta x = \left(\frac{\varepsilon F_e}{\rho_e} - x_e\right)\left(1 - \sqrt{1 + \frac{2\rho_e \varepsilon \delta V}{(\varepsilon F_e - \rho_e x_e)^2}}\right). \qquad (2.28)$$

This can be expanded in powers of δV which gives

$$\delta x \approx \frac{\varepsilon}{(\varepsilon F_e - \rho_x x_e)} \delta V - \frac{1}{2} \frac{\rho_e \varepsilon^2}{(\varepsilon F_e - \rho_e x_e)^3} \delta V^2 + \ldots. \qquad (2.29)$$

We can now calculate the capacitance response of an arbitrary distribution of charged defects to an ac-voltage perturbation as

$$\frac{\delta Q}{\delta V} \approx \frac{A\rho_e \varepsilon}{(\varepsilon F_e - \rho_e x_e)} - \frac{1}{2} \frac{A\rho_e^2 \varepsilon^2}{(\varepsilon F_e - \rho_e x_e)^3} + \ldots \qquad (2.30)$$

Equating terms in (2.30) and (2.21) we see that the coefficients of the expansion in (2.21) can be written:

$$C_0 = \frac{A|\rho_e|\varepsilon}{(\varepsilon F_e - \rho_e x_e)}, \qquad (2.31a)$$

$$C_1 = \frac{A\rho_e^2 \varepsilon^2}{(\varepsilon F_e - |\rho_e| x_e)^3}, \qquad (2.31b)$$

and thus we can determine the defect density at the position x_e as

$$N_{DLCP} \equiv -\frac{C_0^3}{2q\varepsilon A^2 C_1} = \frac{|\rho_e|}{q}. \qquad (2.32)$$

Absolute value signs have been added to the charge densities so as to account for the sign of the charge in both p- and n-type materials.

Now we have in our hands a measurement that is capable of revealing the true defect density that is able to dynamically respond to an applied ac-voltage perturbation. It is important to note a few of the experimental details of such a measurement.

First, when we considered the application of a voltage perturbation to the dc potential at the interface in equation (2.23), we only considered the perturbation in a single direction. This was done on purpose so as to ensure that the position of x_e did not move *towards* the junction, which would severely complicate the analysis. To account for this in the experiment, one must apply a small additional dc bias offset to ensure that the ac-voltage perturbation only negatively biases the device, thus keeping x_e constant.

It is also important to take into account the emission energy dependence of the responding deep defects. The temperature and frequency of the measurement can be varied, thus changing the emission energy of the measurement. We can use this as a tool to study the activation of defect response as a function of emission energy, exactly as we did with admittance spectroscopy. The density of defects able to respond at a given emission energy is

$$\frac{|\rho_e|}{q} = p + \int_{E_F^0}^{E_V+E_e} g(E, x_e)\,dE \qquad (2.33)$$

where p is the free carrier density and E_F^0 is the bulk Fermi level. Thus at small emission energies (high frequency, low temperature) it may be possible to freeze out all deep defect response. Under these conditions the defect density measured is simply the free carrier response. As the emission energy is increased by either increasing the temperature, lowering the frequency, or both, the emission energy can move through a deep defect response, which will contribute to the measured defect density.

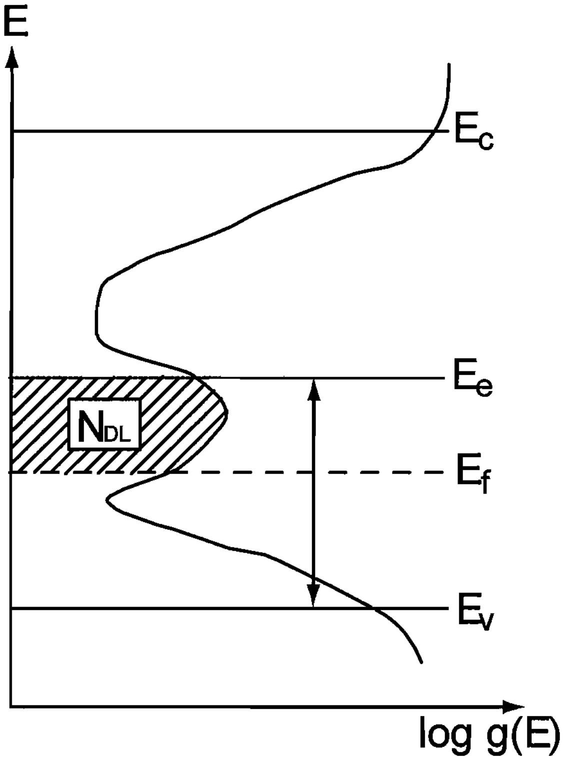

Figure 2.9. Diagram showing the defect response range of a DLCP measurement given by equation (2.33).

Finally, because we can change the depletion width and position cutoff using a dc offset, we can create a defect profile of the device. The defect response is plotted against the centroid of the charge response, given by the C_0 term of equation (2.31a):

$$\langle x \rangle = \frac{\varepsilon A}{C_0}. \tag{2.34}$$

Because the centroid of the charge response contains the C_0 term from equation (2.31a), it does have factors that contain the electric at the position cutoff point inside the device. However, at a given emission energy it is believed that these terms will not vary much as a function of dc bias. Thus changes in $\langle x \rangle$ will reflect true changes in the defect response. However, $\langle x \rangle$ is the centroid of the charge response, and its overall value can be influenced by large densities of defects within the depletion region. Thus, it is inappropriate to treat $\langle x \rangle$ as a "true" profile depth, but one must regard it as a relative position.

Finally, DLCP densities require very accurate knowledge of the sample area and dielectric constant. As mentioned before I will use $\varepsilon=11.7$, which is within the range of experimentally determined values for CIGS materials.

2.4 Reverse Bias Metastabilities in CIGS

Application of reverse bias at or near room temperature has been noticed to cause an increase in the junction capacitance of CIGS solar cell devices [21-24]. The measured increase in acceptor density appears to occur only within a small region near the junction, which gives rise to a non-uniform defect profile through the absorber region of the device. These metastabilities have been observed to have a detrimental impact on the performance of the device. Using the characterization techniques discussed in this chapter, we can study the effects of reverse bias stressing on CIGS devices and their defect profiles [25].

The devices in this particular study are high efficiency CIGS thin-film solar cell devices grown at both the Institute of Energy Conversion (IEC) at the University of Delware, and the Institut für Physikalische Elektronik (IPE) in Stuttgart, Germany. CIGS films grown at the IEC were grown using elemental evaporation techniques with no intentional grading of the composition of the films. A typical baseline structure for these devices is a soda lime glass substrate coated with a molybdenum back contact. This is followed by a ~1μm CIGS absorber layer. Optimized CIGS devices have a Ga content near 30%. ZnO buffer layers and ITO window layers are then deposited, followed by a Ni-Al collection grid.

The devices were characterized in their original state, "State A", and then subjected to a specific treatment procedure to produce degraded states. Devices were characterized using CV and DLC profiling techniques as well as illuminated JV characterization to determine performance parameters.

The treatment procedure consisted of:

1. Hold the sample in the dark at 370K and 0V bias for about 1 hour. The complex admittance of the device was monitored to ensure that the sample had returned to its initial state before treatment. We refer to this process as the annealing process.

2. Bias stress the sample at the treatment temperature. Stressing of the device consisted of holding the device at a particular temperature and exposing it to a certain value of reverse bias for a specified time. Thus we have three treatment parameters: treatment temperature, bias magnitude, and exposure time. It is important to note that the sample is kept in the dark for these steps.
3. Quench the sample while still under bias to a measurement temperature where the properties of the device no longer change despite exposure to bias. The temperature below which the properties of the device remained stable regardless of bias (i.e. the device neither annealed nor further degraded) was experimentally determined to be ~250K. Typically we employed a characterization temperature of 200K.
4. Characterize the admittance of the device as a function of frequency at the desired measurement temperature. DLC and CV profiling was then employed over a range of frequencies chose to characterize any features seen in the admittance spectrum. In addition the performance of the device was characterized using UV+red JV techniques [26].

Use of UV+red light in the JV characterization allowed a determination of the device properties in the bulk due to the weakly absorbed red light, while a component of weak UV light was used to overcome the often observed "red kink" problem that arises due to double-diode behavior while using red light at low temperatures.

The treatment procedure in step 3 was carried out several times for different control parameters. The effects of bias stressing increased proportionally to all three of the parameters discussed. In addition, qualitatively similar results were obtained for all three treatments, as shown in figure 2.10a-c.

As can clearly be seen from the profiles shown in figure 2.10a-c, application of

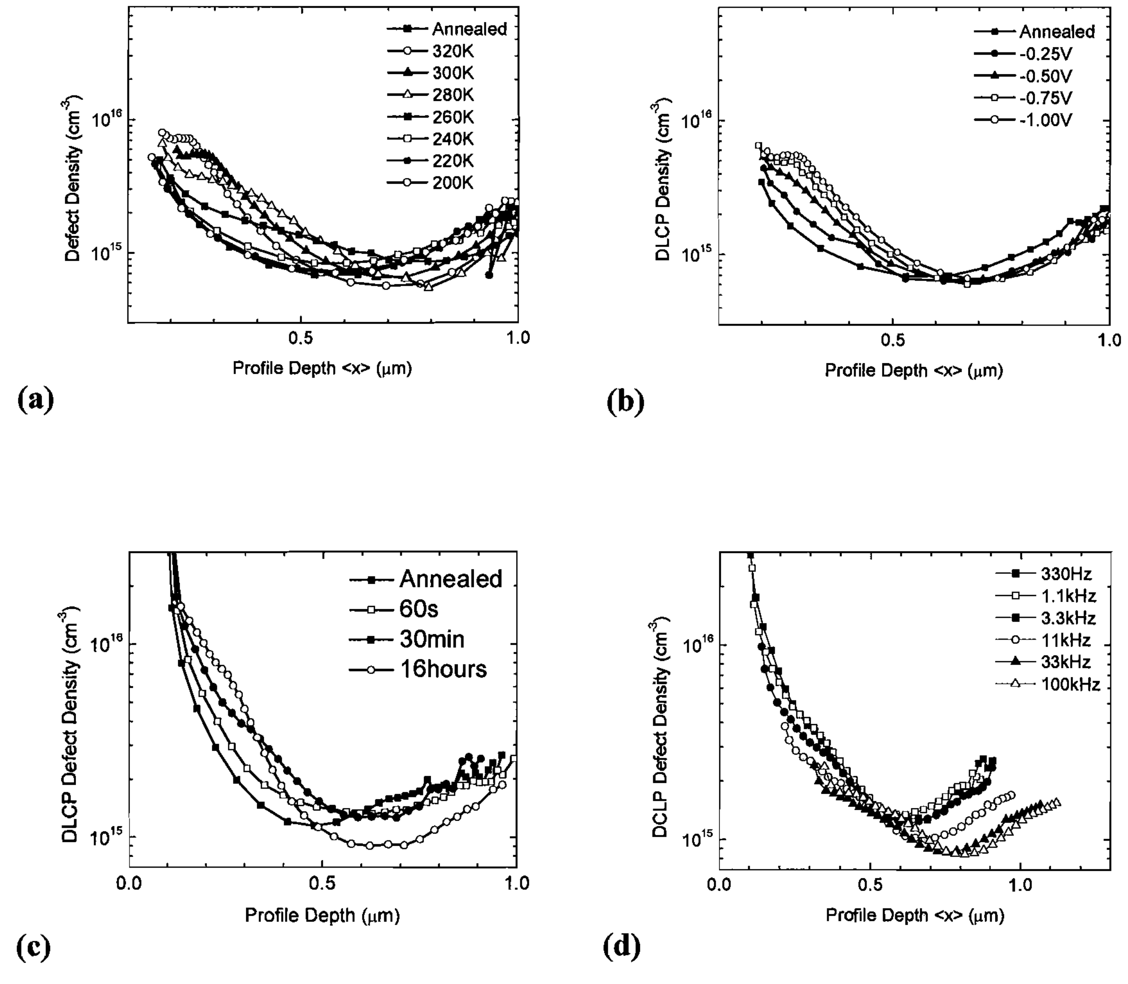

Figure 2.10. a. Exposure temperature series. Samples were exposed to -1V for 1 hour at the stated temperatures. **b.** Voltage magnitude series. Devices were exposed to the stated voltages at 300K for 1 hour. **c.** Exposure time series. Devices were exposed to -1V at 300K for the specified time. **d.** Detailed frequency dependence of the defect profiles for the 30min -1V 300K treatment from the time series shown in figure 2.10c.

reverse bias stress causes a marked increase in the measured DLCP density in the profile region near the junction. In addition we see a decrease in the DLCP density in the region further from the device junction. However, the profile range of the measurements appears to remain approximately constant, which implies that there is little change in the total charge density within the depletion region. In addition, areal integration of the profiles to deduce the effect of the degradation on the total defect density in the film showed no clear trend with the degradation parameters.

Because of the rapidly varying spatial profiles given by the DLC profiling measurements, we must be careful in directly interpreting defect densities from the measured profiles. By fitting the defect profiles using a numerical modeling program, we are able to deduce the degradation mechanism that gives rise to the profile shifts we observe.

My advisor developed a numerical modeling program to simulate such DLCP measurements that utilizes a modified Noumerov method of solving the Poisson equation [13] with an emission time limit to account for the emission energy dependence of the defect response. The electronic properties of the sample are specified in three spatial regions with input parameters including

- The shallow acceptor density within the three regions
- The energy position, width, and magnitude of a Gaussian deep defect band within each region
- A thermal emission cutoff energy to account for the emission time limit of deep defects

- The positions of the boundaries between the regions
- The degree of mixing between the regions.

Using these modeling parameters we were able to obtain detailed fits to the annealed and degraded DLC profiles using a simple shallow acceptor to deep acceptor interconversion mechanism. The inspiration for fitting with such a mechanism has recently been published, and will be discussed below [27].

In Fig. 2.11 we demonstrate that many of the qualitative changes in the DLCP data of Fig. 2.10c can be reproduced using this interconversion mechanism. In this simulation we located two boundaries at 0.15 μm and 0.8 μm from the barrier interface between the three spatial "regions", but mixed these regions into each other over length scales of 0.07 and 0.3 microns, respectively. We set the shallow and deep acceptor densities in the region farthest from the barrier at 1×10^{15} cm^{-3}, and in the intermediate region both shallow and deep acceptor densities were taken to be 6×10^{14} cm^{-3}. In the region nearest the barrier interface, the densities of shallow and deep acceptors were varied in such a way that the total remained constant (3×10^{16} cm^{-3}), only the ratio of shallow and deep acceptors was changed. That is, in this set of simulations we consider that most of the change in defect profiles with treatment to reverse bias is caused by *interconversion* of shallow acceptors to deep acceptors.

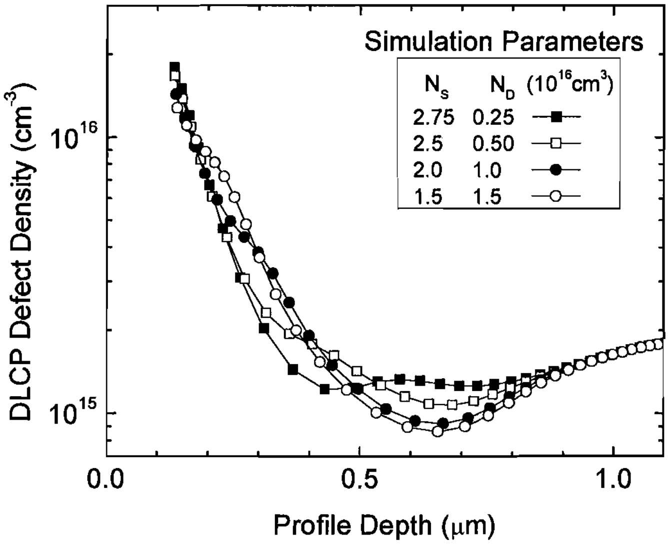

Figure 2.11. Qualitative fits that reproduce the effect of reverse bias stressing in CIGS thin films.

We were also able to obtain detailed fits to the annealed and degraded spectra for the devices exposed to -1V at 300K for specified amounts of time. These detailed fits required a slight adjustment of the size of the region closest to the barrier, which may indicate a small degree of defect *creation* in addition to interconversion in this region. These detailed fits are shown in figure 2.12.

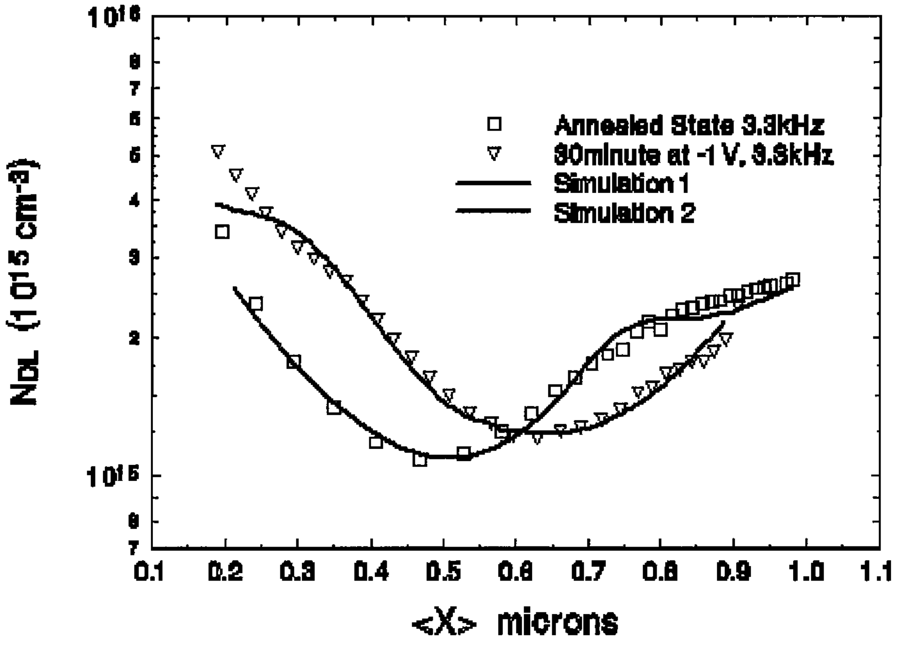

Figure 2.12. Detailed fits for the annealed and degraded defect profiles.

The lines shown in figure 2.12 are the simulated DLC profiles. The actual defect distributions that give rise to these profiles are shown in figure 2.13. In these graphs the dotted line shows the shallow acceptor distribution, and the solid line shows the deep acceptor distribution. It is clear from these profiles that in the annealed state, shallow acceptors are the dominant feature in the near junction region of the defect profiles. Upon exposure to reverse bias stress, these defects convert to deep defects in such a way as to keep their total density constant.

Lany and Zunger recently published theoretical work detailing the dynamics of the Se-Cu divanacy complex (V_{Se}-V_{Cu}) and its relationship to light and bias induced metastabilities in CIGS [27]. This defect complex can exist in two different structural configurations, a shallow donor $(V_{Se}\text{-}V_{Cu})^{+}$, or a shallow acceptor

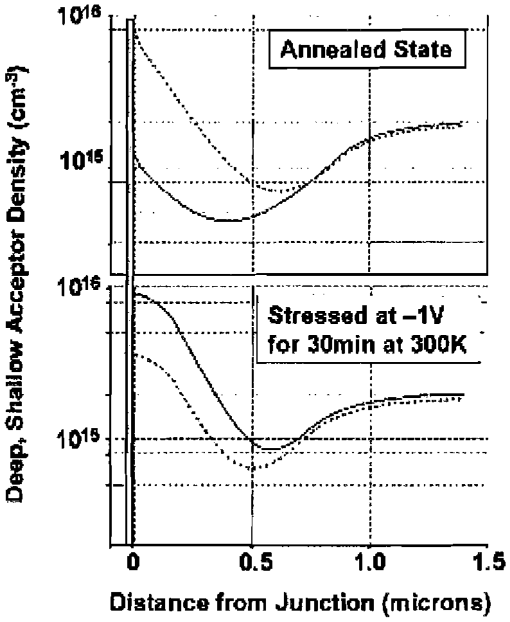

Figure 2.13. Actual defect profiles that give rise to the DLC profiles shown in figure 2.12. The solid lines represent the deep acceptor densities, while the dashed lines represent shallow acceptor densities.

$(V_{Se}\text{-}V_{Cu})^{0/1\text{-}/2\text{-}/3\text{-}}$ which has multiple charge states. These vacancy complexes co-exist with each other in equilibrium in CIGS.

The donor and acceptor states of the divacancy complex can interconvert between their respective states through either electron or hole capture as well as a thermal activation step over an energy barrier associated with a structural reconfiguration. That is:

$$\begin{aligned}(V_{Se}-V_{Cu})^{+}+e^{-} &\rightarrow (V_{Se}-V_{Cu})^{-}+h^{+}\\ (V_{Se}-V_{Cu})^{-}+2h^{+} &\rightarrow (V_{Se}-V_{Cu})^{+}\end{aligned} \tag{2.35}$$

show the conversion of a donor state to an acceptor state upon electron capture, and an acceptor to donor conversion upon capture of *two* holes. It should be noted that these conversions can also work in the reverse direction, albeit with a significant energy barrier (several k_BT at room temperature). Thus it is by tracking the availability of excess carriers of both type as well as the temperature of the device that the authors explain metastabilities due to red light exposure, current injection, blue light exposure, and application of reverse bias. I will restrict discussion to the

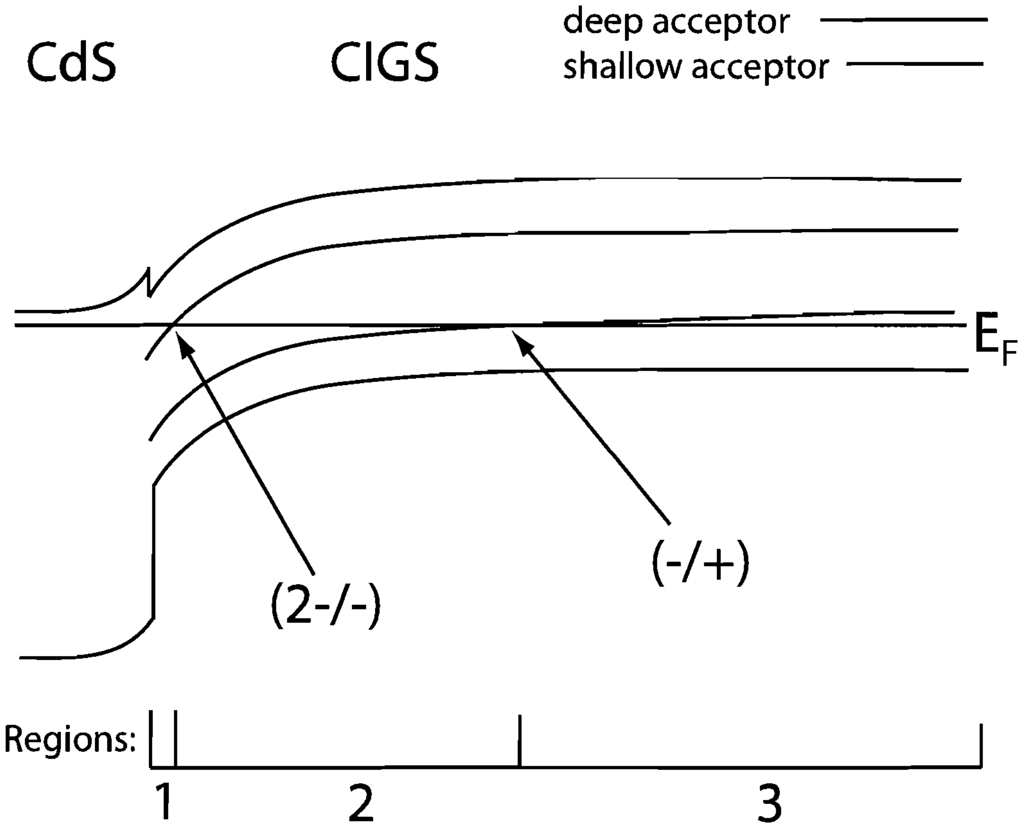

Figure 2.14. Schematic diagram of a CdS/CIGS junction showing the preferred charge and configuration states of the divacancy complex as a function of the Fermi level.

case of reverse bias stressing.

In the annealed state of the device, the equilibrium charge state of the (V_{Se}-V_{Cu}) complex depends on the local Fermi level. Thus, due to the band bending inherent in the device due to the junction, the charge state of the vacancy complex will change as a function of distance from the barrier junction. Near the barrier junction, the complex will exist in the double acceptor state $(V_{Se}\text{-}V_{Cu})^{2-}$ due to the Fermi level position high in the bandgap, labeled region 1 in figure 2.13. Where the energy position of the double acceptor crosses the Fermi level, the vacancy complex will relax into the shallow acceptor configuration $(V_{Se}\text{-}V_{Cu})^{-}$, which lies near the valence band maximum, labeled region 2. This configuration will persist until its own energy crosses the Fermi level, which typically occurs deep into the absorber layer. Through the rest of the device, where the energy level of the acceptor configuration is above the Fermi level, will be preferentially populated with $(V_{Se}\text{-}V_{Cu})^{+}$ compensating donors, labeled region 3.

With this spatial distribution of $(V_{Se}\text{-}V_{Cu})$ complexes in hand, we can determine the effects of reverse bias stressing on the material. Reverse bias increases the width of the depletion region and depletes the material of free electrons and holes. However, in the region near the junction, the applied reverse bias increases the band bending of the junction, thus increasing the region where the doubly negative deep acceptor state is the preferred configuration. Thus this defect model is able to explain the shallow to deep accepter interconversion mechanism we used to fit our reverse bias stressed DLC profiles. However, Lany and Zunger expect that the primary effect of bias stressing will be the conversion of shallow donors to shallow acceptors near the interface of regions 2 and 3 in figure 2.13. In fits to our

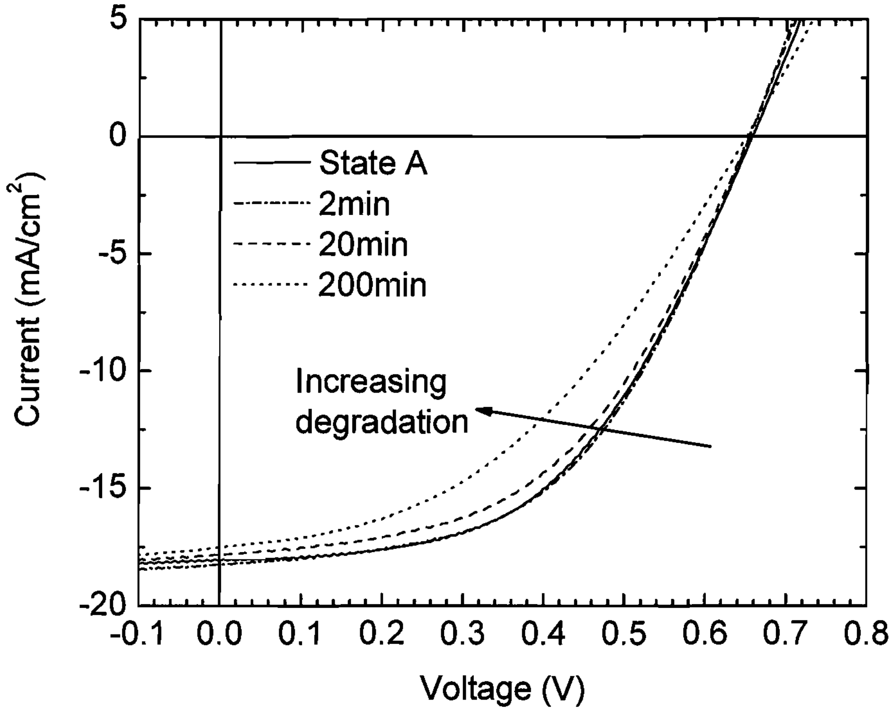

Figure 2.15. Red+UV illuminated JV curves for CIGS in various states of reverse bias induced degradation.

degradation data, we do not require any changes to be made to the acceptor densities outside of the region near the junction.

The 2^- and 3^- deep acceptor configurations of the divacancy complex exist as optical levels within the bandgap of the device approximately 1eV above the valence band maximum. Indeed, optical levels near 0.8eV have been observed for CIGS devices with varying amounts of Ga content [28]. It has been posited that these levels may be responsible for rolloff of the open circuit voltage of CIGS devices with high Ga content, thus affecting the performance of wide bandgap devices [29].

In measuring the performance properties of our CIGS devices in various states of bias stress, we saw a significant dependence of the fill factor on the degree of bias stressing, as shown in figure 2.14. With -1.5V stressing at 320K for increasing amounts of exposure time, the fill factor decreased monotonically to 82% of its original relaxed state value in 200 minutes. This seems to be due to a loss in the quality of the junction between the CIGS and CdS layers and has been observed before [30-32]. These authors modeled the affect of a negatively charged p+ layer near the interface that increases the probability of tunneling enhanced recombination near the junction, detrimentally affecting the fill factor in their devices. This model of a p+ layer close to the barrier junction is in agreement with the doubly negative deep acceptor configuration of the (V_{Se}-V_{Cu}) divacancy complex.

Notes

[1] S. M. Sze, *Semiconductor Devices, physics and technology* (John Wiley & Sons, Inc., 2002).

[2] A. Luque and S. Hegedus, *Handbook of Photovoltaic Science and Engineering*, Hoboken, 2003).

[3] T. Markvart and L. Castaner, *Photovoltaics, fundamentals and applications* (Elsevier Ltd., New York, 2003).

[4] R. H. Bube, *Photovoltaic Materials* (Imperial College Press, London, 1998).

[5] U. Rau, Appl. Phys. Lett. **74**, 111 (1999).

[6] S. S. Hegedus and W. N. Shafarman, Prog. Photovolt.: Res. Appl. **12**, 155 (2004).

[7] K. Ramanathan, M. A. Contreras, C. L. Perkins, S. Asher, F. S. Hasoon, J. Keane, D. Young, M. Romero, W. Metzger, R. Noufi, J. Ward, and A. Duda, Prog. Photovolt.: Res. Appl. **11**, 225 (2003).

[8] J. S. Toll, Phys. Rev. **104**, 1760 (1956).

[9] J. D. Jackson, *Classical Electrodynamics* (John Wiley & Sons, Inc., New York, 1998).

[10] J. D. C. J. T. Heath, and W. N. Shafarman, Journal of Applied Physics **95**, 1000 (2004).

[11] D. Mencaraglia, S. O. Saad, and Z. Djebbour, Thin Solid Films **431-432**, 135 (2003).

[12] D. L. Losee, J. Appl. Phys. **46**, 2204 (1975).

[13] J. D. Cohen and D. V. Lang, Phys. Rev. B **25**, 5321 (1982).

[14] J. G. Simmons and G. W. Taylor, Phys. Rev. B **4**, 502 (1971).

[15] J. Kneisel, K. Siemer, I. Luck, and D. Braunig, J. Appl. Phys. **88**, 5474 (2000).

[16] J. Lee, J. D. Cohen, and W. N. Shafarman, Thin Solid Films **480-481**, 336 (2005).

[17] J. T. Heath, in *Department of Physics* (University of Oregon, Eugene, 2002), p. 148.

[18] C. Rincon, M. A. Arsene, S. M. Wasim, F. Voillot, J. P. Peyrade, P. Bocaranda, and A. Albacete, Mat. Lett. **29**, 87 (1996).

[19] C. E. Michelson, A. V. Gelatos, and J. D. Cohen, Appl. Phys. Lett. **47**, 412 (1985).

[20] J. T. Heath, J. D. Cohen, and W. N. Shafarman, Thin Solid Films **431-432**, 426 (2003).

[21] R. Herberholz, U. Rau, H. W. Schock, T. Haalboom, T. Godecke, F. Ernst, C. Beilharz, K. W. Benz, and D. Cahen, Eur. Phys. Jour. Appl. Phys. **6**, 131 (1999).

[22] P. Zabierowski, U. Rau, and M. Igalson, Thin Solid Films **387**, 147 (2001).

[23] M. Igalson, M. Bodegard, L. Stolt, and A. Jasenek, Thin Solid Films **431-432**, 153 (2003).

[24] U. Rau, K. Weinert, Q. Nguyen, M. Mamor, G. Hanna, A. Jasenekc, and H. W. Schock, Materials Research Society Proceedings **668**, H.9.1.1 (2001).

[25] A. Halverson, J. Mattheis, U. Rau, and J. D. Cohen, in *Conference Record of the 2006 IEEE 4th World Conference on Photovoltaic Energy Conversion* (IEEE, Hawaii, USA, 2006), Vol. 1, p. 519.

[26] A. O. Pudov, J. R. Sites, M. A. Contreras, T. Nakada, and H.-W. Schock, Thin Solid Films **480-481**, 273 (2005).

[27] S. Lany and A. Zunger, J. Appl. Phys. **100**, 1 (2006).

[28] J. T. Heath, J. D. Cohen, W. N. Shafarman, D. X. Liao, and A. A. Rockett, Appl. Phys. Lett. **80**, 4540 (2002).

[29] R. Herberholz, V. Nadenau, U. Ruhle, C. Koble, H. W. Schock, and B. Dimmler, Sol. En. Mater. and Solar Cells **49**, 227 (1997).

[30] A. Niemegeers, M. Burgelman, R. Herberholz, U. Rau, D. Hariskos, and H.-W. Schock, Prog. Photovolt.: Res. Appl. **6**, 407 (1998).

[31] M. Igalson, A. Kubiaczyk, and P. Zabierowski, in *2001 MRS Spring Meeting*, San Francisco, USA, 2001), Vol. 668.

[32] M. Igalson, in *2007 MRS Spring Meeting* (MRS, San Francisco, USA, 2007), Vol. 1012.

CHAPTER III

SUB-BANDGAP OPTICAL CHARACTERIZATION

3.1 Introduction to Optical Measurements

Optical measurements are a powerful tool for exploring the density of states within a semiconductor material. The interactions of light with matter depend heavily on the properties of the material, in particular the band structure, defects, and occupation thereof. Due to the continuous tunability of the energy of light and the ability to filter it down to monochromatic spectra, it is an excellent tool for examining the energy structure of complicated materials.

The most fundamental optical measurements are those of absorption, reflection, and transmission. Due to conservation of energy, only two of these quantities must be measuredand the third is given for free. Because the absorptance of a material is difficult to measure directly, the transmittance and reflectance are typically recorded, and the absorptance is calculated from these quantities. The absorptance however, is simply the imaginary part of the dielectric function, which characterizes the electronic band structure of a material. Ellipsometry measurements, which record the amplitude and phase shift of reflected light as a function of the angle of incidence, can yield detailed information about the a thin film's complex dielectric function. Spectroscopic ellipsometry records similar data, but over a range of wavelengths of incident light [1].

Despite their extreme sensitivity and applicability, ellipsometry measurements falter when attempting to examine the sub-bandgap optical absorption spectra. Thus several other measurements have been developed to optically measure sub-bandgap densities of states and to determine their effect on material and device performance.

Several measurements have been developed that can be used to measure the sub-bandgap optical absorption spectra. Transient photocapacitance (TPC) spectroscopy and transient photocurrent (TPI) spectroscopy are two complementary methods that allow us measure spectra similar to sub-bandgap optical absorption spectra. Other methods that have been applied to amorphous silicon related devices are the constant photocurrent method (CPM), photothermal deflection spectroscopy (PDS) [2], and dual beam photoconductivity . TPC and TPI however, are applicable to CIGS materials in their device configuration, that is, with all the functional material layers that are used to finish the device into a solar cell [3, 4]. This is a significant advantage in that the material properties of CIGS are thought to change significantly based on their environment. In addition, because TPC and TPI measure the charge carriers created upon absorption of a photon, the measurements are sensitive to the charge collection dynamics that occur after the photon is absorbed.

3.2 Transient Photocapacitance and Transient Photocurrent Spectroscopies

From an electrical perspective, the experimental setup of TPC and TPI is nearly identical to that of a DLTS measurement [5]. Capacitance transients in DLTS are induced using voltage (and sometimes light) pulses. First the device is held in equilibrium under reverse bias. A forward bias "filling pulse" is superimposed on the reverse bias which changes the depletion width and facilitates electron emission/hole capture from states that have been pushed above the Fermi-level. After the filling pulse is over, the device returns to the quiescent reverse bias. In this bias configuration we now have a non-equilibrium occupation of deep states due to the filling pulse, which manifests as a change in capacitance due to the extra trapped charge. As these carriers are thermally emitted to the valence band, the capacitance of the junction returns to thermal equilibrium. This is observed as a capacitance transient, the time constant of which is related to the energy depth of the defect as per equations (2.11). The effect of the pulse configuration on the defect occupation is diagramed in figure 3.1. It is interesting to point out that during the voltage filling pulse charge capture processes dominate the active processes in the device. During the return to the quiescent reverse bias, emission processes dominate. Thus, a DLTS pulsing regime is able to decouple the thermal emission and capture processes, which is a very useful tool for defect analysis.

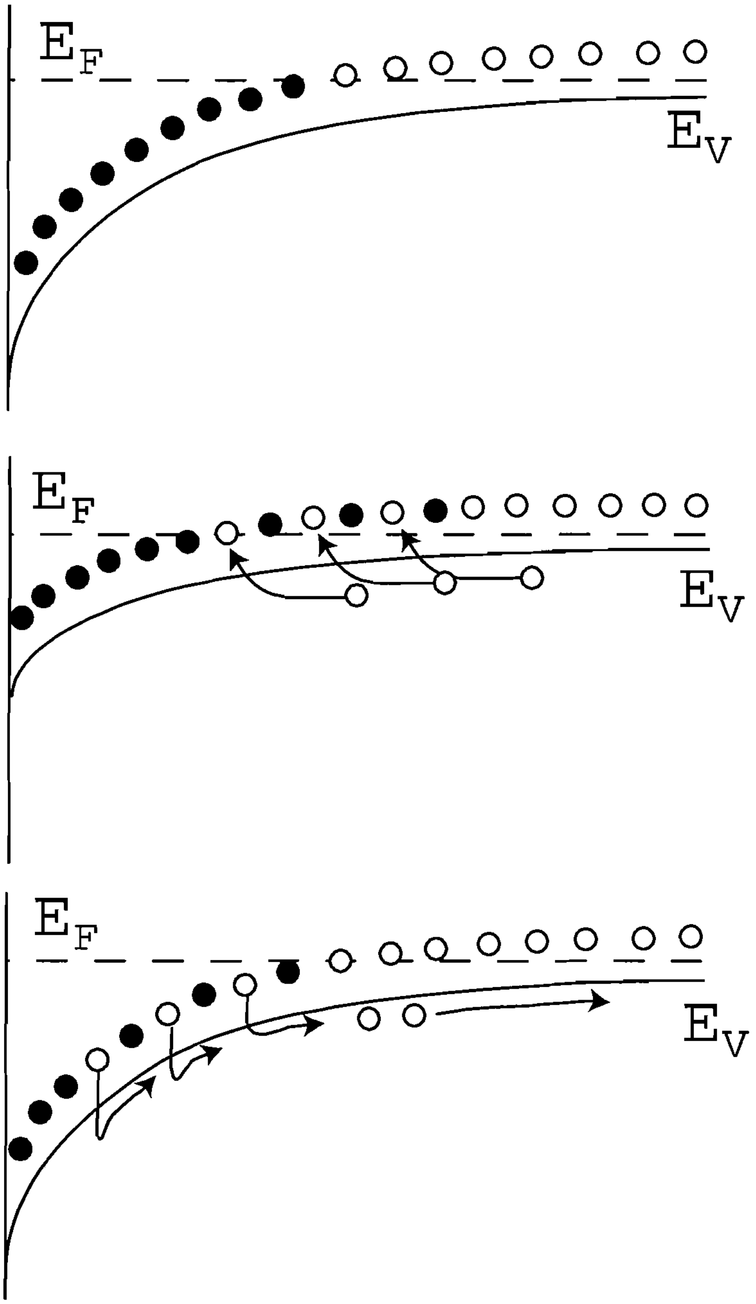

Figure 3.1. Defect occupation, and charge capture and emission during DLTS-type voltage pulses.

Because the measurement is performed in the dark, the capacitance transient seen in a DLTS measurement is due to purely thermal emission from the non-equilibrium defect occupation. Thus, minority carrier emission can be very difficult to observe, and the energy depth that can be observed is limited by the temperature and time constant of the measurement. TPC and TPI overcome this limitation through the use of sub-bandgap monochromatic light to enhance the energetic resolution of the measurement, independent of thermal processes.

In a TPC/TPI measurement, the device is pulsed in exactly the same manner as in a DLTS measurement. However, while a DLTS measurement is done in the dark, every other transient in a TPC/TPI measurement is exposed to low levels of monochromatic sub-bandgap light [6, 7]. This enhances the emission processes during the thermal transient by optically emitting trapped charges in addition to the thermal processes. These light-off and light-on transients are integrated over boxcars, and the signals are subtracted, thus negating any thermal component in the resultant difference signal. This difference signal, normalized to the incident photon flux, is the TPC/TPI signal:

$$S(E_{opt}) = \frac{\int_{t_1}^{t_2} C_{light}(t)dt - \int_{t_1}^{t_2} C_{dark}(t)dt}{\Phi(E_{opt})}. \tag{3.1}$$

By varying the wavelength of the monochromatic light, we can collect a TPC/TPI *spectrum*. This data collection scheme is shown in figure 3.2.

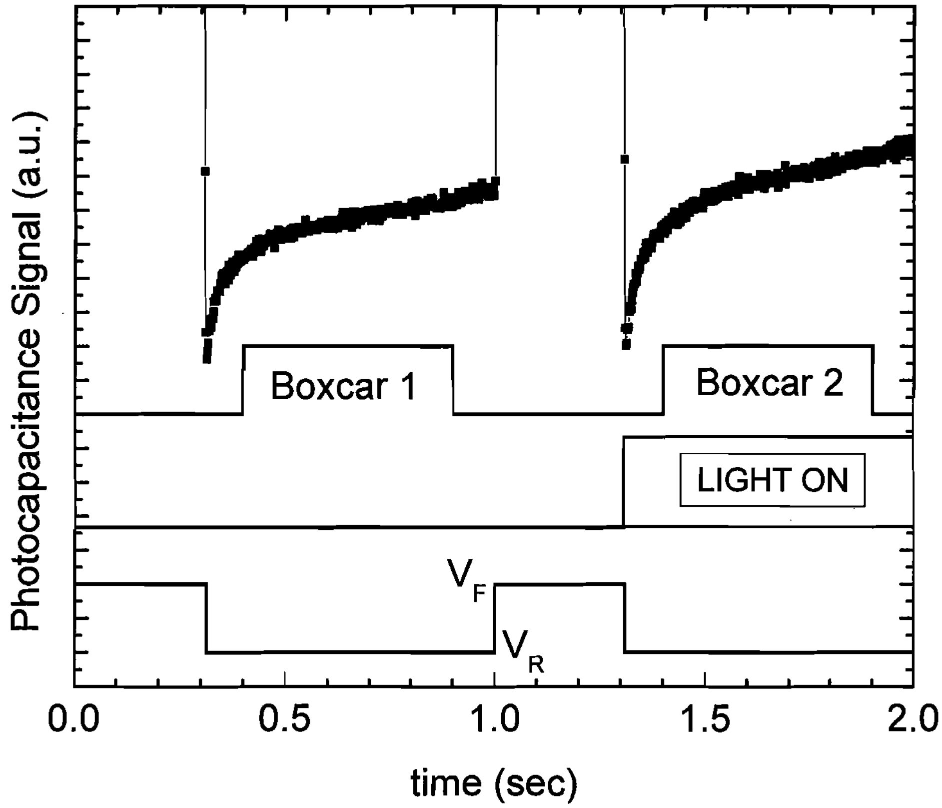

Figure 3.2. Measurement timing and schematic capacitance transient data giving rise to a TPC/TPI signal.

A TPC spectrum is very similar to what a true sub-bandgap optical absorption spectrum should look like, albeit with some very important differences that arise due to the sensitivity of the signal to the charge collection characteristics of the device. Optical absorption at a specific photon energy E_{opt} is governed by the equation

$$P(E_{opt}) = \int \left|\langle i|ex|f\rangle\right|^2 g_{unocc}(E) g_{occ}(E - E_{opt}) dE \qquad (3.2)$$

where g_{unocc} are unoccupied states, g_{occ} are occupied states, and $|\langle i|ex|f\rangle|$ is the optical matrix element between the states. Thus, a photon takes an electron from an occupied state and puts it into an unoccupied state, modified by the probability of such a transition to occur, the information for which is contained in the optical matrix element. Thus, the absorption signal is a convolution of the electron occupied states and the unoccupied states into which they transition. Because we are monitoring the dark and light-enhanced *capacitance* transients, it is important to break (3.2) up into two parts, transitions from the valence band into unoccupied states within the gap, and transitions from occupied gap states into the conduction band. In the former transition, an electron from the valence band is put into a gap state and leaves a hole behind in the valence band, and in the latter an electron is put into the conduction band, leaving behind a trapped hole in a defect state. Thus we have two separate contributions to a TPC signal:

$$\begin{aligned} P_p(E_{opt}) &= \int_{E_v+E_e}^{E_v+E_{opt}} \left|\langle i|ex|f\rangle\right|^2 g(E)g_v(E-E_{opt})dE \\ P_n(E_{opt}) &= \int_{E_c-E_{opt}}^{E_v+E_e} \left|\langle i|ex|f\rangle\right|^2 g(E)g_c(E+E_{opt})dE \end{aligned} \tag{3.3}$$

where P_p is the signal that leaves free holes to be collected, and P_n is the signal that leaves free electrons to be collected. Each integral is a function both of the optical energy of the sub-bandgap light and the emission energy of the measurement. In most analyses, the optical matrix element is assumed to be a constant, or at least slowly varying over the sub-bandgap energy range. This follows with many properties of disordered materials that are broadened in comparison to their crystalline counterparts [8]. A diagram of the transitions due to optical absorption seen in TPC and TPI measurements is shown in figure 3.3.

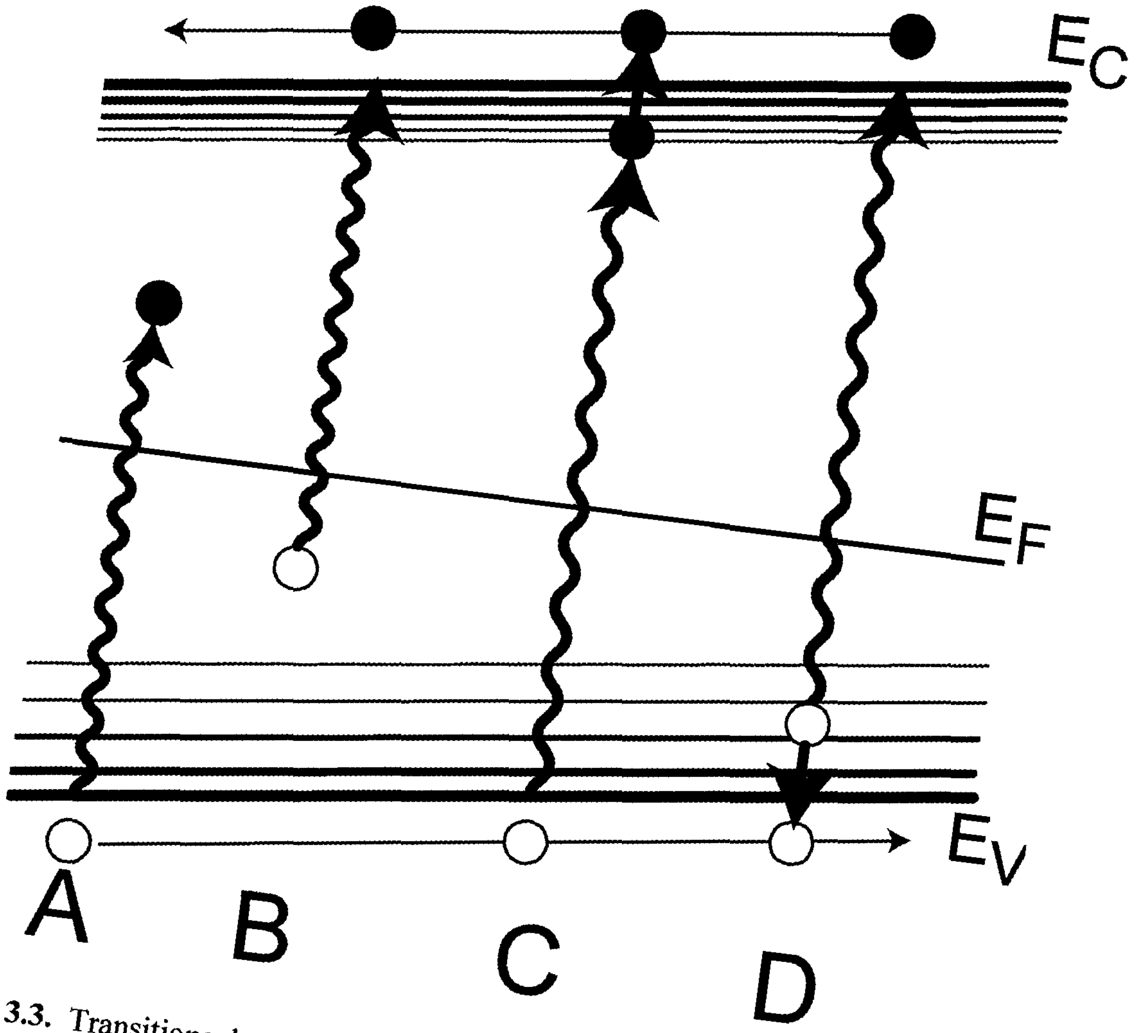

Figure 3.3. Transitions due to optical absorption in disordered semiconductors.

The emission energy is included in the limits to indicate the demarcation energy in the gap between filled states (states below the Fermi level that are occupied by electrons) and those that are able to thermally emit their charge on the time scale of the measurement. For a transient measurement with boxcars as indicated in figure 3.2 the time constant of the measurement is approximately [5]:

$$\tau = \frac{t_2 - t_1}{\ln(t_2) - \ln(t_1)}. \qquad (3.4)$$

Thus the time-dependent occupation of the defects due to thermal excitations is taken into account when considering transitions between states.

If we assume the optical matrix elements in equations (3.3) are constant and that the density of states in the bands are slowly varying relative to the features in the bandgap, the TPC/TPI spectra can be interpreted to be an integral over the density of gap states.

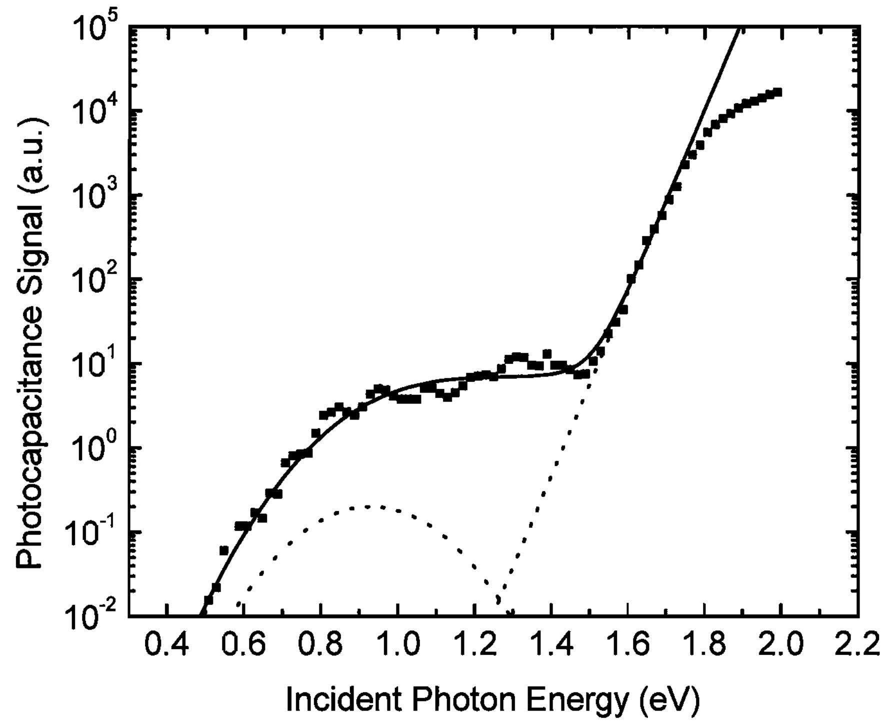

Figure 3.4. An example TPC spectrum taken on a hydrogenated nanocrystalline silicon solar cell device. Shown are the exponential Urbach tail and Gaussian defect band used to fit the spectrum.

There are several important features in the TPC spectrum. Fits to the density of states typically include an exponential Urbach tail (to be discussed in detail in section 3.3) and a Gaussian distribution of deep defects [3, 4, 6, 7]. Since the measured spectrum is the integral over the density of states in the bandgap, we actually fit the spectra with an error function and an exponential tail. It is possible to see more than one defect band although fits to CIGS and related devices have thus far only used a single defect band.

The measured capacitance signal is related to the *difference* in the number of optically excited charge carriers collected during the time window of the measurement, i.e.:

$$TPC \propto p - n \tag{3.4}$$

where p and n are the number of holes and electrons collected. Thus the sign of a TPC measurement tells us which carrier is being collected in larger numbers under the given measurement parameters. In addition, TPC is extremely sensitive to cancellation in devices where carriers are collected in similar quantities. This allow TPC to see features in its spectra that would be unobservable in additive spectra such as TPI.

The current signal in a TPI measurement is due simply to the *total* number of charge carriers collected during the time window of the measurement. Thus we can write

$$TPI \propto p + n. \tag{3.5}$$

The current signal is always enhanced with light, regardless of the transitions that are occurring.

In light of equations (3.4-5), by measuring TPC and TPI spectra, we can gain information about the relative collection fractions of the charge carriers in the device. Typically the spectra are aligned in the region below $E_{opt}=E_g/2$ where most of the signal should come from majority carriers, i.e. both TPC and TPI signals are proportional to the number of holes collected p. Then, the ratio of the signals in the bandtail region can be interpreted as the ratio R:

$$R = \frac{TPC}{TPI} = a\frac{p-n}{p+n} = a\frac{1-\frac{n}{p}}{1+\frac{n}{p}}. \tag{3.6}$$

The constant a is the ratio of TPC to TPI when only one carrier leaves the depletion region. For uniform absorption of light over the depletion region in a one-sided device, and assuming parabolic band bending, a can be shown to be

$$a = \frac{2\tau}{(V + V_{bi})}. \tag{3.7}$$

Due to the configuration of the solar cell devices, minority and majority charge are collected in different regions of the device. Optically excited electrons in the conduction band are swept *towards* the junction by the electric field in the device, whereas optically excited holes in the valence band are swept *away* from the junction towards the edge of the depletion region and the back contact. For this reason, TPC and TPI have different spatial sensitivities, which are important to keep track of when interpreting results [3, 5, 9].

Starting from the Poisson equation in equilibrium, we have

$$\psi_0(0) = \int_0^W \frac{xqN_A}{\varepsilon} dx.$$

If we emit $\delta p << qN_A$ holes at a location x within the depletion region, this collapses the depletion width by an amount δW, given by

$$\psi(0) = \int_0^{W+\delta W} \frac{xqN_A}{\varepsilon} dx = \int_x^{x+\delta x} \frac{x(\delta p)}{\varepsilon} dx.$$

The change in the potential at the junction is then

$$\delta\psi = \psi(0) - \psi_0(0) = \frac{q}{\varepsilon}(W(\delta W)N_A - x(\delta x)\delta p) = 0$$

which is experimentally constrained to be zero during the measurement. We can equate this to the capacitance using the standard parallel plate formula in equation (2.3) and we have

$$\frac{\delta C}{C} = -\frac{\delta W}{W} = -\frac{x(\delta x)(\delta p)}{N_A W^2} \propto x\,. \tag{3.8}$$

Thus the sensitivity of the capacitance response of holes emitted within the depletion region is proportional to the distance from the junction. A similar relation holds for electrons, with opposite sign.

To calculate the spatial sensitivity of the current measurement, we need to keep track of the total charge emitted, and where it goes. The total charge emitted is simply

$$\delta Q = Aq(\delta p)(\delta x)\,.$$

However, not all of this charge leaves the depletion region, as it is needed to produce the accompanying change in capacitance discussed above. The amount of charge required to change the depletion width by an amount δW is simply

$$\delta Q_+ = qAN_A\delta W\,.$$

Thus, the net charge collected outside the circuit as current is the difference between these two quantities:

$$\delta Q_{external} = \delta Q - \delta Q_+ = qA(\delta p)(\delta x)\left(1 - \frac{x}{W}\right).$$

Thus the current for majority carriers is most sensitive to changes near the junction, decreasing linearly towards the edge of the depletion region. For electrons, the net charge reaching the external induces an increase in the depletion width due to the reduced density of negative charge in the depletion region. This causes hole emission at the depletion edge, which creates a current with the same magnitude, with the sensitivity

$$\delta Q = qA(\delta n)(\delta x)\frac{x}{W}.$$

Thus the capacitance sensitivity increases linearly with distance from the junction for both carrier types, whereas the current sensitivity decreases linearly from the junction for majority carriers and increases linearly from the junction for minority carriers.

It is interesting to note that, by integrating the individual charge contributions to the capacitance and the current signals over the depletion width, one arrives at the previously stated relations

$$\begin{aligned}\delta C &\propto \delta p - \delta n \\ \delta Q &\propto \delta p + \delta n\end{aligned}.$$

3.3 The Urbach Tail

The Urbach tail is an exponential decrease in the optical absorption just below the band-edge that is almost universally observed in optical measurements. Urbach first observed it in silver bromide photographic emulsions in 1953 [10], followed shortly thereafter by Martienssen in alkali halide crystals. In addition to the exponential absorption edge, Urbach noticed that the inverse slope of the absorption edge decreased significantly with temperature. This important observation is related to the current interpretation of the Urbach tail as an effect of material disorder on electron states.

Because of their near universal observation in disordered materials, it is worthwhile to discuss the history and current understanding of Urbach tails and how they relate to the materials under study here. Urbach tails have been the focus of a great deal of theoretical and experimental research since their discovery. Multiple theoretical models as well as many empirical models have been developed in an attempt to explain a plethora of experimental data. One commonality amongst all the models and observations is the focus on deviations in the material from the ideal zero temperature crystal, i.e. disorder.

Generally, the Urbach absorption edge can be fit to the formula

$$\alpha(E_{opt}) = \alpha_0 \exp\left(\frac{E_{opt} - E_0}{E_U}\right), \tag{3.9}$$

where α_0 and E_0 are constants, and E_U is the Urbach energy, a parameter that has been observed to increase with increasing disorder by measuring the absorption edge after various systematic treatments or at different temperatures [11-13].

3.3.1 Types of Disorder

There are many types of disorder that are encountered in materials research. All of these are deviations from an ideal structure or configuration that cause some of the assumptions made in the description or analysis of such materials to break down. While the theoretical understanding of crystalline materials benefits from their long-range order, disordered materials confer no such simplification on the researcher. However, despite their difficult to describe properties and mechanisms, disordered materials have many applications.

Urbach tails have been observed in crystalline materials with both indirect [11, 12, 14] and direct [15] bandgaps. In these crystals the Urbach energies are on the order of 10meV, which is much smaller than Urbach energies typically observed in disordered materials. This is due to crystalline nature of these materials, which contain no structural disorder. The source of disorder in these materials is thermal or dynamic disorder. Because optical absorption happens on an extremely short time scale relative to the thermal motion of the electrons and lattice points of the crystal, one can take the approach that the optical absorption event “sees” the crystal in an effectively disordered state. While the time-averaged location of the atoms and electrons correspond to their ideal equilibrium locations, they are instantaneously out of place during the absorption event. Because the thermal fluctuations increase in amplitude with temperature, this type of *dynamic* disorder is a strong function of temperature. We can then rewrite equation 3.9 as

$$\alpha(E_{opt}) = \alpha_0 \exp\left(\frac{E_{opt} - E_0}{E_U(T)}\right)$$

where the Urbach energy parameter is now a function of temperature. It is generally agreed that the temperature dependence of the Urbach slope is reflects the thermal occupancy of phonon states in the crystal [16].

Materials which contain similar short range order to their crystalline counterparts but none of the long range order are referred to as amorphous materials. Despite their intrinsically disordered nature, these amorphous semiconducting materials have a broad range of applications, including solar cells and transistors.

The nature of the disorder in amorphous materials is due to the distribution of topological or structural configurations within the material. While the coordination number of most of the atoms may be the same as their crystalline counterparts, the bond angles and bond lengths are distributed about their ideal values. Even further, there may be significant deviations from crystalline topology such as the dangling and floating bonds found in amorphous silicon semiconductors, although these defects are thought to give rise to mid-gap states rather than Urbach tails [7]. Because these defects are frozen-in in these materials, they are temperature independent, and this type of disorder is sometimes referred to as *static* disorder.

In mixed materials that contain more than one type of atom, compositional disorder can arise due to imperfections in how the atoms are arranged relative to each other. Thus, while an ideal crystal lattice may be maintained, errors in the order of atom placement in the lattice can exist, giving rise to defects such as vacancies, substitutions, and interstitials. Several of these native defects are known to exist in CIGS materials in electronically and optically active configurations [17-19].

Cody et. al. developed a model to explain the effects of thermal and structural disorder in hydrogenated amorphous silicon materials [13]. Assuming the equivalence of thermal and structural disorder, they incorporated a temperature independent term related to the structural disorder into the dependence of the Urbach energy. The Urbach energy then took the form

$$E_U(T,X) = K\left(\left\langle U^2\right\rangle_T + \left\langle U^2\right\rangle_X\right)$$

where the first term in the parentheses is a factor related to the thermal average of the square displacement of atoms from their equilibrium positions, and the second term is mean-square contribution of the deviations of atomic positions from the ideal configuration, encompassing the structural disorder. Expressing the temperature dependent component with the temperature dependence of the phonon spectrum, and the structural component as a measure of disorder normalized to the zero-point uncertainty of the atomic positions, Cody et. al. determined the dependence of the Urbach slope on thermal and structural disorder to be

$$E_U(T,X) = \frac{\Theta}{\sigma_0}\left[\frac{1+X}{2} + \frac{1}{\exp(\Theta/T)-1}\right] \tag{3.10}$$

where Θ is the characteristic temperature of the phonon spectrum, and σ_0 is a parameter of order unity. This formulation allowed them to fit the Urbach slope of the absorption bandtail in their a-Si:H materials as the disorder was controlled using the temperature and evolution of the hydrogen content through thermal annealing.

The formulation of Cody et. al. was expanded for application to single crystal ternary $CuInSe_2$ materials, which suffer from compositional disorder due to deviations stoichiometry. Wasim et. al. generalized equation (3.10) to the form [20, 21]:

$$E_U(P,N,T) = \frac{k_b\Theta}{\sigma_0}\left[\frac{1+P}{2} + \frac{N}{\exp(\Theta/T)-1}\right]$$

where P and N are parameters used to describe deviations from molecularity (ideal cation to cation ratio) and valence stoichiometry (ideal anion to cation ratio). Using this model they were able to describe the temperature dependence of the Urbach energy in single crystals of $CuInSe_2$ and $CuInTe_2$.

Theoretical models used to derive the existence of the Urbach absorption edge typically consider the simple model of an electron that interacts with spatially random but static potentials [22-25]. These random potentials reflect the structural disorder in amorphous materials and disorder due to impurities in doped materials, and are able to reproduce the correct exponential dependence of the absorption edge for these materials.

Notes

[1] P. D. Paulson, R. W. Birkmire, and W. N. Shafarman, J. Appl. Phys. **94**, 879 (2003).

[2] A. Meeder, D. F. Marron, A. Rumberg, M. C. Lux-Steiner, V. Chu, and J. P. Conde, J. Appl. Phys. **92**, 3016 (2002).

[3] J. T. Heath, in *Department of Physics* (University of Oregon, Eugene, 2002), p. 148.

[4] J. T. Heath, J. D. Cohen, W. N. Shafarman, D. X. Liao, and A. A. Rockett, Appl. Phys. Lett. **80**, 4540 (2002).

[5] D. V. Lang, J. Appl. Phys. **45**, 3023 (1974).

[6] A. V. Gelatos, K. K. Mahavadi, and J. D. Cohen, Appl. Phys. Lett. **53**, 403 (1988).

[7] J. D. Cohen, T. Unold, and A. V. Gelatos, J. Non-Cryst. Solids **141**, 142 (1992).

[8] W. B. Jackson, S. M. Kelso, C. C. Tsai, J. W. Allen, and S.-J. Oh, Phys. Rev. B **31**, 5187 LP (1985).

[9] J. D. C. J. T. Heath, and W. N. Shafarman, Journal of Applied Physics **95**, 1000 (2004).

[10] F. Urbach, Phys. Rev. **92**, 1324 LP (1953).

[11] G. D. Cody, in *Materials Research Society Spring 2005*, San Francisco, CA, 2005), Vol. 862, p. A1:3.1.

[12] G. D. Cody, J. Non-Cryst. Solids **141**, 3 (1992).

[13] C. D. Cody, T. Tiedje, B. Abeles, B. Brooks, and Y. Goldstein, Phys. Rev. Lett. **47**, 1480 (1981).

[14] G. G. Macfarlane, T. P. McLean, J. E. Quarrington, and V. Roberts, Phys. Rev. **111**, 1245 (1958).

[15] M. Beaudoin, A. J. G. DeVries, S. R. Johnson, H. Laman, and T. Tiedje, Appl. Phys. Lett. **70**, 3540 (1997).

[16] H. Sumi and Y. Toyozawa, J. Phys. Soc. Japan **31**, 342 (1971).

[17] S. Lany and A. Zunger, J. Appl. Phys. **100**, 1 (2006).

[18] S. B. Zhang, S. Wei, A. Zunger, and H. Katayama-Yoshida, Phys. Rev. B **57**, 9642 (1997).

[19] S. Lany and A. Zunger, Phys. Rev. B **72**, 1 (2005).

[20] I. Bonalde, E. Medina, M. Rodriguez, S. M. Wasim, G. Marin, C. Rincon, A. Rincon, and C. Torres, Phys. Rev. B **69**, 1 (2004).

[21] S. M. Wasim, C. Rincon, G. Marin, P. Bocaranda, and E. Hernandez, Phys. Rev. B **64**, 1 (2001).

[22] C. H. Grein and S. John, Phys. Rev. B **39**, 1140 (1989).

[23] C. H. Grein and S. John, Phys. Rev. B **41**, 7641 (1990).

[24] S. John, M. Y. Chou, M. H. Cohen, and C. M. Soukoulis, Phys. Rev. B **37**, 6963 (1988).

[25] S. John, C. Soukoulis, M. H. Cohen, and E. N. Economou, Phys. Rev. Lett. **57**, 1777 (1986).

CHAPTER IV

CHARACTERIZATION OF THE EFFECTS OF SULFUR ALLOYING IN $Cu(In_xGa_{1-x})(Se_yS_{1-y})_2$ THIN FILM SOLAR CELL DEVICES

4.1 Effects of Sulfur Alloying

To date, the most efficient thin-film solar cell uses a CIGS absorber composition with a gallium content of approximately Ga/III≈0.3 [1]. This alloy composition produces a bandgap energy near 1.2eV, which is not ideally matched to the solar spectrum. However, wide gap solar cells based on higher gallium fraction CIGS absorbers failed to reach higher efficiencies, primarily due to rolloff of the open circuit voltage for bandgaps above 1.2eV [2]. Recent work using transient photocapacitance spectroscopy (TPC) determined the existence of an optically active defect located 0.8eV above the conduction band in CIGS regardless of gallium content [3]. Since gallium alloying increases the bandgap of CIGS primarily by moving the conduction band [4, 5], the 0.8eV defect moves towards the middle of the gap, and may become a detrimental recombination center.

Cation alloying (Cu, Ag; In, Ga, Al) is known to primarily have an effect on the conduction band minimum (CBM). On the other hand, anion alloying (Se, S, Te) affects both the valence band maximum (VMB) and CBM positions. In the case of sulfur alloying, the VBM moves towards lower energy reflecting the lower energy of the sulfur p-orbitals. In addition, the CBM moves towards higher energy due to the smaller volume of the compound and the nature of the sulfur s-orbitals [4-7]. Thus high bandgap quaternary alloys may be possible through alloying with sulfur instead of gallium or aluminum. Even more sophisticated alloys can be created using the pentenary system $Cu(InGa)(SeS)_2$.

We seek to understand the effects of sulfur alloying on the $CuInSe_2$ and $CuInGaSe_2$ semiconductor materials. We hope to be able to elucidate material properties that both help and hinder their use as absorbers in thin-film photovoltaic materials.

4.2 Cell Fabrication and Performance Characterization

All devices in this study were fabricated at the Institute of Energy Conversion at the University of Delaware. The 2 to 2.5 μm thick absorber layers were deposited on molybdenum coated soda-lime glass using elemental evaporation with no intentional grading of the bandgap [8]. The molybdenum back contact was 0.7 μm thick and was deposited by dc sputtering. A ~40nm thick CdS buffer layer was deposited on the absorber using a chemical bath deposition process. ZnO and ITO window layers were then deposited by rf sputtering. The undoped ZnO layer is typically 50 nm thick and has a resistivity of $\rho \approx 1\text{-}10\ \Omega\text{-cm}$. The doped ITO layer is 150 nm thick and has a resistivity $\rho = 3\times10^{-4}\ \Omega\text{-cm}$. Thus the baseline device structure is a glass/Mo/CIGSS/CdS/ZnO/ITO/NiAl-grid sandwich structure.

All films in this study have been deposited Cu-poor, except for an endpoint $CuInS_2$ film, which was Cu-rich. For this device only, the CuS layer was etched off prior to buffer and window layer deposition.

Device performance parameters as measured by IEC as well as the elemental compositions of the absorber layers are given in Table 4.1. Performance parameters were measured under an AM1.5 solar spectrum. Device areas are all equal to $A=0.47cm^2$. A graphical representation of the alloys under study is given in figure 4.1.

Table 4.1. Thin-film solar cell absorber compositions, bandgaps, and best cell performance parameters as grown and measured by IEC.

Sample	**Cu/III**	**Ga/III**	**S/VI**	**E_{gap} (eV)**	**Eff (%)**	**V_{oc} (V)**	**J_{sc} (mA/cm^2)**	**FF (%)**
$CuIn(Se_yS_{1-y})_2$ Device Series								
70008	~0.85	0	0	1.0	9.62	0.417	34.17	67.5
24160	0.91	0	0.33	1.2	9.4	0.4785	29.24	67.6
24208	0.88	0	0.54	1.3	7.27	0.5123	25.84	54.9
24147	>1	0	1	1.5	8.28	0.6509	21.23	59.9
Wide Bandgap $Cu(In_xGa_{1-x})(Se_yS_{1-y})_2$ Device Series								
33875	~0.85	0.80	0	1.5	9.6	0.7367	20.4	63.9
32989	~0.85	0.80	0	1.5	8.79	0.8193	16.44	65.3
24262	~0.85	0.68	0.12	1.5	9.2	0.809	16.4	69.2
24188	~0.85	0.51	0.33	1.5	10.8	0.826	18.6	70.0
24268	~0.85	0.33	0.56	1.5	4.4	0.694	10.2	62.0
$Cu(In_xGa_{1-x})(Se_{\sim0.75}S_{\sim0.25})_2$ Device Series								
24295	0.87	1	0.26	1.88	3.3	0.994	6.1	53.6
24438	0.91	0.62	0.24	1.55	9.6	0.865	17.1	63.1
24439	0.86	0.48	0.23	1.44	13	0.819	21.6	71.9
24440	0.78	0.38	0.23	1.37	14.6	0.776	24.3	76.7
24442	0.80	0.29	0.24	1.32	15	0.73	24.9	79.3

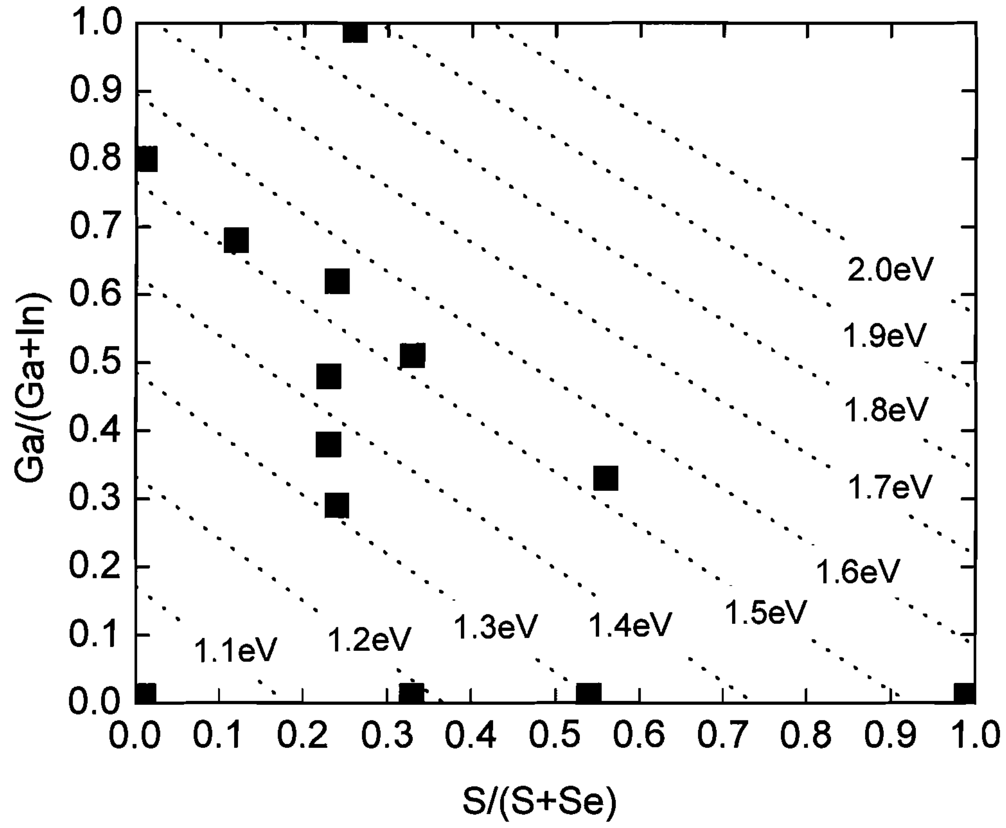

Figure 4.1. Absorber alloys investigated as a function of Ga and S fraction. Constant bandgap lines for the pentenary alloy system CIGSSe are given for reference [9].

4.3 Characterization of CuIn(Se_yS_{1-y})$_2$ Thin Film Solar Cell Devices

4.3.1 Electrical Characterization of CuIn(Se_yS_{1-y})$_2$ Thin Film Solar Cell Devices

Our first investigation involved a characterization of a series of four CuIn(Se_yS_{1-y})$_2$ solar cell devices. The devices characterized are shown in Table 4.1, and include two ternary endpoint devices. The device labeled 70008 is a $CuInSe_2$ endpoint device, and was characterized previously [10], and data from that study is included here for completeness. In that work this device is referred to as "D008", and results will be cited from there where appropriate. Additionally, there are two endpoint $CuInS_2$ devices of identical composition. Electrical measurements were performed on device 24147 and optical measurements were performed on the second device (D138). Results between the two devices were similar where the measurements overlapped.

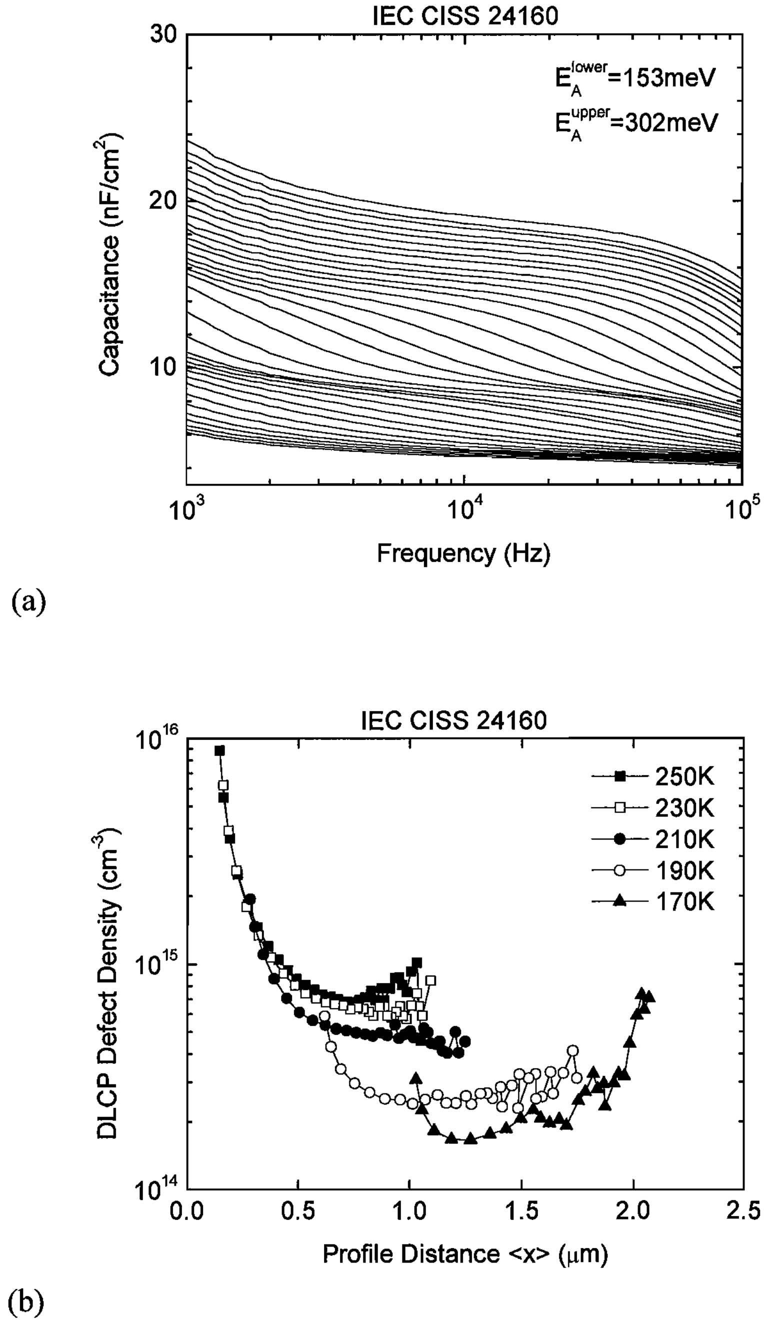

Figure 4.2. C-f-T and DLC profiles for CISS device 24160. **(a)** Admittance spectrum for CISS device 24160 with CISSe composition with S/VI=0.33, measured at 0V applied bias from 110K to 300K in 5K steps. **(b)** DLC profiles at 10kHz over the bias range {-1.0V to +0.5V, ΔV= 0.05V}.

Devices were initially characterized using admittance spectroscopy, measuring the capacitance and conductance as a function of frequency and temperature. These data provide broad information about the electronic properties of the device in the dark, including defect activation energies, the depletion width, and on occasion the geometric width.

As shown in figure 4.2a, the CISS device with S/VI=0.33 showed two activated steps the capacitance occurring over several decades of frequency. The measured activation energies are 153meV and 302meV for the lower and upper steps respectively. It is noted that the upper activation energy is approximately twice the lower activation energy. This as yet unexplained correlation has been seen in several devices in this study. The thermal emission prefactor was determined by the exponential of the y-intercept of the Arrhenius plot as described in chapter II, and was found to be $\nu=10^{11}$ sec^{-1} for the upper step and $\nu=10^{9}$ sec^{-1} for the lower step. These values are somewhat low, typical prefactors are around 10^{12} sec^{-1}. However, in thermally activated processes the prefactor and the activation energy may be related by the Meyer-Neldel rule, which may explain the small prefactor [10].

At the lowest temperatures the capacitance curves all come together at a nearly constant value near 4.1nF/cm^2. By inverting equation (2.17) we compute a geometric width for this device of 2.59μm, in good agreement with the reported thickness from IEC and the typical geometry of these devices. This is confirmed in figure 4.2b, where the DLC profiles have a similar range.

The DLC profiles shown in figure 4.2b show relatively flat defect profiles over the range of reverse biases, with the profiles rising sharply in the forward biases. The average density in the flat regime of the 170K profile is taken to be the free hole carrier density *p* of the device, as this is profile is taken at the smallest emission energy. Thus $p=2x10^{14}$ cm^{-3}. The difference between this value and the limiting value in the flat regime seen at high temperatures gives the defect density, $N_d=5x10^{14}$ cm^{-3}. These numbers are somewhat smaller than typically seen in CIGS devices without sulfur. This may be caused by decreased doping levels due to activation energies for acceptor levels shifting to higher energies as selenium is replaced by sulfur [7, 11].

thus diminishing their access to the valence band [7, 12].

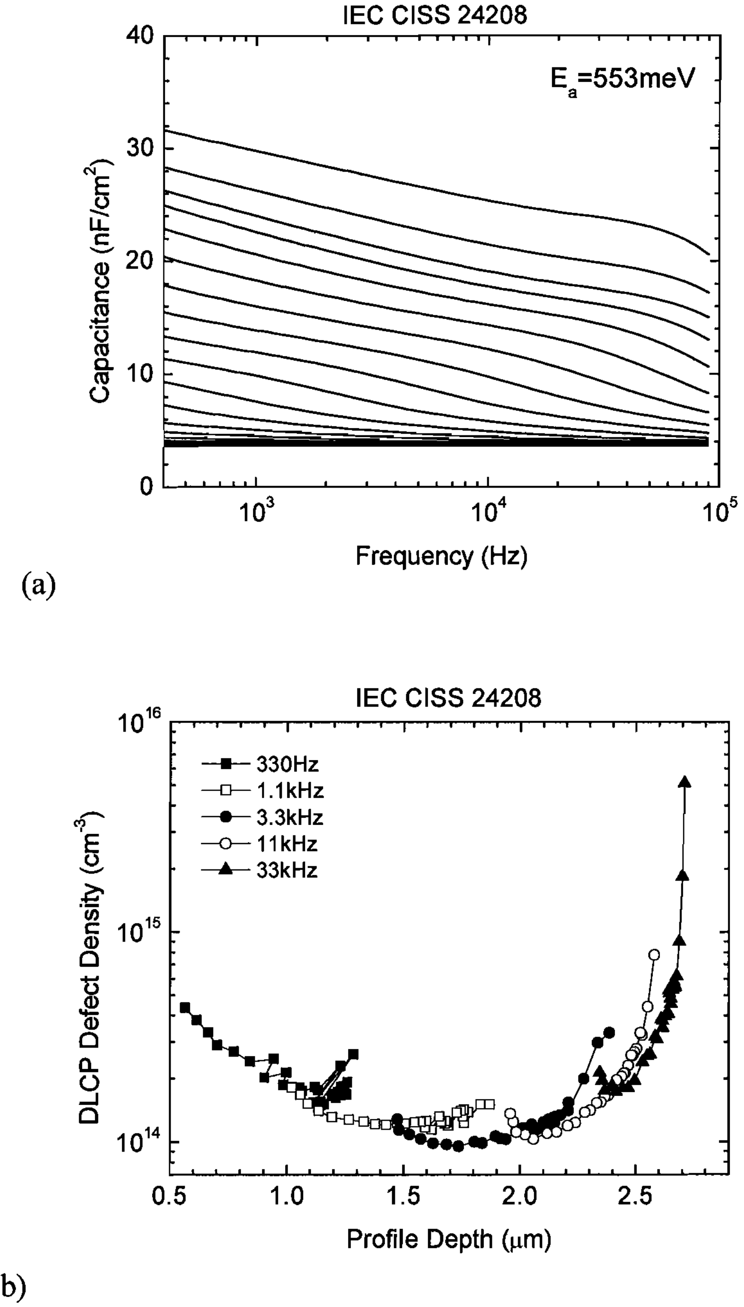

Figure 4.3. C-f-T and DLC profiles for CISS device 24208. **(a)** Capacitance spectra for IEC CISS 24208 (S/VI=0.54) in 10K steps over a range from 100K to 330K. **(b)** DLC profiles for IEC CISS 24208 at 240K over a range of frequencies. The dc voltage ranged from -1.3V to +0.3V in 0.05V steps.

Figure 4.3a shows C-f-T data taken for the quaternary device with nearly equal ratios of sulfur and selenium. The lower limit of capacitance gives a geometric width equal to 2.6μm, again, in good agreement with known device structures, as well as in agreement with the maximum profile depth of the DLC profile shown in figure 4.3b.

There are no steps with increasing emission energy that are immediately apparent to the eye in figure 4.3a. However, a plot of –f(dC/df) readily indicates a peak which allows us to deduce an activation energy of 553meV and a thermal emission prefactor of 10^{15} sec^{-1} for some type of defect response in this device.

The DLC profile for this device indicates a large U-shaped defect distribution across the entire area of the device. The sharp rise of the DLCP density towards the back of the film reflects the inability of the capacitance to change at that depth due to the geometric thickness of the film that is almost entirely depleted under these measurement conditions. As the measurement frequency is lowered, defect states within the film are able to respond, giving a free carrier density near 10^{14} cm^{-3}.

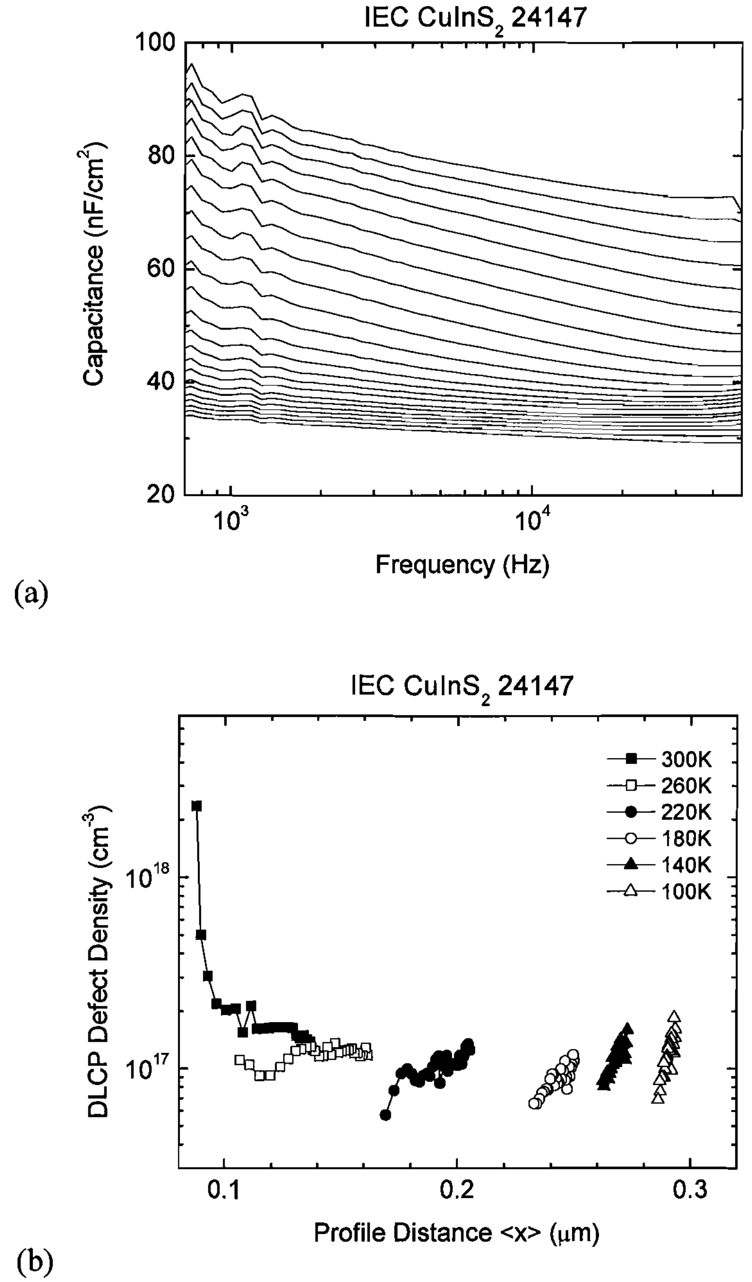

Figure 4.4. C-f-T and DLC profiles for CIS endpoint device 24147. **(a)** C-f-T data taken on endpoint $CuInS_2$ device from 80K to 300K in 10K steps. **(b)** DLC profiles taken at 10kHz over at voltages ranging from -0.7V to +0.6V in steps of $\Delta V=0.05V$.

Figure 4.4 shows C-f-T spectra and DLC profiles for the endpoint $CuInS_2$ solar cell device. This device was grown with a Cu-rich stoichiometry, which is different than typical CIGS solar cell devices. Cu-rich growth promotes S diffusion through the absorber during the deposition process [13, 14].

The C-f-T spectra look very similar to those collected for sample 24208 shown in figure 4.2a, i.e. no clear step in the capacitance with changing emission energy. Indeed, -f(dC/df) analysis uncovers no peaks, thus we can see no activated feature in these C-f-T spectra. The increasing but somewhat constant capacitance with temperature has been attributed by Kneisel *et. al.* to a constant density of gap states [15]. Our data look surprisingly similar to theirs over the temperature and frequency range measured. In their interpretation the lower limit of capacitance in figure 4.4a is associated with the depletion width, which for this device is W_d=0.34μm. DLC profiles for this device show a nearly constant response near $N_d=10^{17}$ cm^{-3} over a very small range of response depths.

Device parameters deduced from electrical measurements are summarized in Table 4.2 below.

Table 4.2. Device parameters as measured with electrical characterization techniques for CISSe devices.

Sample	S/VI	p ($10^{15}cm^{-3}$)	N_d ($10^{15}cm^{-3}$)	E_{A1} (meV)	ν (10^x sec^{-1})	W_d (μm)	W_{geo} (μm)
70008 [10]	0	0.7-3	6-20	284,314	--	--	--
24160	0.33	0.2	0.5	153 302	9 11	0.72	2.59
24208	0.54	0.1	--	553	15	--	2.6
24147	1	--	100	--	--	0.34	--

4.3.2 Optical Characterization of $CuIn(Se_yS_{1-y})_2$ Thin Film Solar Cell Devices

$CuIn(Se_yS_{1-y})_2$ devices were characterized using transient photocapacitance (TPC) and transient photocurrent (TPI) spectroscopies. These measurements revealed the bandgap of the CISSe absorber layers in the device as a function of alloying, the Urbach energies of the devices, as well as their defect structure. Very interesting results were obtained for the endpoint $CuInS_2$ device, which will be discussed in detail.

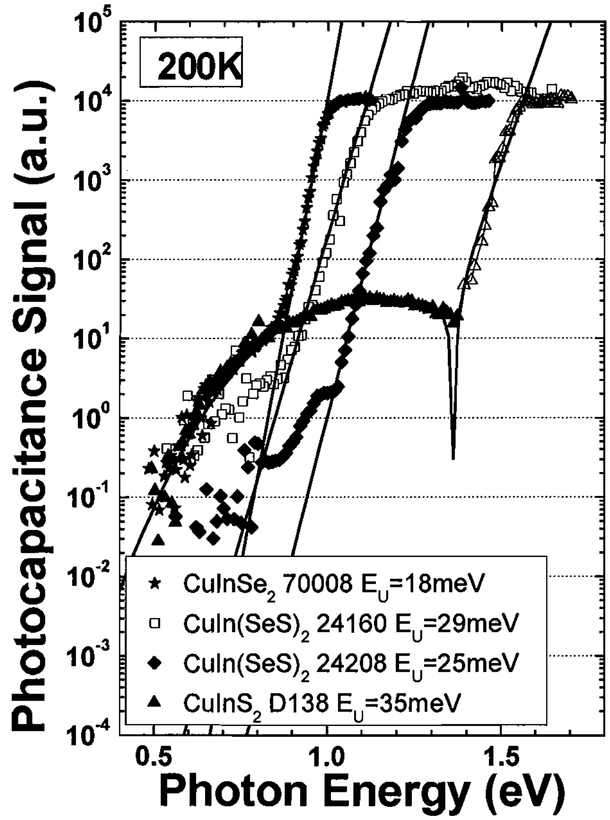

Figure 4.5. TPC spectra for the four CISSe devices taken at 200K. Open symbols for sample D138 denote a *negative* TPC signal.

Shown in figure 4.5 are TPC spectra taken at 200K for the four CISSe devices in this study. The change in optical bandgap with sulfur alloying can be seen clearly by the continuous shifting onset of exponential bandtailing with sulfur addition. In addition, sub-bandgap defect signals can be seen for all four alloys. These defect signals are typically fit using an error function, which is an integral of a Gaussian energy distribution of defects. Urbach energies are determined by using an exponential to fit the bandtail that extends into the sub-bandgap region.

Urbach energies are listed on the graph in figure 4.5. A very small Urbach energy of 18meV is given for the endpoint $CuInSe_2$ device that was characterized in a different study [3] and is included here for completeness. Urbach energies increase once sulfur is added to the system, jumping to 29meV for the absorber with S/VI=0.33, and 25meV for the device with S/VI=0.54. The Urbach energy for the endpoint $CuInS_2$ device was fit with an Urbach energy of 35meV. Note that the TPC signal collected in the bandtail region was *negative* for the endpoint $CuInS_2$ device. This may affect our ability to measure the bandtail width due to cancellation between the negative bandtail signal and the positive defect signal. A good fit to the bandtail region requires a simultaneous fit to the defect region so the area where the two signals cancel can be properly accounted for.

Deep defect distributions have been fit with error functions, which give the energetic center and width of the Gaussian deep defect distribution. Previous results on CIGS alloys showed the existence of a defect centered 0.8eV above the conduction band, independent of the gallium content [3]. However, gallium alloying only changes the energetic position of the valence band 40meV over the entire range of alloys from $CuInSe_2$ to $CuGaSe_2$ (1.0eV to 1.7eV) [4]. On the other hand, sulfur changes the energetic positions of both the valence and conduction band. Thus we may expect to see shifting defect energies as the sulfur content of the absorber is changed and the energetic difference between the valence band and the defect changes. This assumes that the defect does not also change energy with sulfur alloying.

Fits to the defect bands of the TPC spectra in figure 4.5 do, in fact, require shifting defect energies with sulfur addition. While the $CuInSe_2$ endpoint device has the well established defect at E_D=0.8eV, the defect energies used for fitting the two quaternary alloys were E_D=0.89eV and E_D=0.92eV for devices 24160 and 24208 respectively. These shifts in defect energy are in good agreement with the expected shift of the valence band with sulfur alloying [4, 7].

The endpoint $CuInS_2$ device was fit with a defect energy of E_D=0.9eV, which does not fit the alloying trend. This may be due to the Cu-rich nature of this device, which differentiates its stoichiometry from the other devices in this study. Optical fitting parameters in this study are summarized in Table 4.3.

Table 4.3. Optical fitting parameters used to fit TPC spectra for the four CISSe devices. Expected valence band offsets were computed from [4].

Sample	**E_{Urbach} (meV)**	**E_D (eV)**	**$2\sigma_D$ (meV)**	**Expected ΔE_V (meV)**
70008	18	0.8	150	0
24160	29	0.89	260	-9.2
24208	25	0.92	160	-15
D138	35	0.9	220	-28

In device D138 we noticed a marked temperature dependence in the width of the defect band. As the temperature of the measurement was decreased, the measured width of the defect band increased significantly. These data are shown below in figure 4.6. The broadening of the defect band as the measurement temperature is lowered can be seen in the region below ~1.2eV. We believe that this reflects the variation of the thermal emission rate of trapped holes from this broad defect band as a function of temperature, as per the integration limits in equation (3.3). Thus, while the filling pulse ensures that the majority of gap sates are occupied with holes initially, the TPC

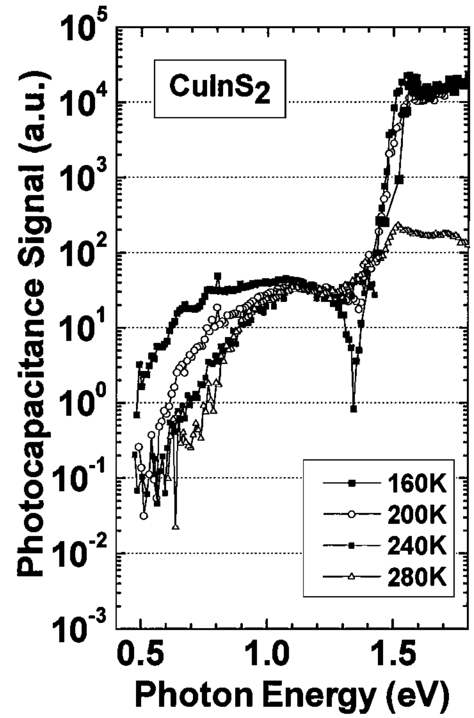

Figure 4.6. TPC spectra for the endpoint CuInS$_2$ device at various temperatures. Distinct dependence in the width of the defect band on temperature is observed.

measurement records the optical excitation of holes out of these states during a time window beginning roughly 250ms later. Because of this delay τ, holes will have been thermally emitted to the valence band up to an energy $E_e=k_BT\log(\nu\tau)$ above the valence band E_V, hence the TPC signal from these states will be absent. As the temperature increases, so will E_e, increasing the low energy threshold for optical excitation. Ultimately, at high enough temperature, the TPC spectrum will only reveal the deep defect states that never lose their holes to the valence band via thermal emission. These are the states that lie above the quasi-Fermi level within the deep depletion region in steady-state.

It is important to note that the defect band revealed in the TPC spectra for a series of Cu(In_xGa_{1-x})Se_2 devices exhibited no such temperature dependence in the defect band [3, 10].

Finally, in figure 4.7, we show matched TPC and TPI spectra for the endpoint $CuInS_2$ device at 280K. At this temperature the TPC signal is positive over the entire range of optical energies. Because the current from escaping holes and electrons has the same sign, the TPI signal is always positive.

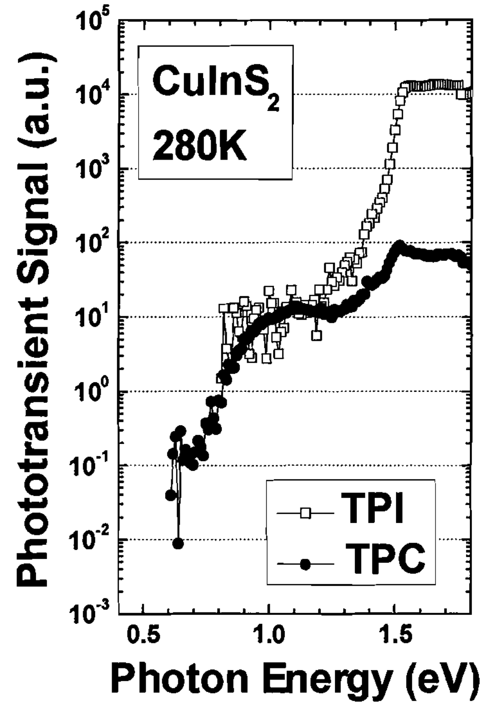

Figure 4.7. TPC and TPI spectra for the endpoint $CuInS_2$ device at 280K.

By aligning the two spectra in the region of the defect band, we can estimate from the relative magnitudes of the bandtail signals that the TPC signal is cancelled to within one part in 250 at 280K. The TPI signal in the bandtail region is roughly the same size as the negative bandtail signal seen in TPC at the lower temperatures. This implies that the minority current largely dominates the excitation of photogenerated electron-hole pairs in the lower temperature regime.

4.4 Characterization of $Cu(In_xGa_{1-x})(Se_yS_{1-y})_2$ Wide-Bandgap Thin Film Solar Cell Devices

Wide-bandgap thin-film solar cells are useful for a variety of reasons. The optimum single-junction device bandgap for matching the solar spectrum lies near 1.4eV [16], whereas record efficiency CIGS based thin-film solar cells have bandgaps near 1.2eV [1].

An advanced technique used to match the absorption of a solar cell device to the solar spectrum is the use of multi-junction devices [17]. These multijunction devices consist of solar cells stacked on top of each other to more efficiently absorb energy from the solar spectrum. The largest bandgap cells are on the top of the device and absorb the high energy photons from the solar spectrum. They transmit the photons with energies below their bandgaps, which are then absorbed by a solar cell with a smaller bandgap situated beneath the wider gap cell. As the number of cells in such a multijunction device increases, so does the theoretical maximum efficiency (and the cost) of the device [17-19]. For an infinite number of junctions, the maximum theoretical conversion efficiency of unconcentrated light is 68% [19].

Wide bandgap thin-film absorbers made with $CuInGaSe_2$ and $CuInAlSe_2$ have failed to meet performance expectations, primarily due to rolloff of the open-circuit voltage at bandgaps above 1.3 eV [2]. Photocapacitance studies indicated the existence of a defect band that moved to the center of the bandgap as the gap was widened with gallium alloying in CIGS devices [3]. Poor material electronic quality, including large bandtails and spatial nonuniformities, was found in the CIAS alloy system [20].

In this section we explore the pentenary alloy system $Cu(In_xGa_{1-x})(Se_yS_{1-y})_2$ (CIGSS) to find out whether more sophisticated alloying could result in an electronic structure that reduces the rate of recombination through the dominant deep defects. To help isolate the other factors that might affects the device performance, we first examine sample devices with different alloy fractions of Ga/III and S/VI, but coordinated in such a way as to maintain a bandgap of 1.5 eV.

All of our devices were fabricated at the IEC at the University of Delaware. The deposition procedure and performance parameters are describe in section 4.2. This study includes two CIGS devices with Ga/III=0.8. Device 32989 is from a previous study on Ga alloying in CIGS [3, 10], and device 33875 is a new device grown for this study. Results for the two devices were similar, so I will restrict most discussion of the two devices to results on device 33875.

4.4.1 Electrical Characterization of $Cu(In_xGa_{1-x})(Se_yS_{1-y})_2$ Wide-Bandgap Thin Film Solar Cell Devices

Shown in figure 4.8 is the C-f-T characterization of the Ga/III=0.8 CIGS device 33875. A thermally activated process is clearly visible as the successive steps in capacitance with increasing temperature. This step has an activation energy of 182meV and is related to the activation of the response of the deep defect. This is verified through examination of the DLC and CV profiles shown in figure 4.9. As can be seen in the DLC profile, under reverse bias the profiles are spatially uniform with a free carrier density of $2\text{-}3\times10^{15}$ cm^{-3}, and show no activated increase as the temperature of the measurement increases. However, the CV profiles show a clear activation of a defect response with increasing measurement temperature, up to a maximum of 6-7 x10^{15} cm^{-3}. The deep defect density can be estimated by the difference between the CV and DLCP densities at high and low emission energies respectively.

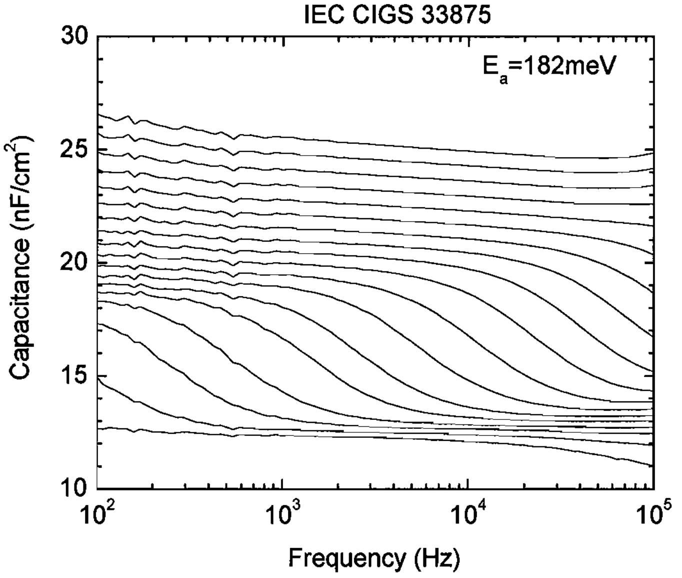

Figure 4.8. C-f-T data for 80% Ga CIGS device 33875. Data were taken over a temperature range of {100K to 260K in 10K steps}.

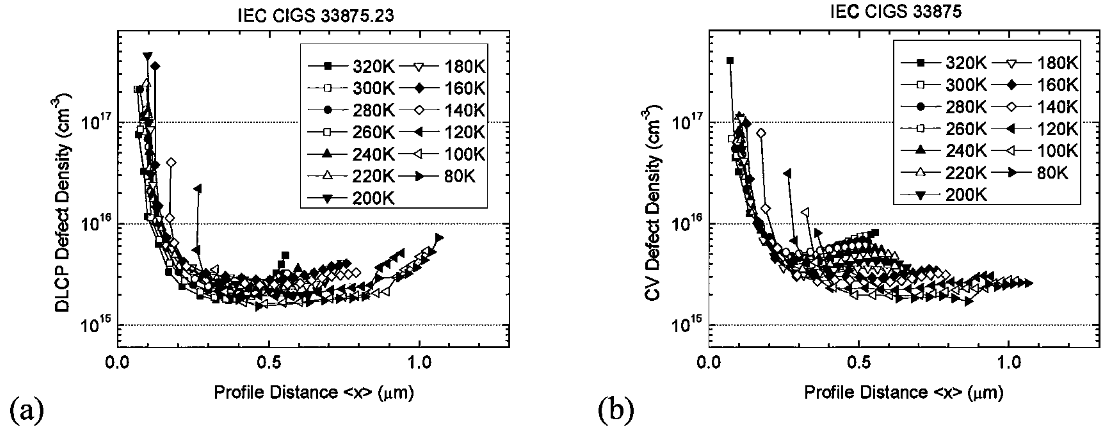

Figure 4.9. **(a)** DLC profiles for the 80% Ga device at 10kHz over the voltage range {-1.2V to +0.6V, ΔV=0.1V}. **(b)** CV profiles taken simultaneously under the same measurement conditions.

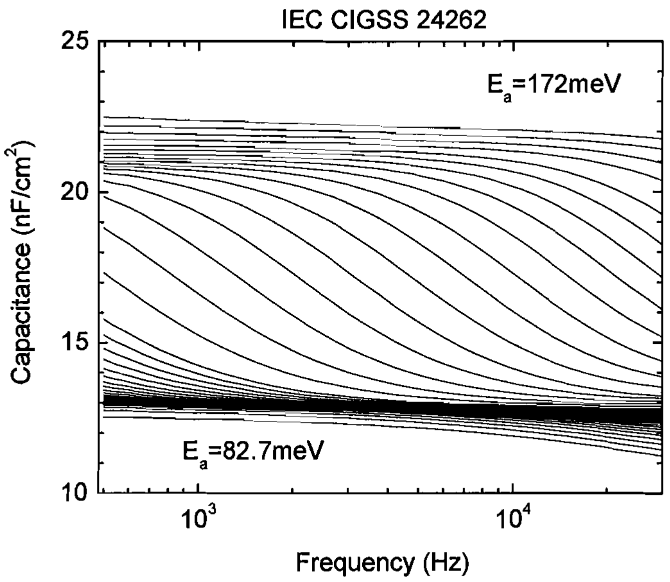

Figure 4.10. C-f-T spectra for CIGSSe device 24262 (Ga/III=0.68, S/VI=0.12) from 80K to 130K in 2K steps and 130K to 215K in 5K steps..

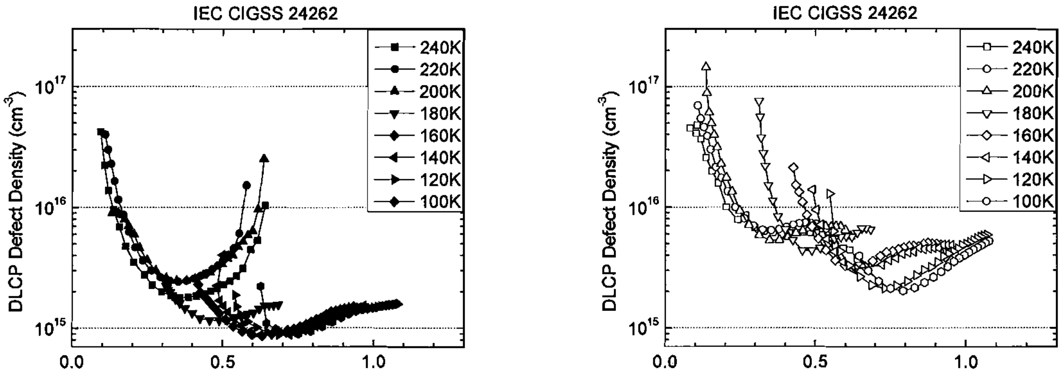

(a) (b)

Figure 4.11 **(a)** DLC profiles at 10kHz for CIGSS 24262 (Ga/III=0.68, S/VI=0.12) over a voltage range {-2V to +0.9V, ΔV=0.1V} **(b)** Simultaneously collected CV profiles.

In figure 4.10 the C-f-T spectra are shown for CIGSSe device 24262, with Ga/III=0.68 and S/VI=0.12. The activation energy for the large prominent step is equal to 172meV. The activation energy of the lower step, which is only hinted at in the high Frequency, low temperature regime, was 82.7meV. The depletion width, calculated near the capacitance value of 13nF/cm^2 was 0.79μm.

DLC and CV profiles for this device are shown in figure 4.11. Defect activations with increasing measurement temperature are clearly seen. A free carrier density of $9x10^{14}$ cm^{-3} is measured from the low emission energy DLC profiles, and an activated defect density of $4x10^{15}$ cm^{-3} is measured from the high temperature CV profiles. In the reverse bias regions of the graphs the profiles show relatively uniform profiles, in-line with previous results on materials grown using this technique [21].

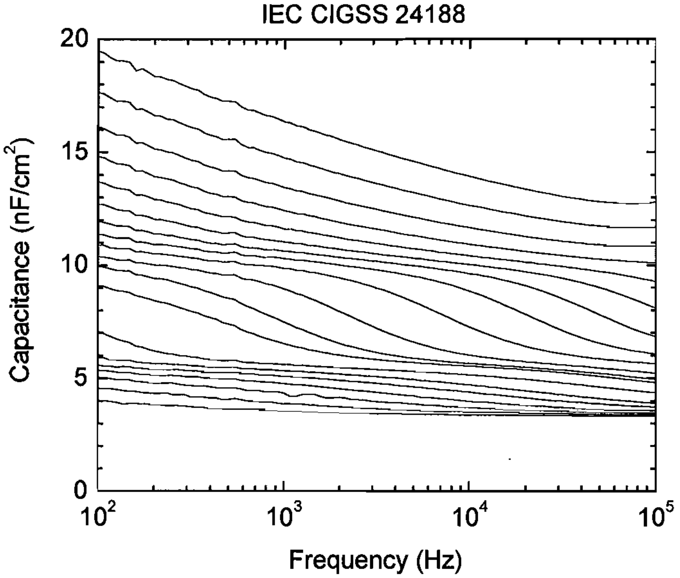

Figure 4.12. C-f-T spectra for CIGSSe device 24188 (Ga/III=0.51, S/VI=0.33) over a temperature range 90K to 270K, ΔT=10K.

Figure 4.12 shows C-f-T spectra for the midpoint pentenary device 24188. Two activated steps can be seen, one just below 5 nF/cm^2 and one at 7.5 nF/cm^2. The activation energies of these steps are 157meV and 291meV respectively. The capacitance minimum at low temperature and high frequency gives a geometric width of W_{geo}=2.83μm. This is in moderately good agreement with device dimensions, but is a bit large, and may indicate errors in the sample area.

Figure 4.13 shows DLC and CV profiles for device 24188. DLCP and CV densities are similar, both showing activation of a deep defect. The free carrier density is near 4 x10^{14} cm^{-3} and the deep defect density is near 3 x10^{14} cm^{-3}. Again, these numbers are smaller than those seen in standard CIGS devices, and are likely reflecting the increased energetic depth of the shallow acceptor and deep defect levels as the valence band is moved away with sulfur alloying.

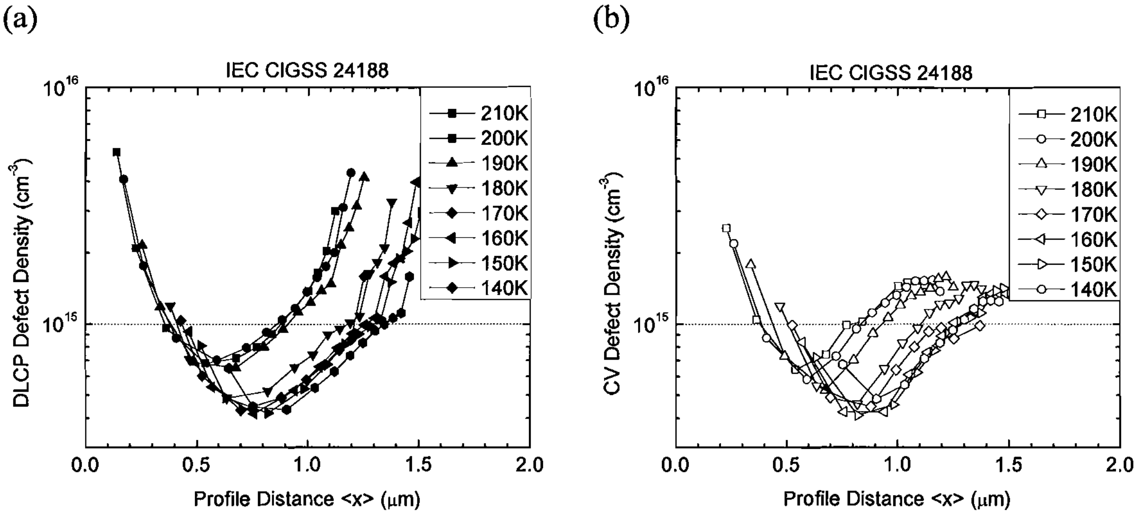

Figure 4.13. DLC and CV profiles for CIGSSe device 24188. **(a)** DLC profiles at 10kHz for CIGSS device 24188 (Ga/III=0.51, S/VI=0.33) over a voltage range {-1.0 to +0.4V, ΔV=0.1V} **(b)** Simultaneously collected CV profiles.

Data for device 24268 (Ga/III=0.33, S/VI=0.56) are quite different. C-f-T spectra shown in figure 4.14a show no activated step at all, with all of the capacitance curves coming to a constant geometric value at high frequencies. There is a hint of a step at low frequencies and high temperatures. If one adopts an Arrhenius approach, the activation energy of this "step" is 753meV with a thermal emission prefactor of 10^{16} sec^{-1}.

However, it must be noted that no peaks in the conductance nor in a –f(dC/df) plot were seen, so this analysis is dubious.

The DLC profiles show a large U-shaped profile when taken together as a whole. The minimum density is near 6×10^{13} cm^{-3}, indicating that this device is nearly intrinsic. The sharp rise in DLC densities near the back of the sample (large profile distance) is an artifact of the inability of the capacitance to change with δV since the response depth $\langle x \rangle$ is pinned at the geometric edge of the film. This is interpreted by the DLCP calculations as a large defect density, but we do not believe the defect density rises at the back of the film.

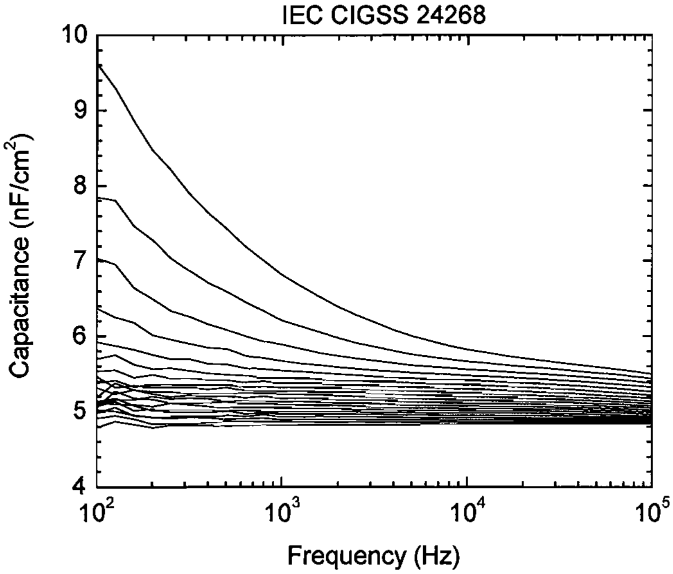

(a)

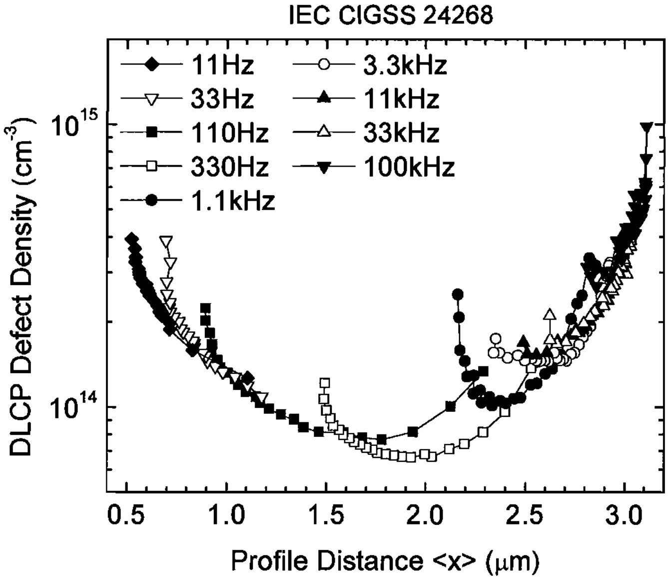

(b)

Figure 4.14 C-f-T and DLC profiles for CIGSSe device 24268. (**a**) C-f-T spectra taken on device 24268 (Ga/III=0.33, S/VI=0.56) from 110K to 300K in 10K steps. (**b**) DLC profiles for the same sample taken at 330K for voltages from -1V to +0.45V in 0.05V steps.

A summary of the electronic parameters measured on these devices is given in Table 4.4. One clear trend that can be seen is the increase in activation energies with sulfur alloying, reflecting the movement of the majority band away from the shallow and deep acceptor levels. This is corroborated by an inverse correlation of sulfur content to the free carrier density.

Table 4.4. Electrical characterization parameters for wide-bandgap CIGSSe.

Sample	Ga/III	S/VI	p (10^{15} cm^{-3})	N_d (10^{15} cm^{-3})	E_A (meV)	ν (10^x sec^{-1})	W_d (μm)	W_{geo} (μm)
33875	0.8	0	2.5	2.5	182	9	0.79	--
32989	0.8	0	0.6	2	--	--	--	--
24262	0.68	0.12	0.9	6	172 82.7	9 10	0.79	--
24188	0.51	0.33	0.4	0.3	291 157	12 10	--	2.83
24268	0.33	0.56	0.06	--	753	16	--	3.1

4.4.2 Optical Characterization of Cu(In_xGa_{1-x})(Se_yS_{1-y})$_2$ Wide-Bandgap Thin Film Solar Cell Devices

CIGSS pentenary devices were extensively characterized using TPC and TPI measurements over a variety of temperatures. Initial results showed the typical features expected in a TPC/TPI spectrum, namely exponential bandtails and Gaussian defect bands. Representative spectra from the TPC measurements on the CIGSS alloy devices are shown in figure 4.15. Fitting parameters are shown in Table 4.5.

All of the devices in this study showed somewhat larger Urbach energies, from 25meV to as high as 32meV, compared to typical Urbach energies in quaternary CIGS devices near 20meV. These broader bandtails indicate a higher degree of structural and/or

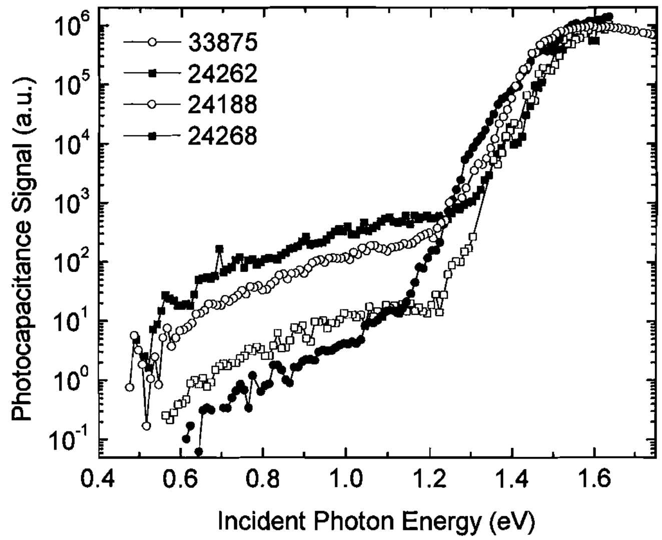

Figure 4.15. TPC spectra collected near 180K for each of the wide-bandgap pentenary devices. Spectra have been aligned in the region above the bandtail.

Table 4.5. Fitting parameters to TPC spectra for wide bandgap CIGSSe devices assuming an exponential bandtail and a Gaussian distribution of deep defects.

Sample	Ga/III	S/VI	E_U (meV)	E_D (eV)	2σ (eV)
33875	0.8	0	29	.9	.24
24262	0.68	0.12	32	1	.32
24188	0.51	0.33	25	1.05	.3
24268	0.33	0.56	26	1.16	.32

compositional disorder in the pentenary devices. A comparison between TPC and TPI magnitudes indicated that the devices with broader bandtails had poorer minority carrier collection. Device 24188 has the smallest Urbach energy at 25meV, and it also has the highest efficiency, as given in Table 4.1.

The TPC spectra also clearly indicate the existence of a broad defect band in all cases (the region for optical energies below the bandtail region). By fitting this portion of the spectrum with a Gaussian distribution, we conclude that the energy position of the defects shifts systematically higher toward the conduction band as the sulfur fraction is increased. (The energies deduced from the Gaussian fits are also listed in Table 4.5.) We believe that this reflects how, when the gap is kept constant, the combination of increasing the sulfur fraction while decreasing the gallium fraction affects the band edges. In such cases the two band edges would be expected to move in parallel toward lower energies. Based upon the deduced energy shift of the defect band, this would indicate that its energy is not pinned to either the conduction band or the valence band, but to some other constant energy feature in the electronic structure of the CIGSS alloy system. In addition, we note that the widths of the defect bands used to the fit the TPC spectra were roughly a factor of two broader than those of similar defect features appearing in the TPC spectra of quaternary and ternary sample devices studied previously.

Another feature seen in these devices that was not observed in CIGS devices is a strong temperature dependence. As shown in figure 4.16, there is a significant increase in the signal from the optical defect at lower temperatures. We can account for this variation in temperature by considering how the electronic occupation of the defect

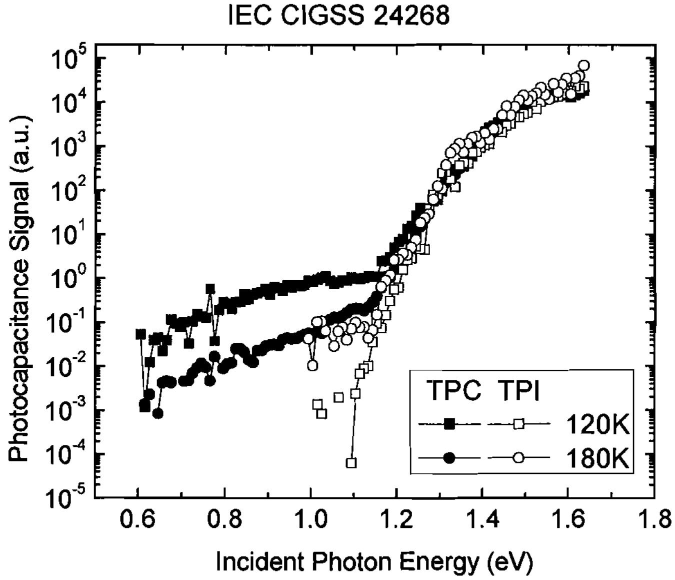

Figure 4.16. TPC and TPI spectra on device 24268 (Ga/III=0.33, S/VI=0.56) at high and low temperatures showing temperature dependence in the defect band region.

depends on the optical filling rate in competition with a thermal emptying rate.

To study this effect in detail, we measured the TPC signal of the devices in two photon energy regimes: With monochromatic light from the monochromator at 1.45eV, which is just below the bandgap of these devices to ensure penetration of the light into the devices, and again with sub-bandgap light from a white-light source filtered by a germanium long-pass window, giving light with energies smaller than about 0.73eV. Using these wavelengths we are able to isolate the "above gap" signal and the defect signal. The ratio of these two signals, dubbed the "relative defect signal", provides a measurement of the relative occupation of the deep defect, which exhibits a sharp increase in the form of a step, as shown in figure 4.17.

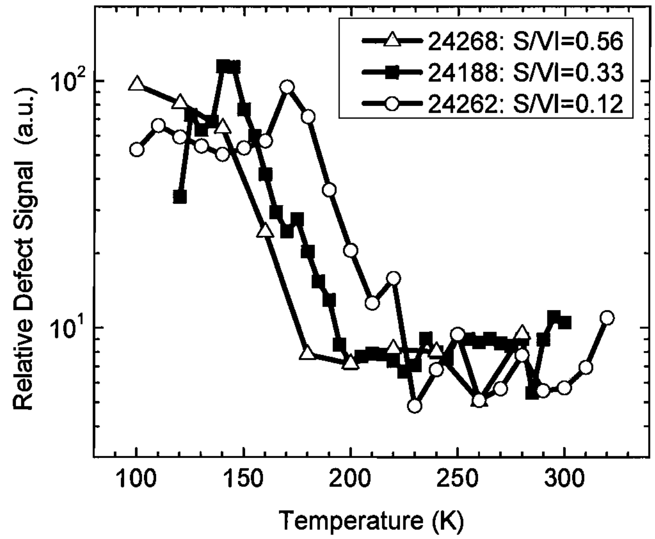

Figure 4.17. Relative defect signal for the three sulfur containing CIGSS devices.

The relative defect signal (RDS) shows a steep increase in magnitude in a step-like fashion as the temperature of the measurement is decreased. This step decreases in temperature systematically with increasing sulfur content, and occurs roughly at the temperature where the (nearly temperature independent) optical rate filling the defect with electrons from the valence band equals the thermal rate for emptying the defect into the conduction band; that is, when

$$\beta\Phi \approx \upsilon \exp\left(-\frac{E_C - E_D}{k_B T}\right),$$

where β is the optical cross section for transitions into the defect, Φ is the photon flux, ν is the prefactor for thermal emission into the conduction band, and E_D is the energy of the defect into the gap. This filling and emptying configuration is represented schematically in figure 4.18.

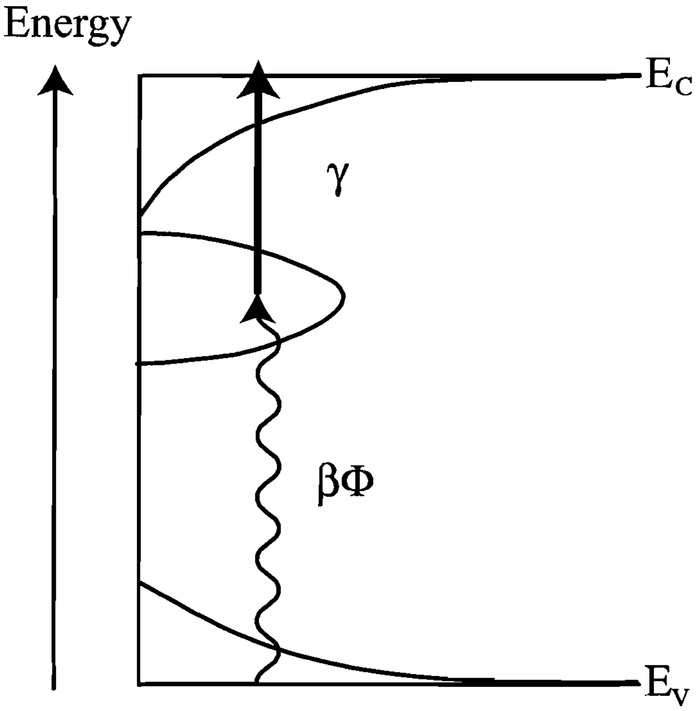

Figure 4.18. Schematic representation of a defect that is optically filled and thermally emptied. γ is the thermal emptying rate, and βΦ is the optical filling rate.

By deducing the step temperature and assuming an optical cross section for the filling rate and a thermal emission prefactor for the emptying rate, we can calculate the approximate energy depths of the defects with respect to the conduction band. We then estimate the energy depths to be 370meV, 400meV, and 460meV below the conduction band for the devices with S/VI= 0.56, 0.33, and 0.12 respectively.

Note that the sum of the energy position of the optical defect and the energy depth beneath conduction band in all cases is very close to the known bandgaps of the devices of 1.5eV.

Given the optical defect positions in CIGS devices [3, 10], we should be able to observe similar transitions through defects in CIGS alloys. The energetic depth of the 0.8eV optical defect for Ga/III=0.3 CIGS should be ~400meV, similar to the pentenary CIGSS device with Ga/III=0.51 and S/VI=0.33. We measured the RDS on a series of CIGS devices with differing gallium contents, taking care to keep the wavelength of light used to record the "above band" signal just below the bandgap of the material. Ge-window filtered white light was still used for the defect signal. As shown in Figure 4.19, no such steps were observed at the expected temperatures, or at any temperature available

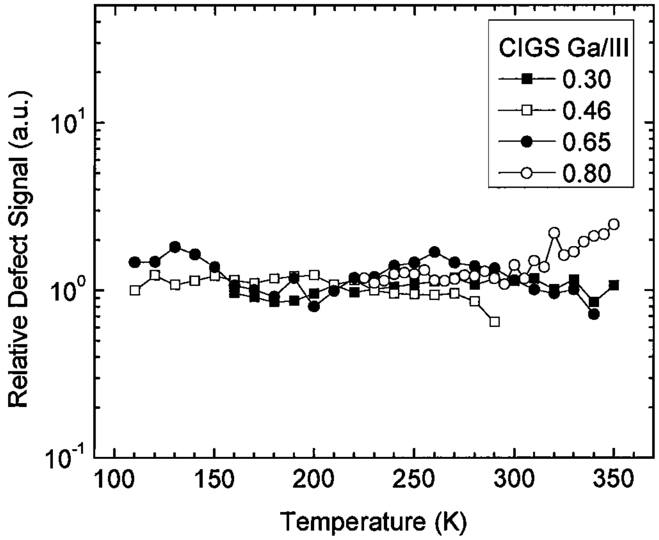

Figure 4.19. Relative defect signal versus temperature for a wide range of quaternary CIGS devices with varying cation fractions.

to us.

This interesting result points to the role of sulfur in facilitating the thermal transition from the defect into the conduction band. Thus we were led to perform similar measurements on the sulfur containing CISSe devices. Shown in figure 4.20 are matched RDS spectra for the pentenary CIGSSe and quaternary CISSe devices with similar chalcogen ratio.

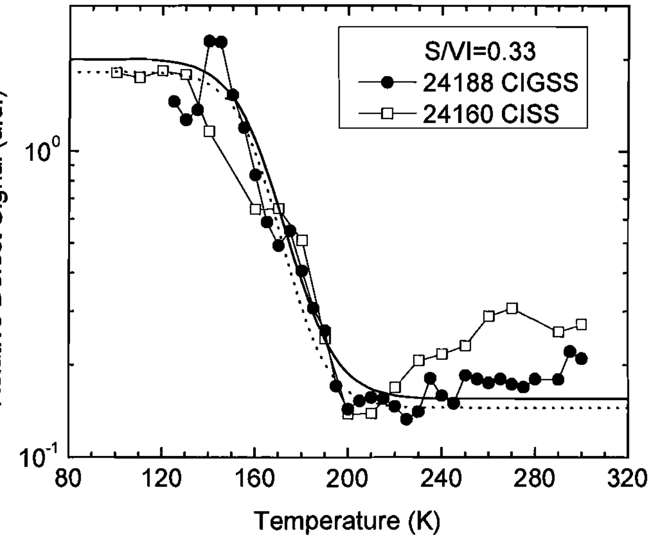

(a)

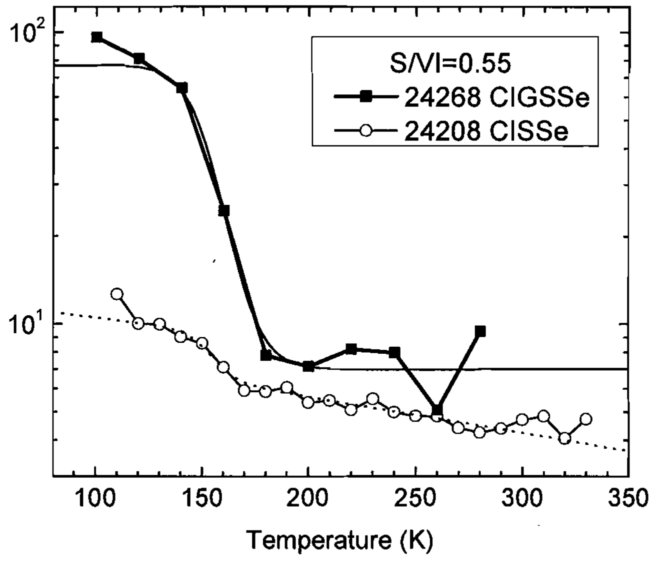

(b)

Figure 4.20. Relative defect signal spectra for partner CISSe and CIGSSe devices with similar sulfur content. **(a)** RDS spectra for the two devices with S/VI=0.33. Step function fits have been added as a guide to the eye. **(b)** RDS spectra for the two devices with S/VI≈0.55. Step function fits have been added as a guide to the eye.

It is clear from the figure that step-like temperature dependence in the RDS spectra exist in the quaternary CISSe devices. Perhaps most surprising though, is that the steps for quaternary and pentenary partner (similar sulfur content) devices occur at the *same temperature.* Step-function fits have been added to the data to guide the eye and give a quantitative sense of the step position. For the S/VI=0.33 devices in figure 4.20a, the steps are located at 151K and 153K for devices 24268 and 24208 respectively. In figure 4.20b, the steps are located at 160K for both S/VI≈0.55 devices. The size of the step for device 24160 is much smaller than its pentenary partner, and the RDS signal in the high temperature regime exhibits a slight slope, possibly indicating minority carrier collection decreasing with temperature via a different mechanism than that creating the step.

A possible explanation for the coincident step temperatures could be overlap of the conduction bandtail and the deep optical defect band. Then an electron excited into the defect band could be excited into the bandtail and collected at the electrode. Examining figures 4.15 and 4.5 we see that the defect bands and the bandtails in these devices *do* overlap. However, this does not explain the role of sulfur in facilitating the transition where non-sulfur containing materials cannot.

It would be interesting to measure the thermal emission prefactor for the defect to more accurately determine its properties. However, attempts to observe the step on different measurement timescales to determine the time-window dependence were inconclusive.

4.5 Characterization of $Cu(In_xGa_{1-x})(Se_yS_{1-y})_2$ Thin Film Solar Cell Devices with Constant Chalcogen Ratio

We have recently undertaken an investigation of a final set of pentenary CIGSSe devices with a constant sulfur content S/VI≈0.25. This ratio was chosen by examination of the efficiencies of the devices in the previous two studies, noting that the devices with S/VI≈0.3 had the highest efficiencies in each group. To study the effect of this small addition of sulfur, and hopefully further elucidate the steps in the RDS spectra, we requested that devices with constant sulfur content and variable indium and gallium contents be grown.

It should be noted that the efficiencies of most of these devices are very good, in particular for those with lower gallium content. The devices with Ga/III= 0.48, 0.38, and 0.29 had efficiencies of 13%, 14.6%, and 15% respectively. While these efficiencies certainly aren't as high as world record CIGS devices, they are very good for wider bandgap devices.

4.5.1 Electrical Characterization of $Cu(In_xGa_{1-x})(Se_yS_{1-y})_2$ Thin Film Solar Cell Devices with Constant Chalcogen Ratio

Results from admittance measurements on all five devices are summarized in Figure 4.21. All five devices showed activated behavior, in some cases more than one capacitance step. Activation energies seemed to come in both shallow and deep regimes, with deep activation energies ranging between 196meV to 328meV, and shallow activation energies from 40meV to 80meV. None of the devices showed evidence of a geometric capacitance limit, indicating that the charge densities are high enough for the sample to not be depleted even at low temperatures.

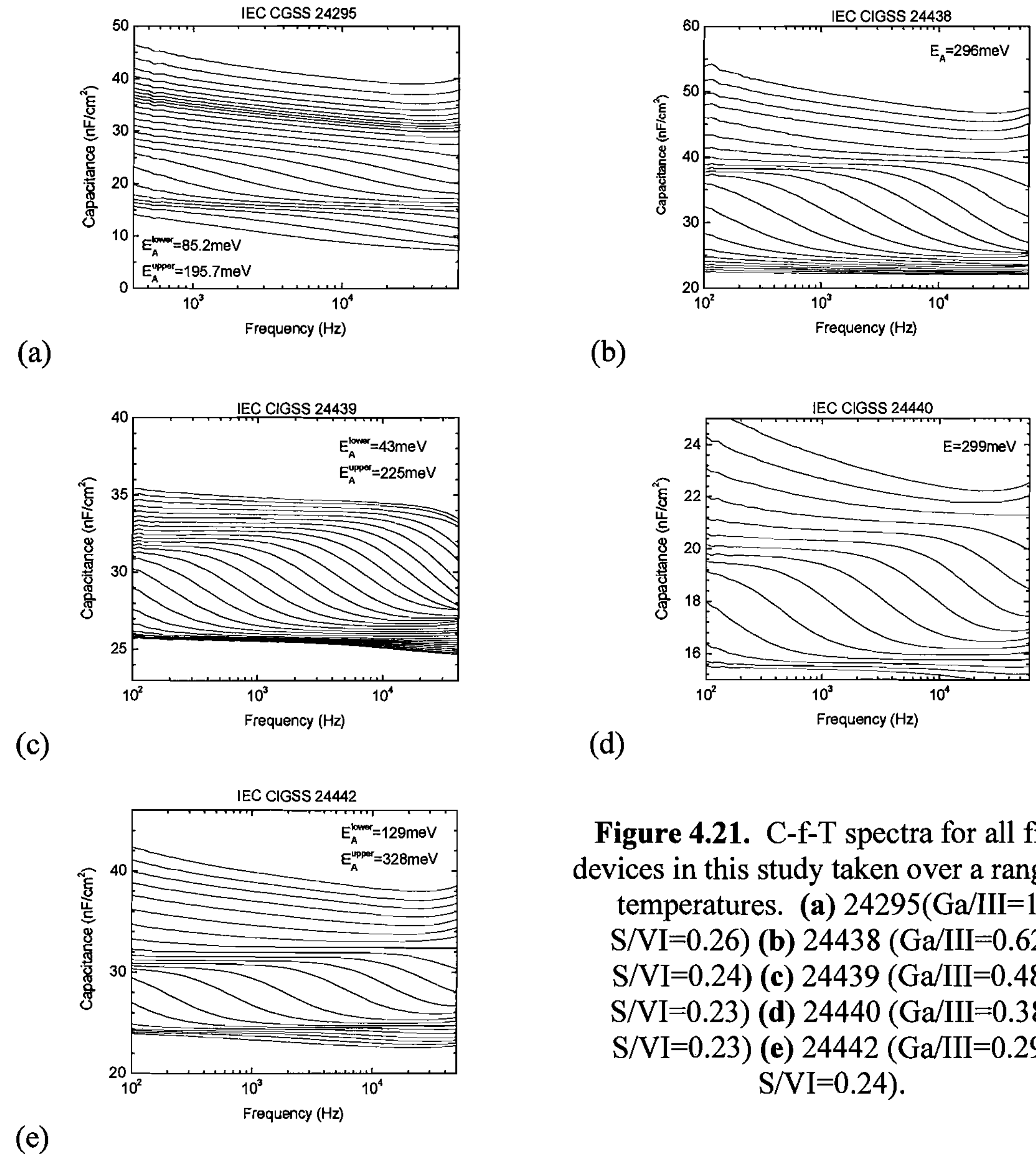

(a)

(b)

(c)

(d)

(e)

Figure 4.21. C-f-T spectra for all five devices in this study taken over a range of temperatures. **(a)** 24295(Ga/III=1, S/VI=0.26) **(b)** 24438 (Ga/III=0.62, S/VI=0.24) **(c)** 24439 (Ga/III=0.48, S/VI=0.23) **(d)** 24440 (Ga/III=0.38, S/VI=0.23) **(e)** 24442 (Ga/III=0.29, S/VI=0.24).

DLCP and CV measurements are summarized in figures 4.22 and 4.23 for two of the devices. Figure 4.22 shows a geometric width of the film near 1.7μm, and a free carrier density near 4x10^{14} cm^{-3}. As the temperature of the measurement is increased ,the DLCP densities increase, appearing to reach a limit at the same magnitude as the CV profiles. We infer a deep defect density of 2 x10^{15} cm^{-3} for this device.

Figure 4.23 shows DLC and CV profiles for device 24440 which are very non-unifo. DLCP densities are highly peaked at larger profile depths, although the geometric limit of the film has not been reached. The CV densities however indicate a much higher defect density. This would seem to indicate a large charge density that is not able to dynamically respond to the ac-perturbation of the DLCP measurement, but is changing the overall capacitance scale. The CV profiles do appear to show a defect activating with increasing temperature,

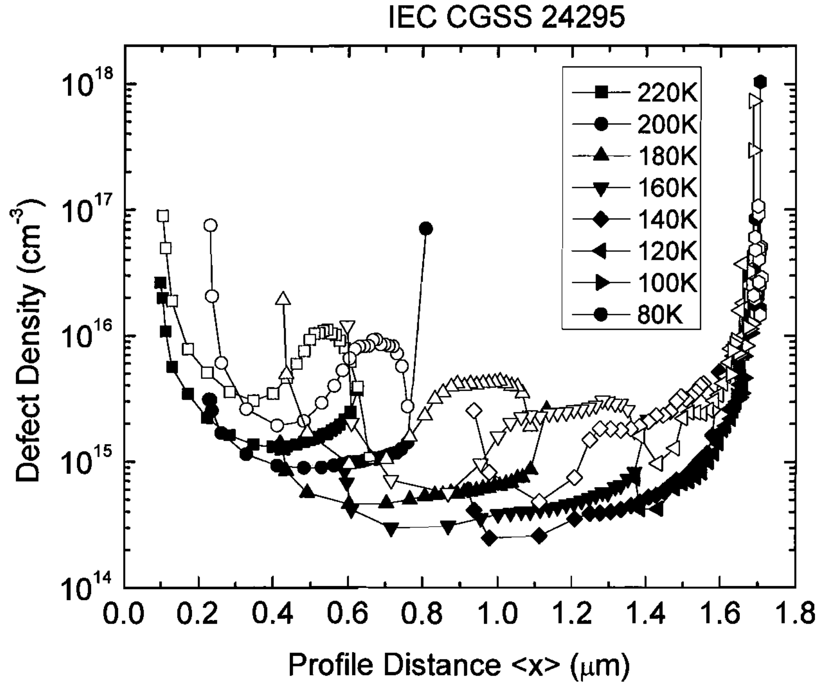

Figure 4.22. DLC and CV profiles for IEC CGSSe device 24295 (Ga/III=1, S/VI=0.26) at 30kHz. Voltages ranged from -1.6V to 0.8V in steps of 0.1V. DLCP densities are in solid symbols, and CV densities in open symbols.

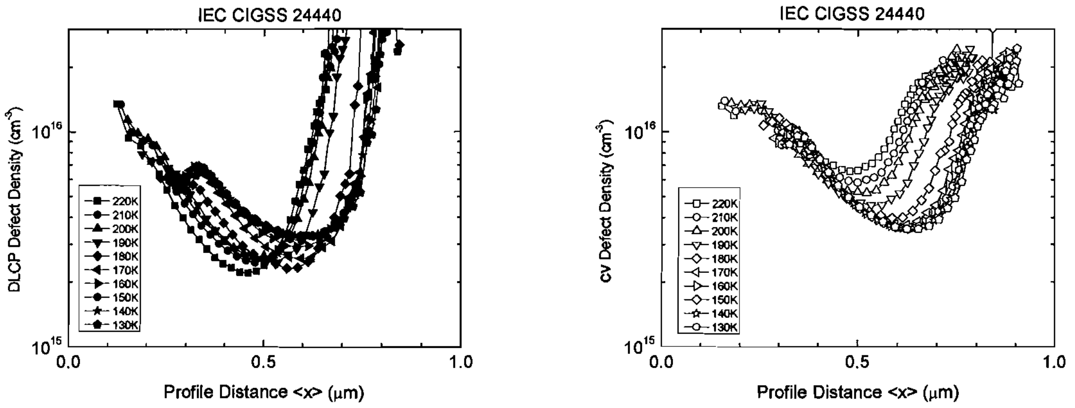

Figure 4.23 **(a)** DLC profiles for IEC CIGSSe device 24440 (Ga/III=0.38, S/VI=0.23) taken at 3.3kHz over a voltage range from -3.8V to 0.8V in 0.1V steps. **(b)** Simultaneously collected CV profiles.

however they do not achieve a limiting value. We can only then put a lower limit on the defect density for this device of ~5×10^{15} cm^{-3}.

Results from electrical measurements on these devices are summarized in Table 4.6.

Table 4.6. Electrical measurement results for CIGSSe devices with constant chalcogen ratio.

Sample	Ga/III	p (10^{15} cm^{-3})	N_d (10^{15} cm^{-3})	E_A (meV)	ν (10^x sec^{-1})	W_d (μm)
24295	1	0.4	2	82.5 195.7	10 9	0.63
24438	0.62	6	10	296	11	0.45
24439	0.48	8	10	43 225	7 11	0.41
24440	0.38	2	>5	299	12	0.63
24442	0.29	8	2	129 328	9 13	0.41

4.5.2 Optical Characterization of Cu(In$_x$Ga$_{1-x}$)(Se$_y$S$_{1-y}$)$_2$ Thin Film Solar Cell Devices with Constant Chalcogen Ratio

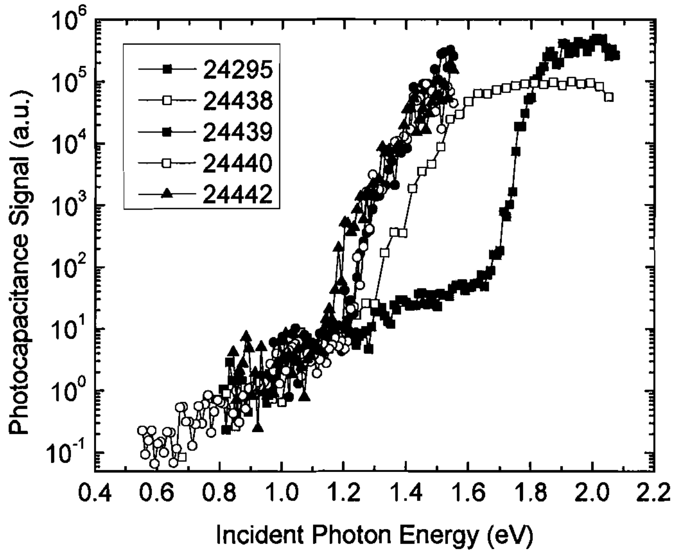

Figure 4.24. TPC spectra at 180K for the five constant chalcogen ratio pentenary devices.

In figure 4.24 TPC spectra for all five devices taken at 180K are shown. Notable are the variations in bandgaps with gallium alloying, particularly for high gallium contents, and the striking similarity in the defect structure. This similarity is reminiscent of the defect structure seen in $Cu(In_xGa_{1-x})Se_2$ alloys [3]. However, a Gaussian fit to this defect required an energetic depth of 1.6eV for the defect! This is larger than the bandgap of most of the devices, and is likely not a correct interpretation of the signal in the sub-bandgap regime of these devices. More likely the signal in this regime is simply reflecting the convolution of the density of states at the edge of the valence band with a continuous distribution of gap states.

Also of note in Figure 4.24 is the "lean over" of the bandtails in the two devices with the least gallium content. TPI spectra do not show such a feature, but rather the bandtail continues to rise up to the bandgap. This indicates that there may be some cancellation in this regime from electrons being collected in large enough numbers to affect the capacitance signal.

At the time of this writing, RDS spectra are under way. It will be interesting to see if there is a step in the RDS signal, and whether or not it is at the same temperature for all five CIGSSe devices, as one would predict from their chalcogen ratios and the results from sections 4.3 and 4.4.

Table 4.7. Optical fitting parameters for constant chalcogen ratio CIGSSe devices.

Sample	Ga/III	S/VI	E_{Urbach} (meV)
24295	1	0.26	18
24438	0.62	0.24	38
24439	0.48	0.23	30
24440	0.38	0.23	22
24442	0.29	0.24	26

4.6 Discussion

The role of sulfur alloying in CISe and CIGSe alloys has been studied in detail for a broad range of absorber compositions. Substitution of sulfur for selenium was hoped to provide a new pathway to efficient wide bandgap absorber materials useful in single and multi-junction thin-film photovoltaic devices. Sulfur containing CISSe and CIGSSe alloys were characterized in their finished device configuration using advanced junction capacitance techniques including admittance spectroscopy, drive-level capacitance profiling, and transient optical spectroscopies.

Admittance spectra for most devices showed broad activation steps with increasing temperature and decreasing frequency. The activation energies of these steps were larger than those typically seen in CIGS devices, and tended to increase in energy with increased sulfur alloying. These activation energies are typically identified as the energy difference between the valence band and the energy of the responding defect within the bandgap [22]. Larger activation energies correlated with increasing sulfur content may reflect the increased energy difference between the defect level and the valence band as the valence band is moved to lower energies and the defect energy remains unchanged. The larger activation energies of the defects imply a slower hole release rate from the defect, which would increase the probability of recombination through these defects.

Defect profiling techniques showed lower free hole carrier densities than those typically seen in CIGS films. Again, this may reflect the increased energy difference between the majority carrier band (valence band) and the shallow dopant levels due to sulfur alloying. In addition, many of the defect profiles seen in these devices were spatially non-uniform. This may reflect the segregation of sulfur towards the front and back of the film, as has been observed in a variety of profiling techniques [8, 13, 22]. Simultaneous incorporation of Se and S in thin films has proven difficult due to differences in the between S and Se fluxes delivered to the film during growth and the final incorporation of Se and S in the CIGSSe film [8].

The spatial non-uniformity of these films may be an explanation for the broad bandtails seen in transient photocapacitance and photocurrent measurements. CIGS devices studied previously had Urbach energies near 20 meV [3, 10], whereas the pentenary devices studied here ranged as high as 38 meV. The performance of these devices appears to be dominated by the compositional disorder inherent in the films both due to the larger alloy system and the difficulties with uniform chalcogen incorporation.

However, rich defect physics have been observed through analysis of the temperature dependence of the relative defect signal in the CISSe and CIGSSe devices. We have been able to observe a defect that is optically filled with electrons from the valence band which are thermally emptied into the conduction band. By measuring the occupation of the defect as a function of temperature, we are able to observe a change in the relative defect signal (RDS) when there is no longer enough thermal energy to emit the electron to the conduction band on the timescale of the experiment. Remarkably, the step in the RDS occurs at exactly the same temperature for CISSe and CIGSSe devices with similar sulfur contents, despite different energy differences between the observed optical defect and the conduction bands. Another piece in the puzzle is the lack of any such step in non-sulfur-containing CIGS devices with a broad range of bandgaps. These data point to the role of sulfur in the formation of a charge trapping defect that may have a detrimental effect on the performance of the material as a photovoltaic absorber. Further measurements to elucidate the role of sulfur in these optical and thermal transitions through defects are ongoing.

Notes

[1] K. Ramanathan, M. A. Contreras, C. L. Perkins, S. Asher, F. S. Hasoon, J. Keane, D. Young, M. Romero, W. Metzger, R. Noufi, J. Ward, and A. Duda, Prog. Photovolt.: Res. Appl. **11**, 225 (2003).

[2] R. Herberholz, V. Nadenau, U. Ruhle, C. Koble, H. W. Schock, and B. Dimmler, Sol. En. Mater. and Solar Cells **49**, 227 (1997).

[3] J. T. Heath, J. D. Cohen, W. N. Shafarman, D. X. Liao, and A. A. Rockett, Appl. Phys. Lett. **80**, 4540 (2002).

[4] S.-H. Wei and A. Zunger, J. Appl. Phys. **78**, 3846 (1995).

[5] D. G. Kilday, G. Margaritondo, T. F. Ciszek, S. K. Deb, W.-H. Wei, and A. Zunger, Phys. Rev. B **36**, 9388 (1987).

[6] J. E. Jaffe and A. Zunger, Phys. Rev. B **28**, 5822 (1983).

[7] M. Turcu, I. M. Kotschau, and U. Rau, J. Appl. Phys. **91**, 1391 (2002).

[8] M. Gossla and W. N. Shafarman, Thin Solid Films **480-481**, 33 (2005).

[9] M. Bar, W. Bohne, J. Rohrich, E. Strub, S. Lidner, M. C. Lux-Steiner, C.-H. Fischer, T. P. Niesen, and F. Karg, J. Appl. Phys. **96**, 3857 (2004).

[10] J. T. Heath, in *Department of Physics* (University of Oregon, Eugene, 2002), p. 148.

[11] B. Eisener, D. Wolf, and G. Muller, Thin Solid Films **361-361**, 126 (2000).

[12] M. Turcu and U. Rau, J. Phys. Chem. Solids **64**, 1591 (2003).

[13] L. L. Kazmerski, M. S. Ayyagari, and G. A. Sanborn, J. Appl. Phys. **46**, 4865 (1975).

[14] D. C. Look and J. C. Manthuruthil, J. Phys. Chem. Solids **37**, 173 (1976).

[15] J. Kneisel, K. Siemer, I. Luck, and D. Braunig, J. Appl. Phys. **88**, 5474 (2000).

[16] A. Luque and S. Hegedus, *Handbook of Photovoltaic Science and Engineering*, Hoboken, 2003).

[17] M. Green, Prog. Photovolt.: Res. Appl. **9**, 123 (2001).

[18] C. H. Henry, J. Appl. Phys. **51**, 4494 (1980).

[19] A. D. Vos, J. Phys. D.: Appl. Phys. **13**, 839 (1980).

[20] J. T. Heath, J. D. Cohen, and W. N. Shafarman, in *Materials Research Society* (MRS, San Francisco, CA, 2003), Vol. 763, p. B9.2.1.

[21] J. D. C. J. T. Heath, and W. N. Shafarman, Journal of Applied Physics **95**, 1000 (2004).

[22] P. K. Johnson, J. T. Heath, J. D. Cohen, K. Ramanathan, and J. R. Sites, Prog. Photovolt.: Res. Appl. **13**, 579 (2005).

CHAPTER V

SUMMARY AND DISCUSSION OF RESULTS

The electronic properties of sulfur-containing $CuIn(S_ySe_{1-y})_2$ and $Cu(In_xGa_{1-x})(S_ySe_{1-y})_2$ thin-film materials have been studied using advanced junction capacitance techniques. These measurements have been applied to finished devices in a working thin-film solar cell device structure. Due to the one-sided nature of these devices, we are able to isolate the differential capacitance response of the absorber material under study in its working environment. This is particularly important because the properties of these materials are heavily affected by their environment.

Measurements employed in this characterization study include admittance spectroscopy, drive-level capacitance and capacitance-voltage profiling, and transient photocapacitance and photocurrent spectroscopies [1-4]. Admittance spectroscopy records the complex current response to a perturbing ac voltage and provides general information about the energetic structure of the electronic levels within the device. Typical information learned using admittance spectroscopy includes defect activation energies, depletion widths, and geometric widths of the device.

We complement our admittance measurements with two defect profiling measurements: drive-level capacitance profiling (DLCP) and capacitance-voltage profiling (CV). CV is a well-known measurement typically used to determine doping levels in semiconductors. However, due to the disordered nature of the devices under study in this thesis there is a significant continuous distribution of defect states within the bandgap of these devices. DLCP is a more sophisticated profiling technique that measures the dynamic response of defect states to a varying amplitude ac perturbation. DLCP was conceived in order to profile such complicated densities of states. These profiling techniques are used to determine spatial defect and free carrier profiles in the devices.

Transient photocapacitance (TPC) and transient photocurrent (TPI) measurements are optical measurements that give spectra similar to absorption spectra. However, because the signals from these measurements result from optically excited charge, they are sensitive to the charge collection dynamics inherent in these devices. In addition they are extremely sensitive, and are able to resolve deep defect structure in the sub-bandgap energy regime.

Previous studies using these methods on $Cu(In_xGa_{1-x})Se_2$ devices showed the existence of a deep defect located at 0.8eV above the valence band, regardless of the Ga content [1, 5]. Ga alloying increases the bandgap of CIGSe materials predominantly by moving the conduction band minimum to higher energies [6]. Thus, as the bandgap of CIGSe materials is widened through Ga-alloying, this defect effectively moves to the center of the gap and possibly becomes a detrimental recombination center. This may explain the rolloff of the open-circuit voltage of higher gap (E_{gap}>~1.3eV) alloys of CIGSe, leading to poor efficiencies in higher gap CIGSe devices [7].

Sulfur alloying provides a new pathway for engineering the bandgap of CIGSe devices. Sulfur alloying increases the bandgap of CIGSe both by moving the valence band maximum to lower energies, and the conduction band minimum to higher energies [6]. Thus, more sophisticated alloys are possible which may be able to achieve higher open-circuit voltage devices.

Admittance spectroscopy measurements showed activated defect signatures in most of the alloys studied. The activation energies we measured were larger than those typically seen in CIGSe devices with similar deposition methods and finishing layers. The activation energies tended to increase with increased sulfur alloy fraction. Additionally a decrease in the measured free carrier densities was observed using DLCP measurements at high frequency and low temperature. The decrease in free carrier densities also scaled with increased sulfur alloy fraction. These results are consistent with each other in that CIGSe materials are natively doped by their intrinsic defects. The shallow acceptor level that gives rise to the free carriers is thought to be due to copper vacancies (V_{Cu}). Thus, as the bandgap is widened with sulfur alloying, the valence band maximum moves away from the shallow dopant level, increasing the measured activation energies and decreasing the free carrier density. These results are summarized for all the devices in this study in figure 5.1.

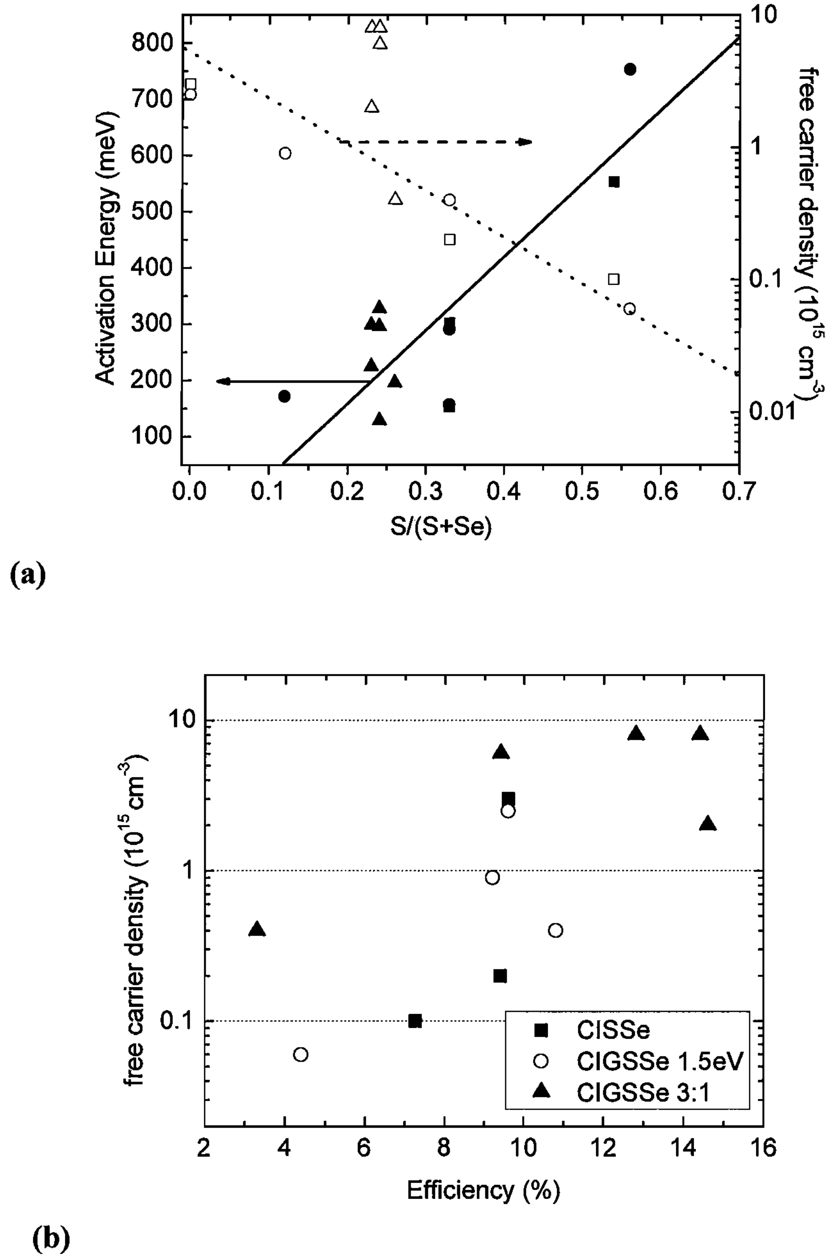

Figure 5.1. **(a)**Activation energies and free carrier densities for the devices studied. The sample series is given by the symbol type: squares are CISSe devices, circles are wide-bandgap CIGSSe devices, and triangles are CIGSSe devices with constant chalcogen ratio. The lines have been drawn as guides to the eye, displaying the trends of increasing activation energies and decreasing free carrier densities with sulfur alloy fraction. **(b)** Free carrier densities and device efficiency appear positively correlated.

In addition to the overall defect and free carrier densities, defect profiling measurements showed significant spatial variations for sulfur containing devices. This may reflect difficulty in uniform incorporation of sulfur in the films, in particular when being deposited simultaneously in the presence of selenium [8, 9]. The spatial nonuniformities are particularly evident in comparison to non-sulfur containing films, an example of which is shown in figure 4.9a.

TPC and TPI measurements revealed a rich sub-bandgap absorption structure, including broad bandtails and defect bands. The bandtails reflect the disorder in the devices. For these devices the disorder is primarily compositional. Compositional disorder results from deviations from the ideal arrangements of cation and anion species in the lattice. In the pentenary CIGSSe alloy systems, the ideal arrangement of elements

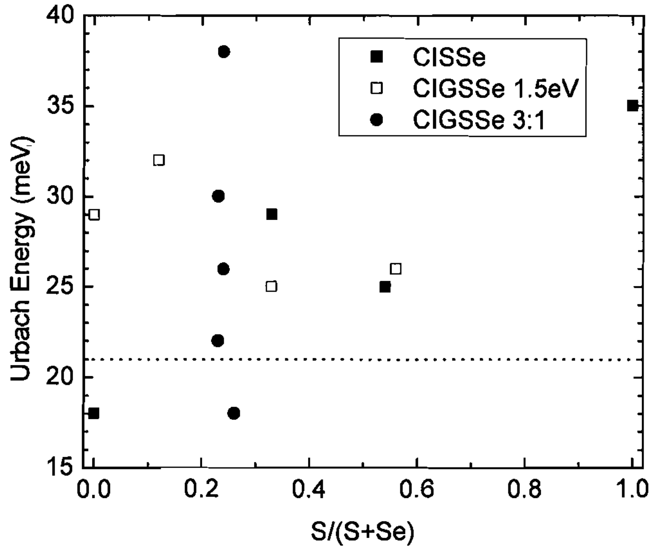

Figure 5.2. Urbach energies for the devices measured in this study. A fiducial line at the average measured value of the Urbach energy for quaternary CIGSe devices has been added for reference.

becomes ambiguous due to the underdetermined nature of how the crystal structure accommodates the five different elements. Figure 5.2 shows Urbach energies for the devices measured in this study compared to the average Urbach energy measured for a series of quaternary $Cu(In_xGa_{1-x})Se_2$ devices [5]. The Urbach energies for a majority of the devices are much larger than those typically seen in CIGSe devices, which indicates an increasing amount of compositional disorder due to the larger alloy system.

Urbach energies also anti-correlate with the device conversion efficiency. This is plausible because compositional disorder is the source of many of the intrinsic defects in these materials, many of which can have a detrimental effect on performance. These data are shown in figure 5.3. It is important to point out that the data point for CIGSSe device 24295 has been left off of this graph. This device has an exceptionally large bandgap near 1.9eV, and would not be expected to be an efficient converter of light from the solar spectrum. In addition we have added a data point for the most efficient CIGSe device from a previous study in this lab as a point of reference [1, 5]. This 16.1% efficient device has a Ga content of Ga/III=0.32, which gives a bandgap of E_{gap}=1.20eV. Its composition is similar to the world-record thin-film solar cell grown using more advanced techniques [10].

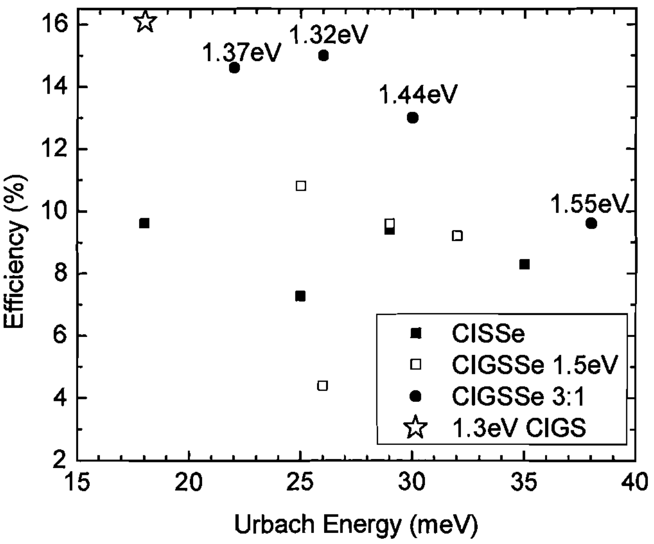

Figure 5.3. Anti-correlation of efficiency and Urbach energy. A high efficiency CIGSe device has been added to the plot as a reference as well as bandgap energies for the highest efficiency devices.

We also observed distinct temperature dependence in the photocapacitance spectra taken on the sulfur containing devices. At lower temperatures we saw an increase in the TPC signal in the defect region of the spectrum. In order to more fully characterize this effect we measured the relative defect signal (RDS), that is the ratio of the TPC signal taken with sub-bandgap light in the defect region to the TPC signal taken with monochromatic light of energy just below the bandgap, as a function of temperature. RDS spectra showed significant temperature dependence in the form of step-like increases in signal as the measurement temperature was lowered. We believe that these steps represent the turn-off of a thermal pathway for optically excited electrons in the defect to be thermally emitted into the conduction band. By assuming a thermal emission prefactor of 10^{12} sec^{-1} we were able to calculate the energy difference between the defect and the conduction band. In figure 5.4 we plot these energy differences versus the conduction band offsets that would be expected for the different alloys calculated from [6].

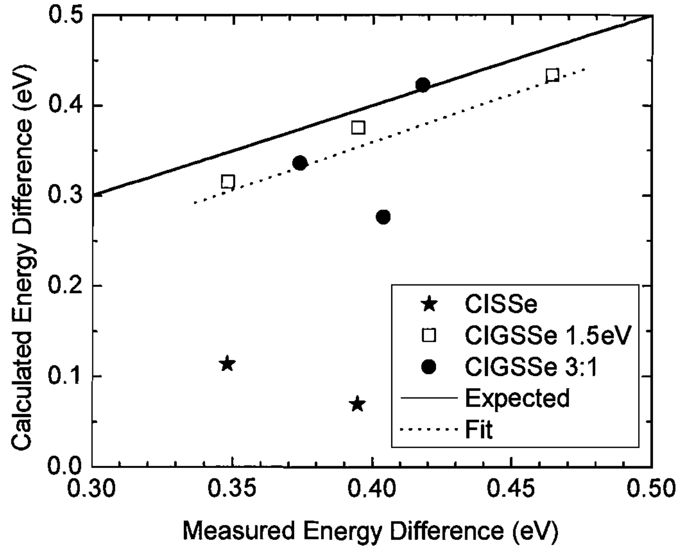

Figure 5.4. Measured and expected energy differences between the optical defect and the conduction band. The fitting was performed on only the pentenary CIGSSe devices from both studies. The expected line is a line with a slope equal to one.

As can be seen in figure 5.4, the pentenary alloys from both the wide-bandgap and the constant chalcogen ratio studies lie along a line parallel to the expected energy difference. There is a 40meV offset between the fitted line and the expected line that may reflect a difference between our assumed thermal emission prefactor and the actual thermal emission prefactor. If one assumes a thermal emission prefactor of $\nu=2*10^{11}$ sec^{-1}, the fitted and expected lines nearly coincide.

The step-like behavior in the RDS signal was also observed in the CISSe devices. Surprisingly the steps occurred at the same temperature at which the steps occurred for the pentenary device with similar sulfur content. This is in spite of radically different energy differences between the defect band and the conduction bands in the two alloys, as can be seen in the star-symbol data in figure 5.4. This may reflect uncertainties in the energetic position of the defect band as determined using TPC measurements. However, this does not explain the coincidence between of the RDS step temperatures between the matched sulfur content CISSe and CIGSSe devices.

Perhaps most surprising is that no steps were seen in a range of CIGSe devices. This is despite conduction band offsets from the well-documented optical defect located 0.8eV above the valence band that should be comparable to those in the CIGSSe devices. The presence of sulfur in the devices seems to be a prerequisite for the observation of the steps in the RDS spectra. The sulfur is either the source of a new defect level within the bandgap of the material, or it is the source of a pathway for charge to thermally escape from the defect observed in CIGSe. There are several possibilities to consider:
(1) broadening due to sulfur incorporation and the associated compositional disorder may facilitate the overlap of the defect band and bandtails which could provide an escape pathway, (2) a sulfur related point defect with different characteristics than those seen in studies of CIGSe may be optically active within the bandgap of the sulfur containing materials, (3) or sulfur incorporation may provide an as yet unknown thermal pathway for thermal escape for the electrons excited into the defect.

Notes

[1] J. T. Heath, J. D. Cohen, W. N. Shafarman, D. X. Liao, and A. A. Rockett, Appl. Phys. Lett. **80**, 4540 (2002).

[2] J. T. Heath, J. D. Cohen, and W. N. Shafarman, J. Appl. Phys. **95**, 1000 (2004).

[3] C. E. Michelson, A. V. Gelatos, and J. D. Cohen, Appl. Phys. Lett. **47**, 412 (1985).

[4] A. V. Gelatos, K. K. Mahavadi, and J. D. Cohen, Appl. Phys. Lett. **53**, 403 (1988).

[5] J. T. Heath, in *Department of Physics* (University of Oregon, Eugene, 2002), p. 148.

[6] S.-H. Wei and A. Zunger, J. Appl. Phys. **78**, 3846 (1995).

[7] R. Herberholz, V. Nadenau, U. Ruhle, C. Koble, H. W. Schock, and B. Dimmler, Sol. En. Mater. and Solar Cells **49**, 227 (1997).

[8] M. Gossla and W. N. Shafarman, Thin Solid Films **480-481**, 33 (2005).

[9] I. M. Kotschau, M. Turcu, U. Rau, and H. W. Schock, Materials Research Society Proceedings **668** (2001).

[10] K. Ramanathan, M. A. Contreras, C. L. Perkins, S. Asher, F. S. Hasoon, J. Keane, D. Young, M. Romero, W. Metzger, R. Noufi, J. Ward, and A. Duda, Prog. Photovolt.: Res. Appl. **11**, 225 (2003).

REFERENCES

Chapter I

[1] U.S. Department of Energy, *International Energy Outlook 2007* (Energy Information Administration Office of Integrated Analysis and Forecasting, 2007).

[2] U.S. Department of Energy, *Basic Research Needs for Solar Energy Utilization*, (Energy Information Administration Office of Integrated Analysis and Forecasting 2005).

[3] M. A. Green, Prog. Photovolt.: Res. Appl. **9**, 123 (2001).

[4] K. Ramanathan, M. A. Contreras, C. L. Perkins, S. Asher, F. S. Hasoon, J. Keane, D. Young, M. Romero, W. Metzger, R. Noufi, J. Ward, and A. Duda, Prog. Photovolt.: Res. Appl. **11**, 225 (2003).

[5] M. Gossla and W. N. Shafarman, Thin Solid Films **480-481**, 33 (2005).

[6] R. Herberholz, V. Nadenau, U. Ruhle, C. Koble, H. W. Schock, and B. Dimmler, Sol. En. Mater. and Solar Cells **49**, 227 (1997).

[7] J. T. Heath, PhD dissertation, (University of Oregon, Eugene, 2002), p. 148.

[8] J. T. Heath, J. D. Cohen, W. N. Shafarman, D. X. Liao, and A. A. Rockett, Appl. Phys. Lett. **80**, 4540 (2002).

[9] R. N. Hall, Phys. Rev. **87**, 387 LP (1952).

[10] W. Shockley and W. T. Read, Phys. Rev. **87**, 835 LP (1952).

Chapter II

[1] S. M. Sze, *Semiconductor Devices, physics and technology* (John Wiley & Sons, Inc., 2002).

[2] A. Luque and S. Hegedus, *Handbook of Photovoltaic Science and Engineering*, Hoboken, 2003).

[3] T. Markvart and L. Castaner, *Photovoltaics, fundamentals and applications* (Elsevier Ltd., New York, 2003).

[4] R. H. Bube, *Photovoltaic Materials* (Imperial College Press, London, 1998).

[5] U. Rau, Appl. Phys. Lett. **74**, 111 (1999).

[6] S. S. Hegedus and W. N. Shafarman, Prog. Photovolt.: Res. Appl. **12**, 155 (2004).

[7] K. Ramanathan, M. A. Contreras, C. L. Perkins, S. Asher, F. S. Hasoon, J. Keane, D. Young, M. Romero, W. Metzger, R. Noufi, J. Ward, and A. Duda, Prog. Photovolt.: Res. Appl. **11**, 225 (2003).

[8] J. S. Toll, Phys. Rev. **104**, 1760 (1956).

[9] J. D. Jackson, *Classical Electrodynamics* (John Wiley & Sons, Inc., New York, 1998).

[10] J. D. C. J. T. Heath, and W. N. Shafarman, Journal of Applied Physics **95**, 1000 (2004).

[11] D. Mencaraglia, S. O. Saad, and Z. Djebbour, Thin Solid Films **431-432**, 135 (2003).

[12] D. L. Losee, J. Appl. Phys. **46**, 2204 (1975).

[13] J. D. Cohen and D. V. Lang, Phys. Rev. B **25**, 5321 (1982).

[14] J. G. Simmons and G. W. Taylor, Phys. Rev. B **4**, 502 (1971).

[15] J. Kneisel, K. Siemer, I. Luck, and D. Braunig, J. Appl. Phys. **88**, 5474 (2000).

[16] J. Lee, J. D. Cohen, and W. N. Shafarman, Thin Solid Films **480-481**, 336 (2005).

[17] J. T. Heath, in *Department of Physics* (University of Oregon, Eugene, 2002), p. 148.

[18] C. Rincon, M. A. Arsene, S. M. Wasim, F. Voillot, J. P. Peyrade, P. Bocaranda, and A. Albacete, Mat. Lett. **29**, 87 (1996).

[19] C. E. Michelson, A. V. Gelatos, and J. D. Cohen, Appl. Phys. Lett. **47**, 412 (1985).

[20] J. T. Heath, J. D. Cohen, and W. N. Shafarman, Thin Solid Films **431-432**, 426 (2003).

[21] R. Herberholz, U. Rau, H. W. Schock, T. Haalboom, T. Godecke, F. Ernst, C. Beilharz, K. W. Benz, and D. Cahen, Eur. Phys. Jour. Appl. Phys. **6**, 131 (1999).

[22] P. Zabierowski, U. Rau, and M. Igalson, Thin Solid Films **387**, 147 (2001).

[23] M. Igalson, M. Bodegard, L. Stolt, and A. Jasenek, Thin Solid Films **431-432**, 153 (2003).

[24] U. Rau, K. Weinert, Q. Nguyen, M. Mamor, G. Hanna, A. Jasenekc, and H. W. Schock, Materials Research Society Proceedings **668**, H.9.1.1 (2001).

[25] A. Halverson, J. Mattheis, U. Rau, and J. D. Cohen, in *Conference Record of the 2006 IEEE 4th World Conference on Photovoltaic Energy Conversion* (IEEE, Hawaii, USA, 2006), Vol. 1, p. 519.

[26] A. O. Pudov, J. R. Sites, M. A. Contreras, T. Nakada, and H.-W. Schock, Thin Solid Films **480-481**, 273 (2005).

[27] S. Lany and A. Zunger, J. Appl. Phys. **100**, 1 (2006).

[28] J. T. Heath, J. D. Cohen, W. N. Shafarman, D. X. Liao, and A. A. Rockett, Appl. Phys. Lett. **80**, 4540 (2002).

[29] R. Herberholz, V. Nadenau, U. Ruhle, C. Koble, H. W. Schock, and B. Dimmler, Sol. En. Mater. and Solar Cells **49**, 227 (1997).

[30] A. Niemegeers, M. Burgelman, R. Herberholz, U. Rau, D. Hariskos, and H.-W. Schock, Prog. Photovolt.: Res. Appl. **6**, 407 (1998).

[31] M. Igalson, A. Kubiaczyk, and P. Zabierowski, in *2001 MRS Spring Meeting*, San Francisco, USA, 2001), Vol. 668.

[32] M. Igalson, in *2007 MRS Spring Meeting* (MRS, San Francisco, USA, 2007), Vol. 1012.

Chapter III

[1] P. D. Paulson, R. W. Birkmire, and W. N. Shafarman, J. Appl. Phys. **94**, 879 (2003).

[2] A. Meeder, D. F. Marron, A. Rumberg, M. C. Lux-Steiner, V. Chu, and J. P. Conde, J. Appl. Phys. **92**, 3016 (2002).

[3] J. T. Heath, in *Department of Physics* (University of Oregon, Eugene, 2002), p. 148.

[4] J. T. Heath, J. D. Cohen, W. N. Shafarman, D. X. Liao, and A. A. Rockett, Appl. Phys. Lett. **80**, 4540 (2002).

[5] D. V. Lang, J. Appl. Phys. **45**, 3023 (1974).

[6] A. V. Gelatos, K. K. Mahavadi, and J. D. Cohen, Appl. Phys. Lett. **53**, 403 (1988).

[7] J. D. Cohen, T. Unold, and A. V. Gelatos, J. Non-Cryst. Solids **141**, 142 (1992).

[8] W. B. Jackson, S. M. Kelso, C. C. Tsai, J. W. Allen, and S.-J. Oh, Phys. Rev. B **31**, 5187 LP (1985).

[9] J. D. C. J. T. Heath, and W. N. Shafarman, Journal of Applied Physics **95**, 1000 (2004).

[10] F. Urbach, Phys. Rev. **92**, 1324 LP (1953).

[11] G. D. Cody, in *Materials Research Society Spring 2005*, San Francisco, CA, 2005), Vol. 862, p. A1.3.1.

[12] G. D. Cody, J. Non-Cryst. Solids **141**, 3 (1992).

[13] C. D. Cody, T. Tiedje, B. Abeles, B. Brooks, and Y. Goldstein, Phys. Rev. Lett. **47**, 1480 (1981).

[14] G. G. Macfarlane, T. P. McLean, J. E. Quarrington, and V. Roberts, Phys. Rev. **111**, 1245 (1958).

[15] M. Beaudoin, A. J. G. DeVries, S. R. Johnson, H. Laman, and T. Tiedje, Appl. Phys. Lett. **70**, 3540 (1997).

[16] H. Sumi and Y. Toyozawa, J. Phys. Soc. Japan **31**, 342 (1971).

[17] S. Lany and A. Zunger, J. Appl. Phys. **100**, 1 (2006).

[18] S. B. Zhang, S. Wei, A. Zunger, and H. Katayama-Yoshida, Phys. Rev. B **57**, 9642 (1997).

[19] S. Lany and A. Zunger, Phys. Rev. B **72**, 1 (2005).

[20] I. Bonalde, E. Medina, M. Rodriguez, S. M. Wasim, G. Marin, C. Rincon, A. Rincon, and C. Torres, Phys. Rev. B **69**, 1 (2004).

[21] S. M. Wasim, C. Rincon, G. Marin, P. Bocaranda, and E. Hernandez, Phys. Rev. B **64**, 1 (2001).

[22] C. H. Grein and S. John, Phys. Rev. B **39**, 1140 (1989).

[23] C. H. Grein and S. John, Phys. Rev. B **41**, 7641 (1990).

[24] S. John, M. Y. Chou, M. H. Cohen, and C. M. Soukoulis, Phys. Rev. B **37**, 6963 (1988).

[25] S. John, C. Soukoulis, M. H. Cohen, and E. N. Economou, Phys. Rev. Lett. **57**, 1777 (1986).

Chapter IV

[1] K. Ramanathan, M. A. Contreras, C. L. Perkins, S. Asher, F. S. Hasoon, J. Keane, D. Young, M. Romero, W. Metzger, R. Noufi, J. Ward, and A. Duda, Prog. Photovolt.: Res. Appl. **11**, 225 (2003).

[2] R. Herberholz, V. Nadenau, U. Ruhle, C. Koble, H. W. Schock, and B. Dimmler, Sol. En. Mater. and Solar Cells **49**, 227 (1997).

[3] J. T. Heath, J. D. Cohen, W. N. Shafarman, D. X. Liao, and A. A. Rockett, Appl. Phys. Lett. **80**, 4540 (2002).

[4] S.-H. Wei and A. Zunger, J. Appl. Phys. **78**, 3846 (1995).

[5] D. G. Kilday, G. Margaritondo, T. F. Ciszek, S. K. Deb, W.-H. Wei, and A. Zunger, Phys. Rev. B **36**, 9388 (1987).

[6] J. E. Jaffe and A. Zunger, Phys. Rev. B **28**, 5822 (1983).

[7] M. Turcu, I. M. Kotschau, and U. Rau, J. Appl. Phys. **91**, 1391 (2002).

[8] M. Gossla and W. N. Shafarman, Thin Solid Films **480-481**, 33 (2005).

[9] M. Bar, W. Bohne, J. Rohrich, E. Strub, S. Lidner, M. C. Lux-Steiner, C.-H. Fischer, T. P. Niesen, and F. Karg, J. Appl. Phys. **96**, 3857 (2004).

[10] J. T. Heath, in *Department of Physics* (University of Oregon, Eugene, 2002), p. 148.

[11] B. Eisener, D. Wolf, and G. Muller, Thin Solid Films **361-361**, 126 (2000).

[12] M. Turcu and U. Rau, J. Phys. Chem. Solids **64**, 1591 (2003).

[13] L. L. Kazmerski, M. S. Ayyagari, and G. A. Sanborn, J. Appl. Phys. **46**, 4865 (1975).

[14] D. C. Look and J. C. Manthuruthil, J. Phys. Chem. Solids **37**, 173 (1976).

[15] J. Kneisel, K. Siemer, I. Luck, and D. Braunig, J. Appl. Phys. **88**, 5474 (2000).

[16] A. Luque and S. Hegedus, *Handbook of Photovoltaic Science and Engineering*, Hoboken, 2003).

[17] M. Green, Prog. Photovolt.: Res. Appl. **9**, 123 (2001).

[18] C. H. Henry, J. Appl. Phys. **51**, 4494 (1980).

[19] A. D. Vos, J. Phys. D.: Appl. Phys. **13**, 839 (1980).

[20] J. T. Heath, J. D. Cohen, and W. N. Shafarman, in *Materials Research Society* (MRS, San Francisco, CA, 2003), Vol. 763, p. B9.2.1.

[21] J. D. C. J. T. Heath, and W. N. Shafarman, Journal of Applied Physics **95**, 1000 (2004).

[22] P. K. Johnson, J. T. Heath, J. D. Cohen, K. Ramanathan, and J. R. Sites, Prog. Photovolt.: Res. Appl. **13**, 579 (2005).